

PASSIVE WIRELESS SENSOR BASED ON REFLECTED ELECTRO-MATERIAL SIGNATURES

A Thesis
Presented to
The Academic Faculty

by

Azhar Hasan

In Partial Fulfillment
of the Requirements for the Degree
Doctor of Philosophy in the
School of Electrical and Computer Engineering

Georgia Institute of Technology
May 2012

PASSIVE WIRELESS SENSOR BASED ON REFLECTED ELECTRO-MATERIAL SIGNATURES

Approved by:

Professor Andrew F. Peterson, Advisor
School of Electrical and Computer
Engineering
Georgia Institute of Technology

Professor Gregory D. Durgin
School of Electrical and Computer
Engineering
Georgia Institute of Technology

Professor Emmanouil M. Tentzeris
School of Electrical and Computer
Engineering
Georgia Institute of Technology

Professor Yang Wang
School of Civil and Environmental
Engineering
Georgia Institute of Technology

Date Approved: March 26, 2012

Humbly dedicated to the heir of Hussein, the 12th Imam, Al-Mahdi.

ACKNOWLEDGEMENTS

First of all, I would like to thank ‘Allah Almighty’ for granting the opportunity and giving me the courage to reach this milestone in life. I would like to express my utmost gratitude to my parents, for their kind prayers and support. Whatever good I possess today, is their effort and hard work.

I want to extend my sincere thanks to my advisor, Dr. Andrew F. Peterson, for his unprecedented support and valuable guidance. I want to thank the members of my PhD committee, especially Dr Gregory D. Durgin, for providing worthy guidance through out the course of my PhD. I am also grateful to Dr. Paul Steffes and Danny Doung for their cooperation and help in the measurement campaign. I also want to acknowledge the moral support and friendship that I enjoyed with all the members of Propagation group especially Dr. Joshua D. Griffin, Dr Ryan Prikl, Dr Mathew Trotter, Gregory Koo, Raj Bhattacharjea, Albert Lu, Bashir Akbar, Christopher Valenta, Blake Marshall and Marcin. I want to express my gratitude to my friends, Dr Manzar Abbas, Dr Murtaza Askari, Hamza Faraz, Nasir Baqar, Faisal Siddiqui, Dr Ali Hassan, Hussain Raza and Moazzam Ali khan for their all-out support and friendship. I would also like to thank my brother, Dr Mazhar Hasan and my sisters, Urooj and Uzma for extending unmatched help through out this demanding time of my life. Thanks for believing in me.

Finally and most importantly, I am highly indebted to my wife and children, for their unconditional support, patience and tolerance of my mood swings and unusual working routines during the complete duration of this PhD. Samar, Ramsha, Fatima and Abbas, it became possible only with your affectionate help and support.

TABLE OF CONTENTS

DEDICATION	iii
ACKNOWLEDGEMENTS	iv
LIST OF TABLES	viii
LIST OF FIGURES	xi
SUMMARY	xvi
I INTRODUCTION	1
1.1 Motivation	1
1.2 The Problem and its Significance	2
1.3 Electro-Material Line	3
1.4 Reflected Electro-Material Signatures (REMS) Sensor	7
1.5 The Central Idea	7
1.6 Reconstructing the Spatially Distributed Permittivity Profile	9
1.7 Organization of the Thesis	11
II MATERIAL CHARACTERIZATION	13
2.1 Dielectric Materials at Microwave Frequencies	16
2.1.1 Dipole Polarization	16
2.1.2 Ferroelectricity	16
2.2 Techniques for Material Characterization	17
III ARTIFICIAL NEURAL NETWORKS	22
3.1 Neuron Architecture	22
3.1.1 <i>Single Neuron</i>	22
3.1.2 <i>Layer of Neurons</i>	24
3.1.3 <i>Multiple Layers of Neurons</i>	24
3.1.4 <i>Transfer Function (Activation function)</i>	26
3.2 Training Algorithms	26

3.2.1	Gradient Descent	28
3.2.2	Variable Learning Rate	28
3.2.3	Resilient Back Propagation	29
3.2.4	Conjugate Gradient Algorithms	29
3.2.5	Quasi Newton Algorithms	31
3.2.6	Levenberg Marquardt Algorithm	32
3.3	Training Data	33
IV	LOSSLESS ELECTRO-MATERIAL LINE	34
4.1	Calculating the Reflection Coefficient from a Transmission line Model	35
4.2	Training Algorithm: Comparison and Selection	37
4.3	Application of Neural Networks for Extracting Material Properties (ϵ_r)	40
4.4	Experimental Measurement and Analysis	45
4.5	Discussion	49
V	THERMO-RESPONSIVENESS AT MICROWAVE FREQUENCIES	51
5.1	Variations in ϵ_r with Temperature Changes	51
5.1.1	Preliminary Experimental Observations	51
5.2	Experimental Verification of Thermo-responsiveness of LC 5CB and Isopropyl Alcohol	54
5.2.1	Measurement Setup	56
5.2.2	Variations in ϵ'_r and $\tan \delta$ of LC 5CB with temperature . . .	57
5.2.3	Variations in ϵ'_r and $\tan \delta$ of Isopropyl Alcohol with temperature	67
5.3	Conclusion	69
VI	RECONSTRUCTING THE COMPLEX PERMITTIVITY . . .	71
6.1	Reconstructing the Complex Permittivity	71
6.2	The Monopole Antenna Model	73
6.3	Neural Network Model for Complex Permittivity	76
6.4	Measurement of Complex Permittivity using Scaled Inputs	80
6.5	Complex ϵ_r Measurements using One Neural Network	83

6.6	Discussion	84
VII DISSIPATIVE ELECTRO-MATERIAL LINE		86
7.1	Setting up the Problem	86
7.2	Variation in Γ_{in} in response to variations in ϵ_r	90
7.2.1	Case 1 : Varying ϵ'_{r2} only	90
7.2.2	Case 2 : Varying $\tan \delta_2$ only	92
7.2.3	Case 3 : Varying $\tan \delta_1, \tan \delta_2$ and $\tan \delta_3$ while $\epsilon'_{r1} = \epsilon'_{r2} = \epsilon'_{r3}$	93
7.2.4	Case 4 : Varying $\tan \delta_1, \tan \delta_2$ and $\tan \delta_3$ with $\epsilon'_{r1} \neq \epsilon'_{r2} \neq \epsilon'_{r3}$	98
7.3	Neural Networks for a Lossy Electro-material Line	99
7.3.1	Lossy electro-material line with $\epsilon'_{r1} = \epsilon'_{r2} = \epsilon'_{r3}$	103
7.3.2	Lossy electro-material line with $\epsilon'_{r1} \neq \epsilon'_{r2} \neq \epsilon'_{r3}$	106
7.4	Reconstructing spatially distributed ϵ'_r and $\tan \delta$	109
7.4.1	Reconstructing $\tan \delta$	110
7.4.2	Reconstructing ϵ'_r	115
7.4.3	Reconstructing complex $\epsilon_r = \epsilon'_r(1 - j \tan \delta)$	124
7.5	Discussion	124
VIII CONCLUSION AND FUTURE WORK		126
APPENDIX A — A COMPARISON BETWEEN NEURAL NETWORKS & MULTIPLE LINEAR REGRESSION ALGORITHMS FOR REMS		131
REFERENCES		137
VITA		143

LIST OF TABLES

1	Dimensions of cascaded microstrip transmission lines	35
2	Results for back-solving ϵ'_{r2} using a neural network with Levinberg Marquardt backpropagation algorithm.	42
3	Comparison of actual values of $\epsilon_{r1,2,3}$ vs neural network output	43
4	Dimensions of microstrip transmission lines in experimental setup. . .	45
5	Comparison of actual values of $\epsilon_{r1,2,3}$ with the neural network results obtained with 1 layer of 20 neurons and trained on data having different levels of white noise, over the frequency range from 1-5 GHz.	48
6	The actual values of $\epsilon_{r1,2,3}$ compared to the values estimated using neural networks for the frequency range 1-2.5 GHz.	48
7	The actual values of complex permittivity ($\epsilon_r = \epsilon'_r - j\epsilon''_r$) compared to the neural network output	78
8	The actual values of complex permittivity ($\epsilon_r = \epsilon'_r - j\epsilon''_r$) compared to the two sets of estimated values and the respective percent error over the frequency range 2.5-5GHz	81
9	The actual values of complex permittivity ($\epsilon_r = \epsilon'_r - j\epsilon''_r$) compared to the two sets of estimated values and the respective percent error over the frequency range 3.5-5GHz	82
10	The actual values of complex permittivity ($\epsilon_r = \epsilon'_r - j\epsilon''_r$) compared to the two sets of estimated values and the respective percent error over the frequency range 4-5GHz	83
11	The actual values of complex permittivity ($\epsilon_r = \epsilon'_r - j\epsilon''_r$) compared to the two sets of estimated values using 1 neural network, and the respective percent error over the frequency range 4-5GHz	84
12	Dimensions of the microstrip transmission lines used for lossy electro-material line	104
13	Results for estimating $\tan \delta_{1,2,3}$ using neural networks with 20 neurons in the hidden layer for a lossy electro-material line with $\epsilon'_{r1,2,3} = 2.4$. .	105
14	Results for estimating $\tan \delta_{1,2,3}$ using neural networks with 35 neurons in the hidden layer for a lossy electro-material line with $\epsilon'_{r1,2,3} = 2.4$. .	105
15	Results for estimating $\tan \delta_{1,2,3}$ using neural networks with 20 neurons in hidden layer for a lossy electro-material line with $\epsilon'_{r1} = 2.4$, $\epsilon'_{r2} = 4.4$, and $\epsilon'_{r3} = 6.6$	107

16	Results for estimating $\tan \delta_{1,2,3}$ using neural networks with 30 neurons in hidden layer for a lossy electro-material line with $\epsilon'_{r1} = 2.4$, $\epsilon'_{r2} = 4.4$, and $\epsilon'_{r3} = 6.6$	107
17	Results for estimating $\tan \delta_{1,2,3}$ using neural networks with 20 neurons in hidden layer for a lossy electro-material line with $\epsilon'_{r1} = 2.4$, $\epsilon'_{r2} = 4.4$, and $\epsilon'_{r3} = 6.6$, in presence of white Gaussian noise with 10 dB SNR. .	108
18	Results for estimating $\tan \delta_{1,2,3}$ using neural networks with 20 neurons in hidden layer for a lossy electro-material line with $3.5 \leq \epsilon'_{r1} \leq 4.0$, $2.5 \leq \epsilon'_{r2} \leq 3.0$, and $4.5 \leq \epsilon'_{r3} \leq 5.0$, for the frequency range of 4.0 - 5.5 GHz with $\Delta f = 75MHz$	111
19	Results for estimating $\tan \delta_{1,2,3}$ using neural networks with 20 neurons in hidden layer for three different lossy electro-material lines with $3.5 \leq \epsilon'_{r1} \leq 4.0$, $2.5 \leq \epsilon'_{r2} \leq 3.0$, and $4.5 \leq \epsilon'_{r3} \leq 5.0$. The results are presented for the frequency range of 4.0 - 5.5 GHz with $\Delta f = 75MHz$, in presence of white Gaussian noise with 10dB, 15dB, 20dB, 25dB and 30dB SNR. (Est. denotes estimated)	113
20	Results for estimating $\tan \delta_{1,2,3}$ using neural networks with 25 neurons in hidden layer for a lossy electro-material line with $3.5 \leq \epsilon'_{r1} \leq 4.0$, $2.5 \leq \epsilon'_{r2} \leq 3.0$, and $4.5 \leq \epsilon'_{r3} \leq 5.0$, for the frequency range of 4.0 - 5.5 GHz with $\Delta f = 75MHz$	115
21	Results for estimating $\tan \delta_{1,2,3}$ using neural networks with 25 neurons in hidden layer for three different lossy electro-material lines with $3.5 \leq \epsilon'_{r1} \leq 4.0$, $2.5 \leq \epsilon'_{r2} \leq 3.0$, and $4.5 \leq \epsilon'_{r3} \leq 5.0$. The results are presented for the frequency range of 4.0 - 5.5 GHz with $\Delta f = 75MHz$, in presence of white Gaussian noise with 10dB, 15dB, 20dB, 25dB and 30dB SNR. (Est. denotes estimated)	116
22	Results for estimating $\tan \delta_{1,2,3}$ using neural networks with 30 neurons in hidden layer for three different lossy electro-material lines with $3.5 \leq \epsilon'_{r1} \leq 4.0$, $2.5 \leq \epsilon'_{r2} \leq 3.0$, and $4.5 \leq \epsilon'_{r3} \leq 5.0$. The results are presented for the frequency range of 4.0 - 5.5 GHz with $\Delta f = 75MHz$, in presence of white Gaussian noise with 10dB, 15dB, 20dB, 25dB and 30dB SNR. (Est. denotes estimated)	117
23	Results for estimating $\tan \delta_{1,2,3}$ using neural networks with 35 neurons in hidden layer for three different lossy electro-material lines with $3.5 \leq \epsilon'_{r1} \leq 4.0$, $2.5 \leq \epsilon'_{r2} \leq 3.0$, and $4.5 \leq \epsilon'_{r3} \leq 5.0$. The results are presented for the frequency range of 4.0 - 5.5 GHz with $\Delta f = 75MHz$, in presence of white Gaussian noise with 15dB, 20dB, 25dB and 30dB SNR. (Est. denotes estimated)	118

24	Results for estimating $\tan \delta_{1,2,3}$ using neural networks with 40 neurons in hidden layer for three different lossy electro-material lines with $3.5 \leq \epsilon'_{r1} \leq 4.0$, $2.5 \leq \epsilon'_{r2} \leq 3.0$, and $4.5 \leq \epsilon'_{r3} \leq 5.0$. The results are presented for the frequency range of 4.0 - 5.5 GHz with $\Delta f = 75MHz$, in presence of white Gaussian noise with 15dB, 20dB, 25dB and 30dB SNR. (Est. denotes estimated)	119
25	Results for estimating $\epsilon'_{r1,2,3}$ using neural networks with 20 neurons in hidden layer for three different lossy electro-material lines with $0.01 \leq \tan \delta_{1,2,3} \leq 0.10$. The results are presented for the frequency range of 4.0 - 5.5 GHz with $\Delta f = 75MHz$. (Est. denotes estimated)	120
26	Results for estimating $\epsilon'_{r1,2,3}$ using neural networks with 20 neurons in hidden layer for three different lossy electro-material lines with $0.01 \leq \tan \delta_{1,2,3} \leq 0.10$. The results are presented for the frequency range of 4.0 - 5.5 GHz with $\Delta f = 75MHz$, in presence of white Gaussian noise with 10dB, 15dB, and 20dB SNR. (Est. denotes estimated)	121
27	Results for estimating $\epsilon'_{r1,2,3}$ using neural networks with 25 neurons in hidden layer for three different lossy electro-material lines with $0.01 \leq \tan \delta_{1,2,3} \leq 0.10$. The results are presented for the frequency range of 4.0 - 5.5 GHz with $\Delta f = 75MHz$, in presence of white Gaussian noise with 10dB, 15dB, and 20dB SNR. (Est. denotes estimated)	122
28	Results for estimating $\epsilon'_{r1,2,3}$ using neural networks with 30 neurons in hidden layer for three different lossy electro-material lines with $0.01 \leq \tan \delta_{1,2,3} \leq 0.10$. The results are presented for the frequency range of 4.0 - 5.5 GHz with $\Delta f = 75MHz$, in presence of white Gaussian noise with 10 dB, 15 dB, and 20 dB SNR. (Est. denotes estimated)	123
29	Results for estimating $\tan \delta_{1,2,3}$ using multiple linear regression for three different lossy electro-material lines with $3.5 \leq \epsilon'_{r1} \leq 4.0$, $2.5 \leq \epsilon'_{r2} \leq 3.0$, and $4.5 \leq \epsilon'_{r3} \leq 5.0$. The results are presented for the frequency range of 4.0 - 5.5 GHz with $\Delta f = 75MHz$, in presence of white Gaussian noise with 15dB, 20dB, 25dB and 30dB SNR. (Est. denotes estimated)	134
30	Results for estimating $\epsilon'_{r1,2,3}$ using multiple linear regression for three different lossy electro-material lines with $0.01 \leq \tan \delta_{1,2,3} \leq 0.10$. The results are presented for the frequency range of 4.0 - 5.5 GHz with $\Delta f = 75MHz$, in presence of white Gaussian noise with 10dB, 15dB, and 20dB SNR. (Est. denotes estimated)	135

LIST OF FIGURES

1	The polymerization process records the historical temperature profile in the spatial distribution of electrical properties of the material line.	4
2	The polymerization process developing a spatially distributed permittivity profile in the electro-material line. The permittivity depends upon the temperature it experienced at the time when liquid crystals were frozen into the cell area being polymerized.	6
3	Components of a REMS Sensor.	8
4	Block Diagram of a REMS sensor. Spatially distributed permittivity profile of the electro-material line is depicted by 8 different bins with arbitrary values of ϵ_r	9
5	Small reflections model in comparison with the electro-material line .	10
6	Impedance matching with multi-section and continuous impedance tapers	10
7	Single input neuron with weight, bias and activation function	23
8	Single neuron with multiple inputs and one output and one activation function	23
9	One layer of multiple neurons	25
10	Three layers of multiple neurons	25
11	Hard Limit Transfer Function	26
12	Linear Transfer Function	27
13	Log Sigmoidal Transfer Function	27
14	The microstrip line model with three discrete segments having different permittivity profiles, terminated in a load to emulate a REMS sensor with three wells of sensor material.	35
15	Three transmission lines cascaded together and terminated in a load.	36
16	Signal Flow Graph for calculating Γ	36
17	The transmission line model of the RF tag, illustrating four changing permittivity profiles of the center well of the REMS sensor.	37
18	Magnitude of Γ_{IN} for $\epsilon_{r2} = 2, 3, 4$ and 5 calculated from the signal flow graph.	38
19	Phase of Γ_{IN} for $\epsilon_{r2} = 2, 3, 4$ and 5 calculated from the signal flow graph.	39

20	Overhead view on a PCB of a simple model of an electro-material line with $\epsilon_{r1} = 3$, $\epsilon_{r3} = 3.8$, and $2 \leq \epsilon_{r2} \leq 8$	40
21	The neural network architecture with 10 neurons in the hidden layer, and one neuron in the output layer.	42
22	ANN architecture for backsolving permittivity profile of a microstrip line structure emulating a 3-bin electro-material line	43
23	Correlation coefficient (R) of regression analysis plotted against the number of neurons for a network trained with data having white Gaussian noise. Number ‘30’ on the X-axis represents two hidden layers of 10 neurons each	44
24	Snapshot of microstrip transmission line setup for experimental measurements.	45
25	Comparison between magnitude of measured and calculated reflection coefficient ($ \Gamma_{in} $).	46
26	Comparison between measured and calculated phase of reflection coefficient ($\angle\Gamma_{in}$).	47
27	Measurement setup to measure S11 at different temperatures for a 10mm monopole probe immersed in Liquid Crystal 5CB	52
28	Measured S11(complex-valued quantity displayed as a polar plot) for a 10mm monopole probe immersed in the liquid crystal 5CB	53
29	Measurement setup to measure S11 at different temperatures for a 10mm monopole probe immersed in isopropyl Alcohol	53
30	Measured S11(complex-valued quantity displayed as a polar plot) for a 10mm monopole probe immersed in isopropyl Alcohol	54
31	High-temperature dielectric probe of the Agilent 85070D Dielectric Probe Kit (From product overview).	55
32	Dielectric probe kit accuracy vs frequency for $\epsilon'_r = 2, 5, 20, 50$ and 80. (From product overview).	55
33	Measurement setup to measure S11 at different temperatures using the Agilent dielectric probe immersed in isopropyl alcohol	56
34	Measurement setup to measure S11 at different temperatures using the Agilent dielectric probe immersed in isopropyl alcohol	58
35	Variations in ϵ'_r of LC 5CB as the temperature is varied from $5^\circ C$ to $9^\circ C$ over the frequency range from 3.5 GHz to 6 GHz.	59

36	Variations in $\tan \delta$ of LC 5CB as the temperature is varied from $5^{\circ}C$ to $9^{\circ}C$ over the frequency range from 3.5 GHz to 6 GHz.	59
37	Variations in ϵ'_r of LC 5CB as the temperature is increased from $22^{\circ}C$ to $23^{\circ}C$ over the frequency range from 3.5 GHz to 6 GHz.	60
38	Variations in $\tan \delta$ of LC 5CB as the temperature is increased from $22^{\circ}C$ to $23^{\circ}C$ over the frequency range from 3.5 GHz to 6 GHz. . . .	60
39	Variations in ϵ'_r of LC 5CB as the temperature is increased from $23^{\circ}C$ to $26^{\circ}C$ over the frequency range from 3.5 GHz to 6 GHz.	61
40	Variations in $\tan \delta$ of LC 5CB as the temperature is increased from $23^{\circ}C$ to $26^{\circ}C$ over the frequency range from 3.5 GHz to 6 GHz. . . .	61
41	Variations in ϵ'_r of LC 5CB as the temperature is increased from $27^{\circ}C$ to $40^{\circ}C$ over the frequency range from 3.5 GHz to 6 GHz.	62
42	Variations in $\tan \delta$ of LC 5CB as the temperature is increased from $27^{\circ}C$ to $40^{\circ}C$ over the frequency range from 3.5 GHz to 6 GHz. . . .	62
43	ϵ'_r for water computed using Miessner and Wentz model for the frequency range from 3-6 GHz	64
44	$\tan \delta$ for water computed using Miessner and Wentz model for the frequency range from 3-6 GHz	65
45	ϵ'_r of LC 5CB for different temperatures over the frequency range from 3.5 GHz to 6 GHz, after using the Meissner & Wentz model correction.	66
46	$\tan \delta$ of LC 5CB for different temperatures over the frequency range from 3.5 GHz to 6 GHz, after using the Meissner & Wentz model correction.	66
47	Variations in ϵ'_r of Isopropyl alcohol as the temperature is varied from $9^{\circ}C$ to $40^{\circ}C$ over the frequency range from 3 - 6 GHz.	67
48	Variations in $\tan \delta$ of Isopropyl alcohol as the temperature is varied from $9^{\circ}C$ to $40^{\circ}C$ over the frequency range from 3 - 6 GHz.	68
49	ϵ'_r of Isopropyl alcohol for different temperatures over the frequency range from 3 - 6 GHz, after using the Meissner & Wentz model correction.	68
50	$\tan \delta$ of Isopropyl alcohol for different temperatures over the frequency range from 3.5 GHz to 6 GHz, after using the Meissner & Wentz model correction.	69
51	A monopole probe of height h , radius a , and connected to ground plane with diameter d , immersed in a dissipative dielectric medium with permittivity $\epsilon_r = \epsilon'_r - j\epsilon''_r$	72

52	A monopole probe of height h and radius a , immersed in a dissipative dielectric medium with permittivity $\epsilon_r = \epsilon'_r - j\epsilon''_r$, and connected to a VNA	75
53	A two layer multiple neuron neural network	76
54	The neural network model comprising two networks, #1 solving for ϵ'_r and #2 reconstructing ϵ''_r , using the Levenberg Marquardt back-propagation algorithm	78
55	The input vectors corresponding to different values of the complex permittivity $\epsilon_r = \epsilon'_r - j\epsilon''_r$	79
56	Scaled input vectors corresponding to different values of the complex permittivity $\epsilon_r = \epsilon'_r - j\epsilon''_r$	80
57	The neural network model comprising two networks with scaled inputs, #1 solving for ϵ'_r , and #2 reconstructing ϵ''_r , using the Levenberg Marquardt back-propagation algorithm	81
58	Scaled input vectors corresponding to the different values of complex permittivity $\epsilon_r = \epsilon'_r - j\epsilon''_r$	82
59	The neural network model having only one network with scaled inputs, #1 solving for ϵ'_r , and #2 reconstructing ϵ''_r , using the Levenberg Marquardt back-propagation algorithm	84
60	Input training vectors for 17 different sets of $\epsilon_{r1,2,3}$. The change in magnitude of Γ_{in} is much more pronounced as compared to the change in phase across the range complex permittivity values of interest. . .	88
61	Input training vectors for 17 different sets of $\epsilon_{r1,2,3}$. Phase is scaled by the 5 to evenly distribute the information across all elements of input vector. The scaling factor is determined through linear scaling. . . .	89
62	$ \Gamma_{in} $ for three section lossy electro-material line with $\epsilon'_{r1} = 3.5$, $\epsilon'_{r3} = 5.5$, $\tan \delta_1 = \tan \delta_2 = \tan \delta_3 = 0.01$. Four different values of ϵ'_{r2} are used, $\epsilon'_{r2} = 2.0, 2.9, 3.8, 5.0$, to demonstrate the effect of varying ϵ'_r while keeping $\tan \delta$ fixed.	91
63	Phase of Γ_{in} for three section lossy electro-material line with $\epsilon'_{r1} = 3.5$, $\epsilon'_{r3} = 5.5$, $\tan \delta_1 = \tan \delta_2 = \tan \delta_3 = 0.01$. Four different values of ϵ'_{r2} are used, $\epsilon'_{r2} = 2.0, 2.9, 3.8, 5.0$, to demonstrate the effect of varying ϵ'_r while keeping $\tan \delta$ fixed.	92
64	$ \Gamma_{in} $ for three section lossy electro-material line with $\epsilon'_{r1} = 3.5$, $\epsilon'_{r2} = 2$, $\epsilon'_{r3} = 5.5$, $\tan \delta_1 = \tan \delta_3 = 0.01$. To demonstrate the effect of varying $\tan \delta$ while keeping ϵ'_r fixed, four different values of $\tan \delta_2$ are used, $\tan \delta_2 = 2.0, 2.9, 3.8, 5.0$	94

65	Phase of Γ_{in} for three section lossy electro-material line with $\epsilon'_{r1} = 3.5$, $\epsilon'_{r2} = 2$, $\epsilon'_{r3} = 5.5$, $\tan \delta_1 = \tan \delta_3 = 0.01$. To demonstrate the effect of varying $\tan \delta$ while keeping ϵ'_r fixed, four different values of $\tan \delta_2$ are used, $\tan \delta_2 = 2.0, 2.9, 3.8, 5.0$	95
66	$ \Gamma_{in} $ for three section lossy electro-material line with $\epsilon'_{r1} = \epsilon'_{r2} = \epsilon'_{r3}$, while varying $\tan \delta_{1,2,3}$. To demonstrate the effect of varying $\tan \delta$ while keeping ϵ'_r fixed, three different combinations of $\tan \delta_{1,2,3}$ are used satisfying the equality described in Eq. 75.	96
67	Phase of Γ_{in} for three section lossy electro-material line with $\epsilon'_{r1} = \epsilon'_{r2} = \epsilon'_{r3}$, while varying $\tan \delta_{1,2,3}$. To demonstrate the effect of varying $\tan \delta$ while keeping ϵ'_r fixed, three different combinations of $\tan \delta_{1,2,3}$ are used satisfying the equality described in Eq. 75.	97
68	$ \Gamma_{in} $ for three section lossy electro-material line with $\epsilon'_{r1} \neq \epsilon'_{r2} \neq \epsilon'_{r3}$, while varying $\tan \delta_{1,2,3}$. To demonstrate the effect of varying $\tan \delta$, three different combinations of $\tan \delta_{1,2,3}$ are used as highlighted in Eq. 84 - Eq. 76.	100
69	Phase of Γ_{in} for three section lossy electro-material line with $\epsilon'_{r1} \neq \epsilon'_{r2} \neq \epsilon'_{r3}$, while varying $\tan \delta_{1,2,3}$. To demonstrate the effect of varying $\tan \delta$, three different combinations of $\tan \delta_{1,2,3}$ are used as highlighted in Eq. 84 - Eq. 76.	101
70	A neural network with one hidden layer and three output neurons.	104
71	Two neural networks integrated together to backsolve ϵ_r of lossy electro-material line. Network 1 solves for ϵ'_r and network 2 reconstructs the $\tan \delta$	110
72	Coefficient of correlation, R , computed for different values of SNR in white Gaussian noise for a neural network with 20 neurons in the hidden layer.	114

SUMMARY

The objective of the proposed research is to devise a methodology for sensing and tracking environmental variables using a passive wireless sensor based on reflected electro-material signatures. Viability of item level tracking demands the sensor to be extraordinary low cost, thus eliminating the use of any active sensor or memory circuitry. Recent developments of materials whose electrical properties can change significantly with the environmental conditions suggest the possibility of developing a passive sensor that can be interrogated remotely to extract data about the time tracked environmental changes at the sensor. A simple passive sensor, based on the concept of reflected electro-material signatures (REMS), consists of an antenna attached to a microstrip transmission line, which in turn is routed over one or more sections of variable permittivity material before being terminated in a load. The basic idea revolves around sensing the electrical properties of thermotropic liquid crystal (LCs) trapped in a polymer substrate to record the temperature data. As the temperature changes with time, the polymerization process through the material line records the historical temperature profile in the spatial distribution of the electrical properties, thus enabling the system to extract the historical profile of temperature without using any active memory circuitry. This concept can possibly be used to track a variety of variables of interest; however, the proposed research is focused on sensing and extracting the time profile of temperature. The problem of identifying medium properties from waves reflected from a device of this type is a form of the classical one dimensional inverse scattering problem. For profile inversion in a lossy inhomogeneous media, analytical techniques are difficult to implement in most practical situations. In the proposed research, neural networks with a back-propagation algorithm are

used to reconstruct the historical temperature profile of the material by extracting the spatially distributed material properties of the electro-material line. After the initial proof of concept for a lossless medium, the methodology is extended to extract spatially distributed properties for a dissipative medium. Finally, for the implementation of REMS sensor concept, a neural network based methodology is developed to reconstruct the spatially distributed permittivity profile of a lossy electro-material line.

Azhar Hasan

CHAPTER I

INTRODUCTION

1.1 Motivation

Wireless sensing is gaining interest from a wide variety of disciplines. Passive sensors, that reduce cost and eliminate batteries, have attracted great attention of researchers. In the recent past there is an increased interest in developing sensors with capabilities much more than merely sensing a parameter. For example, when perishable goods are transported through cold supply chains and are exposed to temperature fluctuations, it results in reduced shelf life or renders them unusable. Item level tracking and monitoring is an effective way of verifying that refrigerated food has been maintained at an appropriate temperature during storage and shipping. The viability of item-level tracking demands that the sensor be extraordinary low-cost, thus eliminating the use of any active sensor or memory circuitry. Recent developments of materials whose electrical properties can change significantly with the environmental conditions suggest the possibility of developing a passive sensor that can be interrogated remotely to extract data about the time-tracked environmental changes at the sensor [1].

A simple passive sensor, based on the concept of *reflected electro-material signatures* (REMS), consists of an antenna attached to a microstrip transmission line, which in turn is routed over one or more sections of variable permittivity material before being terminated in a load. The material properties of the transmission line will change in response to the change in the environmental conditions, and would be sensed using the REMS based sensor. This concept can possibly be used to track a variety of variables of interest; however, this research is focused on developing a methodology for sensing and extracting the time profile of temperature.

1.2 The Problem and its Significance

Advances in passive RFID sensors and recent developments in materials allow a number of tracking and sensing applications. A variety of sensors, sensing strain, displacement, acceleration, deformation and other damage indices, employing smart materials and/or smart structures have been proposed for structural health monitoring (SHM). Correlating the change in the electric resistance and peak/residual strain for Carbon Fiber Glass Fiber Reinforced Plastic(CFGFRP), a peak strain sensor was proposed by Muto et.al. [2]. As the electric resistance of CFGFRP changes with strain, the material itself could function as a sensor. In an effort for developing mechanical memory, Westermo and Thompson used Transformation Induced Plasticity (TRIP) steel for memorizing the peak strain, as it gets magnetized when large strain is applied [3]. As another example, capacitive peak strain sensors, using two concentric conducting pipes with dielectric in between, have been developed to monitor the structural health of materials [4]. The relative displacement of the pipes can be gauged through the change in capacitance, which causes a resonant frequency shift detectable by the sensor. Simonen et.al. proposed a corrosion sensor to sense the corrosion thresholds which exploits the shift in resonant frequency as the length of the sensor wire changes with corrosion [5]. Corrosion breaks the wire, thus acting as a switch to open the LC circuit and thus causing a noticeable shift in the resonant frequency. In the recent past researchers have also proposed single walled nanotube-based inductively coupled passive wireless sensors for structural monitoring [6].

In the UHF band, the change in the tagged body's feature can be detected without using any specific sensor. The input impedance of an RF tag is dependent on the physical/material properties of the tag, and this can be exploited to estimate the tag's permittivity using the multiport tag concept [7, 8]. With the reader-tag distance known, the change in the target permittivity is detected by monitoring the power backscattered by the transponder, however, it requires prior calibration for using the

ratio of backscattered power to estimate the change in permittivity correctly.

Based on the fact that the RFID tag performance deteriorates in close vicinity of metals, Bhattacharyya et.al. proposed a RFID-tag-antenna-based sensor for temperature thresholds and displacement sensing [9]. They have also highlighted the concept of non-electronic memory in terms of recording the occurrence of an event in past: the event has occurred or not.

Despite increased interest in the passive sensor with the capabilities to sense and track a parameter, the problem still remains unsolved. The most challenging part of this problems comes from the need of a memory, without any active circuitry. This leads to the various options of non-electronic memory, like mechanical or chemical memory. Using a passive tag, to the best of our knowledge, researchers have been able to register only a peak value [4, 5], or a change/threshold crossing [7–9]. Developing a time profile still remains unaddressed with a passive tag. In this research, a new method is presented to sense and record time profile of parameters like temperature. The proposed methodology is based on the concept of using an *electro-material line* with a *Reflected Electro-material Signatures(REMS) Sensor*.

1.3 *Electro-Material Line*

The electro-material line is a chemical strip sandwiched between the ground plane and top trace of an RF tag’s microstrip transmission line. Any material that has environmental sensitivity to permeability, permittivity, or conductivity may be a candidate for the electro-material line in the REMS sensor. For example, a simple instantaneous temperature sensor could incorporate thermotropic liquid crystals. These types of liquid crystals experience state disordering upon heating, leading to a change in their electrical (and optical) properties [10, 11]. Another candidate material may be a line substrate doped with ferroelectric or super-paramagnetic particles [12]. Such a device could use the nonlinear relationship between field and flux density components

to sense external field strengths. The basic idea of *reflected electro-material signatures* (REMS) revolves around sensing the electrical properties of thermotropic liquid crystals (LCs) trapped in a polymer substrate to record the temperature data. As the temperature changes with time, the polymerization process through the material line records the historical temperature profile in the spatial distribution of the electrical properties. One such material line is shown in Fig. 1.

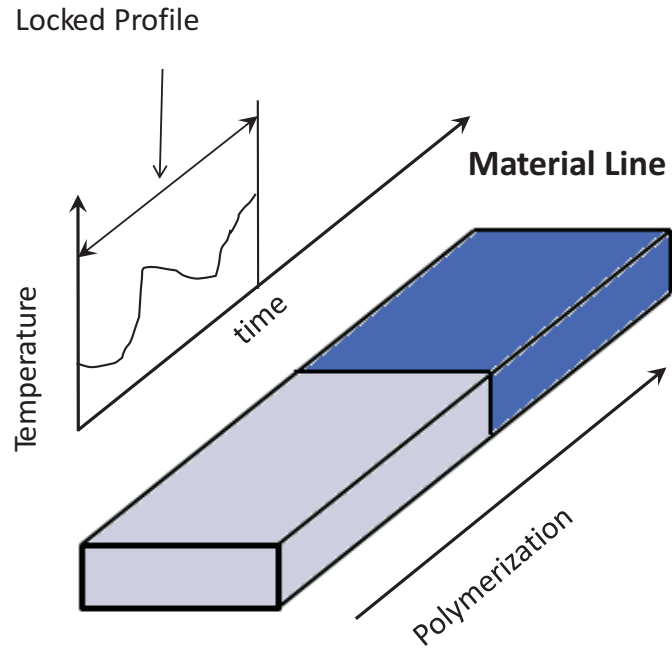


Figure 1: The polymerization process records the historical temperature profile in the spatial distribution of electrical properties of the material line.

Electrical properties of a thermo-tropic liquid crystal trapped in a polymer substrate to record the temperature data depend on the degree of ordering of the LC in the substrate. Therefore the electrical properties of the electro-material line depend upon the temperature experienced at the time the compounds were locked into position when their cell area polymerized. Properties of these frozen LCs are linked to the local capacitance and conductivity.

For time history, slow-polymerizing monomers can be mixed with the thermotropic liquid crystals. An auto-oxidizing reaction mixture begins polymerization at one end of the electro-material line. The monomers slowly knit together as polymerization proceeds. LCs along the line are effectively frozen in their mechanically disordered state, thereby trapping a record of temperature induced effects that can be electrically interrogated. This concept is explained in a simplified way in Fig. 2. The electro-material line is shown with the polymerization process. The polymerization process starts at time t_0 . The electro-material line is exposed to temperature T_1 for time Δt ($t_0 \rightarrow t_1$). Due to thermo-responsive nature of the electro-material line, its permittivity changes to ϵ_{r1} corresponding to temperature T_1 . As the polymerization process continues for time Δt , the first bin of electro-material line of length Δl is locked to permittivity ϵ_{r1} . As the polymerization process continues from time t_1 to t_2 , the temperature changes to T_2 and correspondingly liquid crystals in the next bin of length Δl are frozen to permittivity ϵ_{r2} . This process continues for the complete length l of the electro-material line resulting in a number of bins, each with a different permittivity depending upon the temperature it experienced at the time when the liquid crystals were frozen in the spatial location by polymerization.

The following assumptions are made to simplify the process for the basic proof of concept:

- The polymerization process is irreversible.
- Polymerization speed is not a function of temperature. The polymerization process will progress with uniform speed irrespective of temperature fluctuations.
- The total length of line l covers the total time period of interest.
- Polymerization is in one dimension only (along the length), and starts at one end with controlled exposure preventing the other end or portions to be frozen first.

- The electro-material line polymerization is discretized such that:
 - $\Delta t \Rightarrow \Delta l$ (each time segment corresponds to equal length segments on electro-material line)
 - The electro-material line is homogeneous within each bin of length Δl .
- ϵ_r is independent of frequency for the frequency range of our interest.

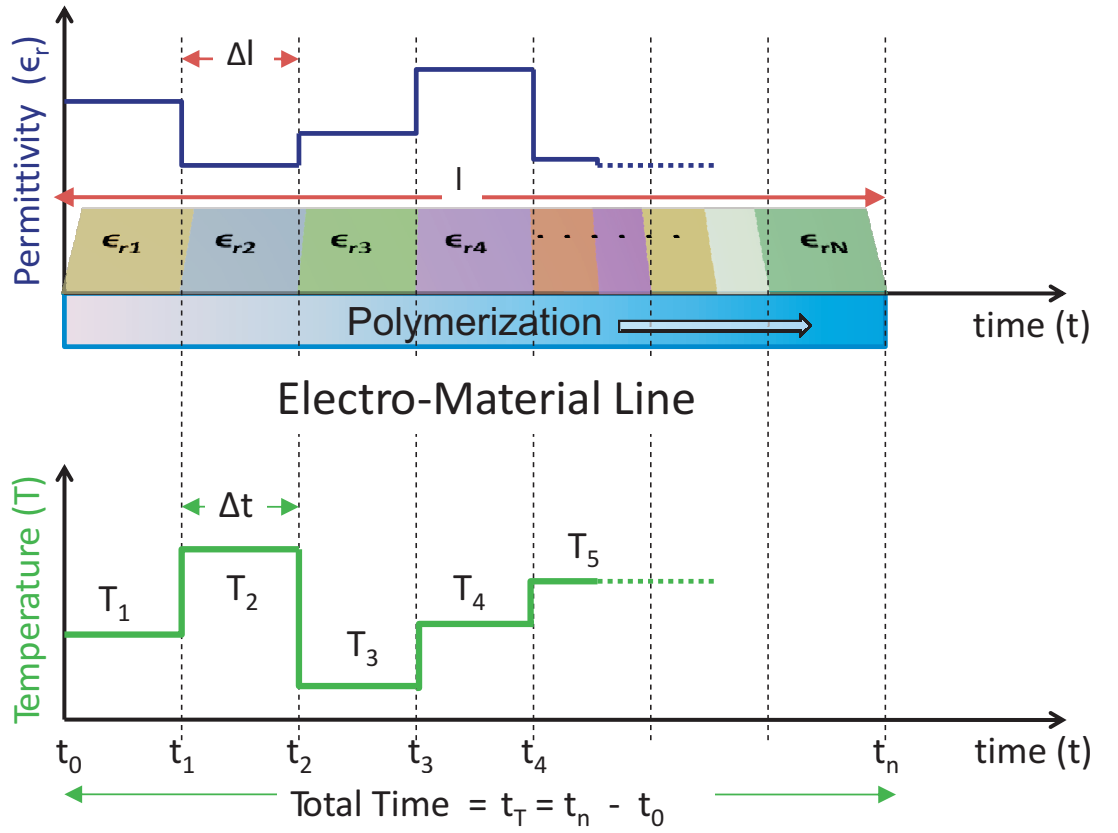


Figure 2: The polymerization process developing a spatially distributed permittivity profile in the electro-material line. The permittivity depends upon the temperature it experienced at the time when liquid crystals were frozen into the cell area being polymerized.

1.4 Reflected Electro-Material Signatures (REMS) Sensor

A sensor concept based on reflected electro-material signatures (REMS) consists of three distinct components working together to provide passive sensing capability of environment information. The first component is the electro-material line, a chemical strip sandwiched between the ground plane and top trace of an RF tag's microstrip transmission line. The second component, the reflector circuitry, consists of the transmission line itself, the radio-frequency integrated circuit (RFIC) that perform backscatter and identification functions, and any RF tag antennas. Finally, an RF reader must be used to interrogate the REMS sensor as well as perform the signal-processing for data extraction. These components are illustrated in Fig. 3.

Conceivably, the REMS concept could be implemented with existing UHF or microwave passive RFID integrated circuits, greatly lowering the cost and allowing passive interrogation of the sensor. In a conventional backscatter RFID system, the signal is reflected from a binary-switched load, providing two potential frequency-dependent measurements for extracting material line parameters [13]. Since an RFID reader filters out un-modulated scatter components, an RFID-based REMS sensor would allow a much more precise measurement compared to other forms of remote sensing.

The REMS sensor concept may also allow for materials that time-record other environmental attributes, thus providing a form of chemical memory rather than electrical memory that would achieve a completely passive sensor. This type of sensor functionality cannot be achieved under today's 'system on a chip' paradigm, which still requires external power supplies for electronic memory recording functions.

1.5 The Central Idea

In a typical RFID system, the antenna is connected to a matched load or an electrical short by a transmission line. When the matched load is connected all the

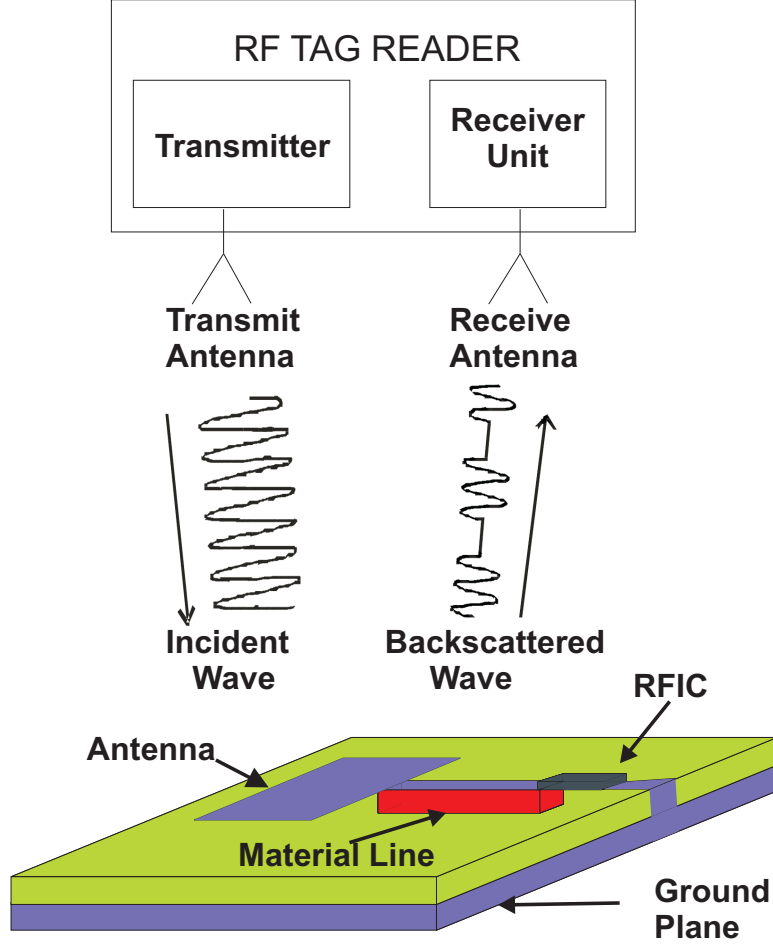


Figure 3: Components of a REMS Sensor.

power is absorbed and nothing is reflected back. When the short is connected, the transmission line experiences perfect reflection and received power is completely reflected. In REMS sensor, in place of a homogeneous dielectric transmission line, an electro-material line is used. By switching between different loads, it is possible to modulate data onto the backscattered radio wave. The electrical properties of the electro-material line and therefore its impedance varies with the environmental temperature. Thus for a REMS sensor, all the information is embedded in the spatially distributed permittivity profile of the electro-material line as shown in Fig. 4.

The central idea of this research is to reconstruct the historical temperature profile of the material by extracting the spatially distributed electrical properties of the

electro-material line.

1.6 Reconstructing the Spatially Distributed Permittivity Profile

The “theory of small reflections” is employed in various models, such as multisection, binomial, Chebyshev and tapered lines, to determine Z_n for a desired Γ and a given bandwidth [14, 15]. The small reflections model in comparison with the electro-material line is shown in Fig. 5. To highlight the difference, the impedance matching profile using continuous and multi-section tapers is shown in Fig. 6. Any desired reflection coefficient response can be synthesized by properly choosing Γ_n with a sufficient number of sections. The tapered line impedance matching transformers can not be used to back-solve the permittivity profile of the electro-material line for the following two reasons:

- In the tapered line impedance matching transformers, Z_n should be monotonically increasing or decreasing [15], while in REMS, Z_n depends on the permittivity profile of the electro-material line and varies with the temperature

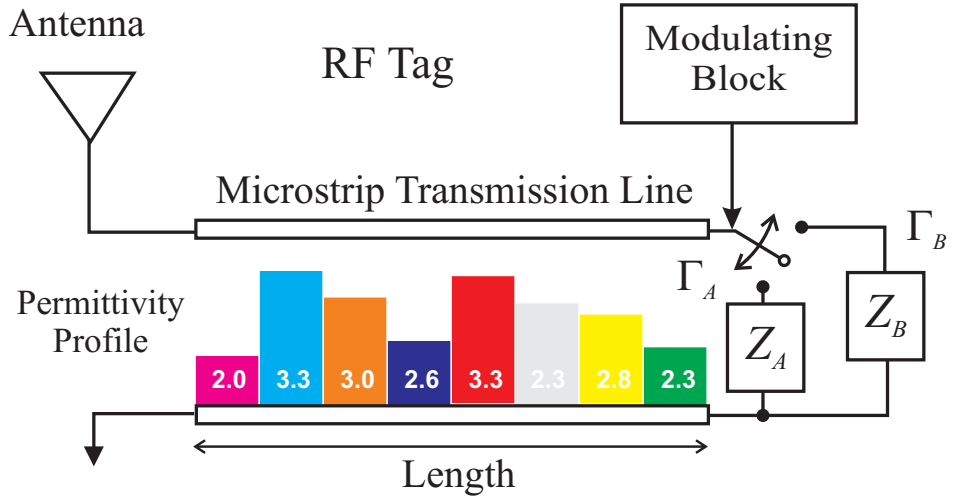
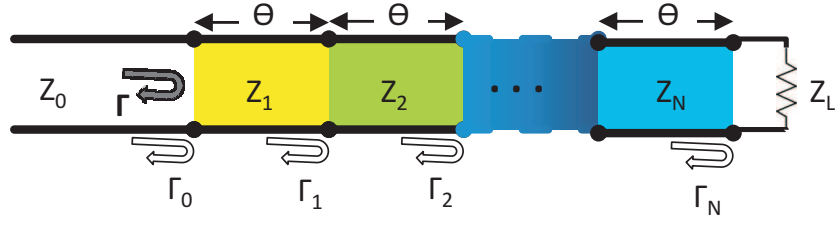


Figure 4: Block Diagram of a REMS sensor. Spatially distributed permittivity profile of the electro-material line is depicted by 8 different bins with arbitrary values of ϵ_r .

Small Reflections Model



Electro-material Line

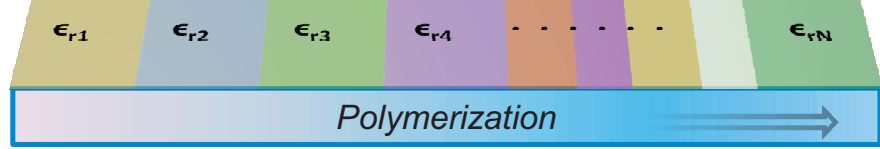


Figure 5: Small reflections model in comparison with the electro-material line

record.

- In the tapered line models, all Γ_n have the same sign and are real. However, for the REMS sensor, the electro-material line can be lossy which requires a methodology capable of handling complex reflection coefficients with possibly varying signs.

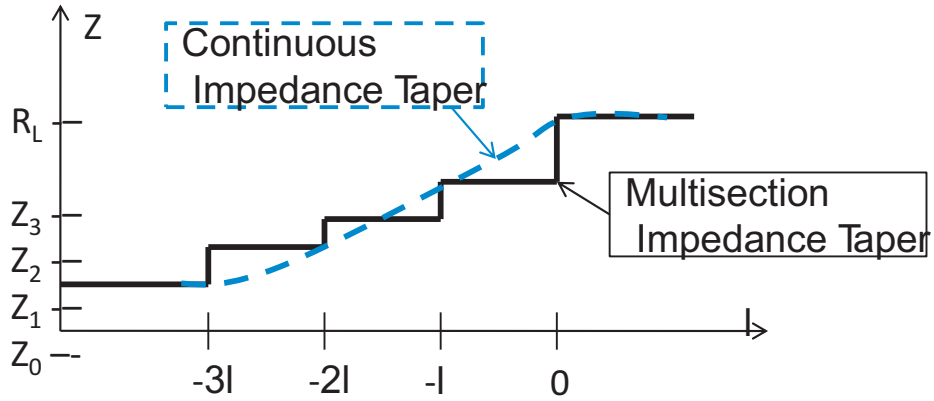


Figure 6: Impedance matching with multi-section and continuous impedance tapers

The problem of identifying medium properties from waves reflected from a device of this type is a form of the classical one-dimensional inverse scattering problem. For

profile inversion in a lossy inhomogeneous medium, analytical techniques are difficult to implement in most practical situations, and thus various numerical techniques have been investigated. Researchers have tried to address this problem from multiple dimensions, including time domain analysis, the multilevel single linkage method, the finite difference time domain technique, and 1-port and 2-port measurements. Neural networks are gaining popularity for material science based research as well, and are particularly suited to non-linear inverse profiling problems [16]. In this research we propose a neural network based methodology for passive REMS sensing. A neural network is applied to reconstruct the permittivity profile of a multi-section electro-material line for REMS sensor using complex input reflection coefficient of the backscattered wave.

1.7 Organization of the Thesis

The thesis is organized in the following way. After the introduction in chapter 1, the material properties and material characterization is briefly discussed in chapter 2. Chapter 3 covers the basics of Artificial Neural Networks (ANNs) along with a brief overview of the training algorithms. With this background knowledge, the first case of a lossless electro-material line is discussed in chapter 4. This is primarily a proof of concept/feasibility of the application of an ANN to the REMS sensor concept for a simple, lossless case. The physics of a thermo-responsive electro-material line warrants the need of developing the capability to backsolve complex permittivity. To explore the thermo-responsiveness of liquid crystals and materials at microwave frequencies, an experimental analysis of isopropyl alcohol and a thermotropic liquid crystal, 4-Cyano-4'-pentylbiphenyl (5CB), was carried out. A brief analysis of results is presented in chapter 5. As a first step, a neural network based method is demonstrated using a monopole probe in chapter 6. Three different methods based on the

neural network architecture are presented in this chapter. This ANN based methodology to reconstruct complex permittivity is applied to a multi-section electro-material line in chapter 7. With this analysis, the ANN is compared to a regression analysis specific to the REMS sensor application in chapter 8. The final chapter includes the concluding discussion highlighting the original contributions of this research and also future work related to this research.

CHAPTER II

MATERIAL CHARACTERIZATION

The response of a material to an applied electromagnetic field depends upon the displacement of free and bounded electrons by the electric field, and the alignment of atomic moments due to the magnetic field. Although the importance of magnetic materials for passive sensing applications can not be underestimated, the focus of this research is limited to the electrical properties of non-magnetic materials. Electrical properties of materials are determined using a complex permittivity ϵ , which describes the interaction of a material with an applied electric field. The permittivity can be written as :

$$\epsilon = \epsilon_o \epsilon_r \quad (1)$$

where ϵ is the complex permittivity, ϵ_r is the relative complex permittivity, and ϵ_o is the permittivity of free space. The relative complex permittivity is a dimensionless quantity defined by :

$$\epsilon_r = \epsilon'_r - j\epsilon''_r = \epsilon'_r(1 - j \tan \delta_e) \quad (2)$$

where ϵ'_r is the real part and ϵ''_r is the imaginary part. Dielectric loss angle is denoted by δ_e , and $\tan \delta_e$ is the dielectric loss tangent. The change in the material properties due to an applied electromagnetic field is explained at a microscopic level in terms of the electron energy bands and the magnetic moments [17]. At a macroscopic scale, these interactions are explained using Maxwell's equations:

$$\nabla \cdot \mathbf{D} = \rho \quad (3)$$

$$\nabla \cdot \mathbf{B} = 0 \quad (4)$$

$$\nabla \times \mathbf{H} = \mathbf{J} + j\omega\epsilon\mathbf{E} \quad (5)$$

$$\nabla \times \mathbf{E} = -j\omega\mu\mathbf{H} \quad (6)$$

and the constitutive relationships:

$$\mathbf{D} = \epsilon \mathbf{E} = (\epsilon' - j\epsilon'')\mathbf{E} \quad (7)$$

$$\mathbf{B} = \mu \mathbf{H} = (\mu' - j\mu'')\mathbf{H} \quad (8)$$

$$\mathbf{J} = \sigma \mathbf{E} \quad (9)$$

The electric field interacts with the material in two ways, (i) energy storage, and (ii) energy dissipation. Energy storage describes the lossless flow of energy between the field and the material, while the energy dissipation is caused by the electromagnetic energy absorption by the material. The real part of permittivity (ϵ'_r) represents the storage and the imaginary part (ϵ''_r) indicates the dissipation.

For an electromagnetic propagating wave, the characteristic impedance of the medium, η , and the wave propagation velocity, v , depend on the permittivity and permeability of the medium.

$$\eta = \sqrt{\frac{\mu}{\epsilon}} \quad (10)$$

$$v = \frac{1}{\sqrt{\mu\epsilon}} \quad (11)$$

The wave impedance of free space is 376.7Ω and the wave velocity in free space is $2.998 \times 10^8 m/s$. With a complex permittivity and/or complex permeability, the

imaginary part is a mathematical convenience for expressing loss [17]. The propagation of electromagnetic waves in a medium is described using a complex propagation coefficient γ .

$$\gamma = \alpha + j\beta = j\omega\sqrt{\mu\epsilon} \quad (12)$$

where ω is the angular frequency, α is the attenuation coefficient, and β is the phase coefficient. For high-conductivity materials, Eq. 12 is modified as :

$$\gamma = \alpha + j\beta = j\omega\sqrt{\mu\epsilon}\sqrt{1 - j\frac{\sigma}{\omega\epsilon}} \quad (13)$$

In case of high conductivity materials, $\sigma \gg \omega\epsilon$, meaning thereby that the conduction current is much larger than the displacement current. Ignoring the displacement current term, Eq. 13 is approximated as :

$$\gamma = (1 + j)\sqrt{\frac{\omega\mu\sigma}{2}} \quad (14)$$

where the skin depth is defined as :

$$\delta_s = \frac{1}{\alpha} = \sqrt{\frac{2}{\omega\mu\sigma}} \quad (15)$$

At microwave frequencies, the behavior of high conductivity materials is determined by the surface impedance.

$$Z_s = R_s + jX_s = \frac{E_t}{H_t} = (1 + j)\sqrt{\frac{\mu\omega}{2\sigma}} \quad (16)$$

where R_s is the surface resistance, X_s is the surface reactance, H_t is the tangential magnetic field and E_t is the tangential electric field.

Based on the value of conductivity, materials can be classified as *insulators*, with very low conductivity and having an imaginary part of permittivity usually assumed to be equal to zero ($\epsilon'' = 0$), *semiconductors*, with conductivity higher than dielectrics but less than conductors, and *conductors*, having conductivity in the range of 10^4 to $10^8(\Omega m)^{-1}$.

2.1 Dielectric Materials at Microwave Frequencies

The permittivity of a material is related to different physical phenomena depending upon the frequency range of interest. In the low frequency range, ion conductivity dominates ϵ'' , while in the microwave frequency range, the variation of permittivity is caused by dipolar relaxation [17].

2.1.1 Dipole Polarization

Dipole polarization or relaxation is the response of a population of dipoles to an external electric field. Although the *Debye* equation is based on the assumptions of ideal and non-interacting dipoles, the equation is applicable in most cases. In the Debye equation, the complex permittivity is expressed as:

$$\epsilon_r = \epsilon_{r\infty} + \frac{\epsilon_{r0} - \epsilon_{r\infty}}{1 + j\beta} \quad (17)$$

where $\epsilon_{r\infty} = \lim_{\omega \rightarrow \infty} \epsilon_r$, $\epsilon_{r0} = \lim_{\omega \rightarrow 0} \epsilon_r$,

$$\beta = \frac{\epsilon_{r0} + 2}{\epsilon_{r\infty} + 2} \omega \tau \quad (18)$$

τ is the relaxation time, and ω is the angular frequency.

Ionic conductivity contributes only toward losses in the material. At low frequencies, ϵ_r'' is dominated by the ionic conductivity in moist materials, however, the ionic conductivity decreases with an increase in frequency. The imaginary part of complex permittivity comprises dielectric loss (ϵ_{rd}'') and conductivity (σ) as shown in Eq. 19.

$$\epsilon_r'' = \epsilon_{rd}'' + \frac{\sigma}{\omega \epsilon_o} \quad (19)$$

2.1.2 Ferroelectricity

Dielectric materials are also classified based on the type and nature of the polarization they undergo. *Paraelectric* materials get polarized when an electric field is applied to

them. The polarization is linear and it returns back to the original state once the field is removed. *Pyroelectric* materials generate a temporary voltage when they are heated or cooled [17]. The change in temperature gives rise to a change in polarization, which in turn generates a voltage. If the temperature stays at the new value for some time, the pyroelectricity voltage disappears due to leakage currents. Pyroelectric materials are considered a subgroup of *piezoelectric* materials, which generate an electric field or electric potential in response to an applied mechanical stress.

Ferroelectric materials are a further subgroup of *pyroelectric* materials [17]. With an applied field, ferroelectric materials display a non-linear hysteresis effect of polarization. The permanent electric dipoles in the material causes the formation of a hysteresis loop. Ferroelectric materials can be maintained only below a certain specific temperature called the *Curie temperature*. Above the Curie temperature, the ferroelectric materials enter a paraelectric state. The relative permittivity of the ferroelectric materials rises sharply just below the Curie point and then quickly decreases just above the Curie point when the material has entered its paraelectric state. Ferroelectric materials are used in various newly developed applications and can potentially be used in the material line for the REMS sensor.

2.2 Techniques for Material Characterization

The methods for extracting material properties at microwave frequencies can be classified as resonant and non-resonant methods. Non-resonant methods are used to characterize the material over a broad frequency range, while the resonant methods are focused at getting accurate knowledge of the electrical properties of the material at a single frequency or several discrete frequencies. Both the methods can be used in combination to obtain accurate knowledge of materials over a range of frequencies.

The properties of materials are deduced from their impedance and wave velocities in the non-resonant methods. When an electromagnetic wave propagates from one

medium to another, the characteristic impedance changes and a part of wave is reflected back. This reflection from the interface depends upon the dielectric properties of the material, which can be extracted from the measurement of the reflection coefficient. Non-resonant methods include reflection, and transmission/reflection methods. There are two further types of reflection methods, (i) open-circuit reflection, and (ii) short circuit reflection. In the *open-reflection method*, the measurement fixture is usually a coaxial dielectric probe and is used for measuring the electrical properties of non-magnetic materials. *Short-reflection methods* are used to measure the magnetic permeability of materials with electrical properties not sensitive to other measurements [18]. Reflection methods are also used to measure the surface impedance of high conductivity materials with the thickness of the sample several times larger than the skin depth. The surface resistance of high temperature superconducting thin films can be measured using this method [19]. The *transmission/reflection method* is primarily used for characterizing low conductivity materials and measurement of surface impedance of high conductivity materials. The permeability and permittivity of the material is measured using the reflection from the material and transmission through the material. The material under test is inserted in a piece of transmission line which causes a change in the characteristic impedance of the transmission line. The material properties can then be derived by comparing the coefficients with the sample loaded transmission line.

The resonant methods are widely used for low-loss non-magnetic dielectrics, and can be broadly classified into two sub-categories: resonator methods, and resonant-perturbation methods. The resonance frequency and the quality factor of a dielectric resonator with given dimensions are function of its permittivity and/or permeability. The sample is sandwiched between two conducting plates of known properties. The dielectric sample functions as a resonator, and the dielectric constant and loss tangent are determined from its resonant frequency and quality factor. The TE_{011} mode is

commonly used as this mode does not have a transverse electric field between the sample and the conducting plates, and therefore the measurements are not affected by presence of a small gap between the sample and the plates. Properties of materials with high dielectric constants, low loss materials and anisotropic materials can be measured using resonator methods [20,21]. In the resonant perturbation methods, the sample is introduced into a resonator which causes a change in the resonant frequency and the quality factor of the resonator. Electrical and/or magnetic properties of the material are derived from the changes in the resonant frequency. The resonant perturbation methods are further classified into three subgroups: cavity shape perturbation, wall loss perturbation and material perturbation. Cavity shape perturbation methods are used to adjust the resonant frequency of a cavity. In wall loss perturbation methods, the material under test is introduced into the cavity which shifts the resonant frequency and quality factor. This method is also called the cavity perturbation method and is used for characterizing low-loss materials.

Material characterization at microwave frequencies has been an active research area for quite some time and researchers have addressed this problem from different dimensions. Owing to the inherent non-linear nature of this problem, analytical techniques have limited scope. Various numerical techniques have been explored in conjunction with the resonant and non-resonant methods.

The propagation of electromagnetic waves through a stratified medium can be modeled using transmission line equations. A time domain analysis for wave propagation in inhomogeneous medium is presented using the Lagrangian approach for piecewise uniform lossy transmission lines in [22]. Based on an objective function defined as the mean-square error between the measured data and the analytical data, the multilevel single linkage method is used to reconstruct the permittivity and conductivity profile of layered media in [23]. This method utilizes a priori knowledge of

the parameters to improve the parameter bounds and to develop the impedance profile. The method is successful in a noise free environment, and requires an enlarged data set to offset the adverse effects of noise. Researchers have been employing methods such as the finite difference time domain technique to study the effect of material properties on the reflection coefficient [24]. With this approach, the dielectric constant of the dispersive medium is written as a rational polynomial function and the constitutive relationship is derived in the time domain. The material properties can be extracted from the information contained in the reflected or transmitted waves using the 1-port and 2-port measurements as well, however, this method is limited only to the real part of effective permittivity [25].

Artificial neural networks have been employed across a wide field of applications, including neuromodeling of microwave circuits based on space mapping technology [26], RF and microwave design using electromagnetics based training for passive circuits and physics based training for active devices [27, 28], and inverse electromagnetic problems [29], [30], and [31]. Exploiting a priori knowledge of the geometry, neural networks incorporating a back-propagation algorithm were able to retrieve the radius position and dielectric permittivity of a circular cylinder [32]. Neural networks have also demonstrated the ability to reconstruct the permittivity profile of homogeneous cylinders in free space and detecting the position of cylinders [33]. The effective use of neural networks to determine non-smooth, one-dimensional profiles of an inhomogeneous layer has been investigated with noisy data by Yaman and Simcsek [34]. Neural networks are particularly suited to non-linear inverse profiling problems for material characterization [16]. In next chapter, the basic concepts of an ANN are discussed along with brief description of different algorithms and its application to the proposed research problem.

The concepts of microwave propagation and transmission line theory form the

basis of material characterization techniques at microwave frequencies. These concepts are discussed in detail in [15], and therefore are not discussed at length in this chapter.

CHAPTER III

ARTIFICIAL NEURAL NETWORKS

The idea of neural networks evolved in late 19th century to understand how the human brain functions. The concept of decentralized network units (neurons) was introduced in 1943 when McCulloch and Pitts developed the first mathematical model of a neuron [35]. Inspired from brain function, the neural network is generally used to solve artificial intelligence problems without requiring a model of the system. Neural networks are adjusted and trained to solve problems that are difficult to solve using conventional techniques. In simple words, neural networks are extremely useful in recognizing patterns and fitting functions and are specially well suited to solving complex non-linear problems.

A neural network has three main components: 1) neurons/architecture , 2) training algorithm, and 3) training data. Neurons are the main building blocks which form the architecture of the network. The training algorithm uses training data to train the network to solve the problem while minimizing the error. In the forthcoming sections, each of the component is briefly discussed.

3.1 Neuron Architecture

3.1.1 Single Neuron

A single neuron with a single input p is shown in Fig.7. The scalar input p is multiplied with a weight w and passed on to the summer. The other input 1 is multiplied with the bias/offset b and also passed onto the summer. A neuron may or may not have the bias/offset input. The output n (net input) of the summer then goes through the activation function f (some authors write it as a transfer function). The output a is the output of the neuron. The bias/offset is similar to a weight except that the bias

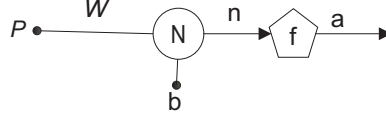


Figure 7: Single input neuron with weight, bias and activation function

has always a fixed input of 1. The activation function is chosen by the designer, while the weight and bias (if used) are adjusted by some learning rule [36]. The output function is shown in Eq. 20.

$$a = f(wp + b) \quad (20)$$

Due to size and structure of data matrices, one neuron has usually more than one input. A neuron with R inputs is shown in Fig. 8. Scalar inputs p_1, p_2, \dots, p_R are multiplied with corresponding weights of a weight matrix $w_{1,1}, w_{1,2}, \dots, w_{1,R}$. If bias b is used and W is the weight matrix then the output would be given by Eq. 21. In this case the weight matrix is only a row vector, and the output n is given by Eq. 22. The output a is given by Eq. 23.

$$n = WP + b \quad (21)$$

$$n = w_{1,1}p_1 + w_{1,2}p_2 + \dots + w_{1,R}p_R + b \quad (22)$$

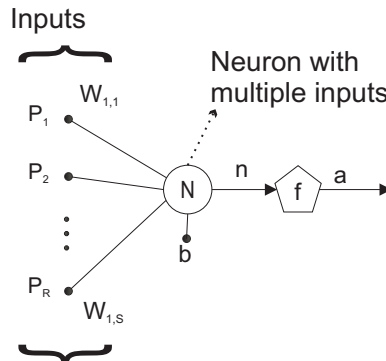


Figure 8: Single neuron with multiple inputs and one output and one activation function

$$a = f(WP + b) = fn \quad (23)$$

3.1.2 *Layer of Neurons*

For most of the systems, one neuron is insufficient. Therefore multiple neurons are used in parallel. A set of neurons operating in parallel is called a *layer* of neurons. One such layer comprising S neurons is shown in Fig. 9. Each input is connected to each neuron and the weight matrix has S rows. In the matrix, the row index of an element indicates the destination neuron associated with that weight, as shown in Eq. 24.

$$w = \begin{pmatrix} w_{1,1} & w_{1,2} & \dots & w_{1,R} \\ w_{2,1} & w_{2,2} & \dots & w_{2,R} \\ \cdot & \cdot & \cdot & \cdot \\ \cdot & \cdot & \cdot & \cdot \\ \cdot & \cdot & \cdot & \cdot \\ w_{S,1} & w_{S,2} & \dots & w_{S,R} \end{pmatrix} \quad (24)$$

The number of neurons is usually not equal to the number of rows, as this equivalence has no significance [36]. All neurons usually have the same transfer function, however for complex cases, different transfer functions can be assigned to different neurons [36].

3.1.3 *Multiple Layers of Neurons*

There can be a variety of systems for which one layer of multiple neurons might be insufficient. For such systems, a network with multiple layers, as shown in Fig. 10, is used. These layers are also called *hidden layers*. Each layer has its own weight matrix W , bias vector b , net input vector n and output vector a . For identification, the layer number is marked with a superscript. W^1 , W^2 and W^3 are the weight matrices for

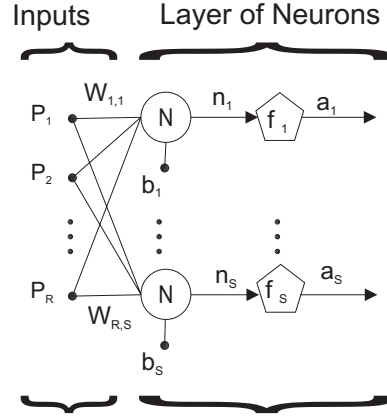


Figure 9: One layer of multiple neurons

the first, second and third layer, respectively. For R inputs, and S^1 neurons in the first layer, the second layer can be considered as a layer with S^1 inputs, S^2 neurons and a $S^1 \times S^2$ weight matrix. The input to the second layer is a^1 and the output, which is the input to layer three, is a^2 . The final output is a^3 , which is given by Eq. 25.

$$a^3 = f^3(W^3 f^2(W^2 f^1(W^1 p + b^1) + b^2) + b^3) \quad (25)$$

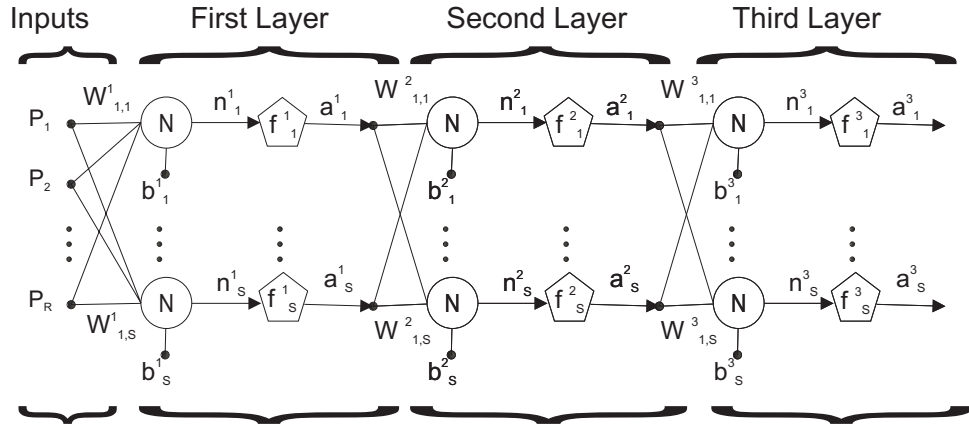


Figure 10: Three layers of multiple neurons

3.1.4 Transfer Function (Activation function)

A linear or non linear transfer function is used depending upon the specifications of problem that the neuron is trying to solve. The three most commonly used transfer functions are the *hardlimit transfer function*, the *linear transfer function*, and the *log sigmoidal transfer function* shown in Fig. 11, Fig. 12 and Fig. 13, respectively [35]. The hard limit transfer function limits the output of neuron to either 0 or 1 depending upon the input argument. It is most commonly used in classification problems. The linear transfer function has an output equal to its input and is used in Adaline networks [36]. The log sigmoidal transfer function takes any input from minus infinity to plus infinity and compresses the output into the range 0 to 1 according to the expression in Eq. 26. It is the most typically used transfer function in backpropagation algorithms. Log sigmoidal and tan sigmoidal transfer functions are differentiable and are more suited to function approximation problems.

$$a = \frac{1}{1 + e^{-n}} \quad (26)$$

3.2 Training Algorithms

Backpropagation of error requires the activation function to be differentiable. Its implementation is known as the *Delta rule*, which is given by Eq. 27 for the j^{th}

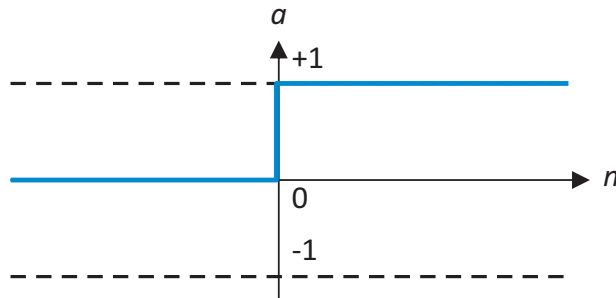


Figure 11: Hard Limit Transfer Function

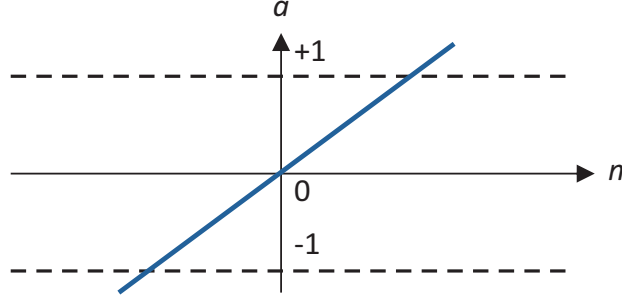


Figure 12: Linear Transfer Function

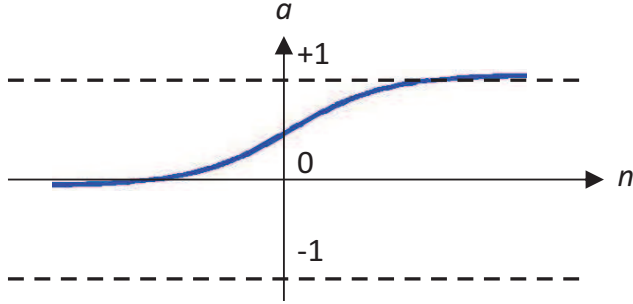


Figure 13: Log Sigmoidal Transfer Function

neuron and the i^{th} weight, where α is the constant learning rate, t_j is the target output, y_j is the actual output and $g(x)$ is the activation function.

$$\Delta w_{ji} = \alpha(t_j - y_j)g'(h_j)x_i \quad (27)$$

In simple words, the purpose of the training algorithm is to minimize the error as quickly and as accurately as possible. Training algorithms can be divided into two broad categories based on the method by which they are developed: using heuristic techniques and using standard numerical optimization techniques. Each category has different training algorithms as listed below.

- Heuristic techniques
 1. Gradient descent and Gradient descent with momentum
 2. Variable learning rate

3. Resilient backpropagation

- Standard numerical optimization techniques

1. Conjugate gradient
2. Quasi Newton
3. Levenberg Marquardt

3.2.1 Gradient Descent

In the gradient descent algorithm, network weights are moved along the negative of the gradient of the performance function. If steps are taken proportional to the gradient, one reaches the local minimum [36]. Gradient descent, gradient descent with momentum, variable learning rate, and resilient back propagation, all operate in batch mode. In batch mode, weight and biases of network are updated after the entire training has been applied to the network. The learning rate (denoted by α or l_r) is a critical parameter in every algorithm. If l_r is too large, the algorithm may become unstable, and if l_r is too small, the algorithm converges too slowly. Gradient descent and gradient descent with momentum, are both too slow for most practical problems [36].

3.2.2 Variable Learning Rate

In a variable learning rate algorithm, as the name depicts, the optimal training rate changes during the training process. The learning step is kept as large as possible while keeping the learning stable. If new error exceeds old error by more than a pre-defined ratio (generally 1.04), the new weights are discarded and the learning rate is decreased by a ratio (generally 0.7). Otherwise, if the new error is low, the learning rate is increased (usually by a factor of 1.05)

3.2.3 Resilient Back Propagation

Multilayer networks typically use a sigmoidal transfer function in hidden layers, which are often called squashing functions because they compress the infinite input range to a finite output range. Their feature that the slope must approach to zero as the input gets large, poses a problem for steepest descent training. Even when weights are far from their optimal values, the gradient can have small values causing at most small change in weight and biases. The resilient back propagation algorithm eliminates the harmful effects of partial derivative magnitudes. In this algorithm, only the sign of the derivative is used to determine the direction of the weight update. The size of weight change is determined by a separate update value. If the derivatives have the same sign for two consecutive iterations, the update value is increased. In case of a sign change, the update value is decreased [37].

3.2.4 Conjugate Gradient Algorithms

The basic back propagation algorithm adjusts the weight along the negative gradient (steepest descent direction). Although the function decreases, it does not necessarily produce the fastest convergence. In conjugate gradient algorithm, a search is performed along conjugate directions and the step size is adjusted in each iteration.

The term *conjugate direction* stems from the word conjugate, meaning, having features in common but opposite or reverse in some particular. In the context of error minimization in neural networks, suppose we have an estimate of minimum of a function $f(a)$ in a two dimensional problem. To refine the minimum, a line search is carried out in some direction u along the line $a + u\lambda$. This is a one dimensional minimization to find the value of λ which minimizes the function $f(a + u\lambda)$. For finding minima of $f(a)$, this process is repeated through n cycles along n direction vectors which span the parameter space. This can end up zigzagging inefficiently in small steps. After a line search is performed along a direction u , the objective is to

choose a new direction v , so that minimizing along v will not *spoil* minimization along u . As function f is already minimized along u , $\nabla f \cdot u = 0$. In order to not interfere with u minimization, the gradient should remain perpendicular to u , $u^T A v = 0$. The two vectors u and v having this property are *conjugate*. If a function is minimized along a series of conjugate directions, the minimum would be reached efficiently. As the conjugate gradient methods were invented purely for quadratic functions, one pass through the set will reach the exact minima [38]. Otherwise the cycle must be repeated a number of times.

Four common conjugate gradient methods are described here.

3.2.4.1 Fletcher-Reeves Update

In this algorithm, the first step is taken in the steepest descent direction and then a line search is performed to find the optimal step size in the conjugate direction [39].

$$p_0 = -g_0 \tag{28}$$

$$x_{k+1} = x_k + \alpha_k p_k \tag{29}$$

$$p_k = -g_k + B_k p_{k-1} \tag{30}$$

In the Fletcher Reeves update, B_k is the ratio of the norm squared of the current gradient to the norm squared of the previous gradient.

$$B_k = \frac{g_k^T g_k}{g_{k-1}^T g_{k-1}} \tag{31}$$

3.2.4.2 Polak-Ribiere' Update

This algorithm is similar to Fletcher-Reeves update except the way the constant B_k is computed. In Polak-Ribiere' algorithm, B_k is the ratio of the inner product of the

previous change in gradient and the current gradient, to the norm squared of the previous gradient. The Fletcher-Reeves algorithm has a lower storage requirement compared to the Polak-Ribiere' algorithm [36].

$$B_k = \frac{\Delta g_{k-1}^t g_k}{g_{k-1}^t g_{k-1}} \quad (32)$$

3.2.4.3 *Powell-Beale Restarts*

For all conjugate gradient algorithms, the search direction is periodically reset to the negative of the gradient. A standard reset point occurs when the number of iterations equals the number of weights and biases. In the Powell-Beale algorithm, the technique restarts if very little orthogonality is left between the current gradient and the previous gradient [40] and [41]. This technique has storage requirements higher than the Fletcher-Reeves update [36].

3.2.4.4 *Scaled Conjugate Gradient*

A line search computes the network response to all training inputs several times and thus gets computationally expensive. The scaled conjugate gradient algorithm avoids the tedious line search by using the step size scaling mechanism with the conjugate gradient approach to save time [42]. The main idea is to introduce a scalar quantity to regulate the indefiniteness of the Hessian. Storage requirements are the same as the Fletcher-Reeves update and the algorithm may require more iterations to converge, but the computation is significantly reduced as no line search is involved.

3.2.5 **Quasi Newton Algorithms**

Newton's method is an alternative to conjugate gradient methods for fast optimization, and involves the update :

$$x_{k+1} = x_k - A_k^{-1} g_k \quad (33)$$

where A_k^{-1} is the Hessian of the performance index of current values of weights and biases. Newton’s method often converges faster than the conjugate gradient method, but the Hessian is expensive to compute. In the Quasi Newton method, an approximate Hessian is updated at each iteration instead of being recomputed from scratch [36].

3.2.5.1 Broyden Fletcher Goldfarb and Shanno (BFGS) Algorithm

This algorithm, most commonly known as the BFGS algorithm, requires more computation and storage than the conjugate gradient algorithm and is not suited to large networks [36].

3.2.5.2 One Step Secant Algorithm

The one step secant algorithm is an effort to bridge the gap between conjugate gradient and quasi-Newton algorithms. Instead of storing the complete Hessian matrix at each iteration, it assumes that the previous Hessian was an identity matrix [43]. It requires less storage and computation than the BFGS algorithm but more than conjugate gradient algorithms.

3.2.6 Levenberg Marquardt Algorithm

This algorithm was designed to approach second order training speed without computing the Hessian. The Hessian is approximated as $H = J^T J$ and the gradient as $g = J^T e$, where J is the Jacobian that contains the first derivative of network errors with respect to weight and biases, and e is the vector of network errors [44]. The Jacobian is computed through a standard back propagation technique which is much less complex than computing the Hessian [45]. An approximation to the Hessian matrix is:

$$x_{k+1} = x_k - [J^T J + \mu I]^{-1} J^T e \quad (34)$$

In the Newton method μ is zero, while in a gradient descent with small size, μ is large. As the Newton method is faster and more accurate close to error minimum, the aim is to shift to the Newton method as quickly as possible.

The main drawback of Levenberg Marquardt is that it requires the storage of a quite large matrix. The size of the Jacobian is $Q \times n$, where Q is the number of training sets and n is the number of weights and biases. The Jacobian can be divided into equal sub matrices, and the Hessian is expressed as :

$$H = J^T J = J_1^T J_1 + J_2^T J_2 \quad (35)$$

where J is divided into two equal matrices J_1 and J_2 .

3.3 Training Data

Training data are used for training the network through the selected algorithm. The data can be generated using an analytical / numerical model or through experiments. The available training data are often divided into three parts: the training set, the validating set, and the testing set. Most of the data is used in the learning phase for creating the model. The learning set uses around 70-80% of the data, while validating and testing sets are typically allocated 15% and 5% of the data set, respectively. The validating set is used to validate the model and then it is tested for usability using the testing set. The size of data set becomes extremely important in the case of complex non-linear function approximation problems, where it is very difficult to converge to the correct model/weights with a small data set. The larger data sets can be difficult to create, especially when training data are generated using experiments.

In this research, the training data are generated using analytical and numerical techniques. The type and amount of training data are described for each case of electro-material line in the forthcoming chapters.

CHAPTER IV

LOSSLESS ELECTRO-MATERIAL LINE

The passive wireless sensor based on reflected electro-material signatures (REMS), consists of an electro-material line, the reflector circuitry and the RF reader, as shown in Fig. 3 in section 1.4. The electro-material line is routed between the ground plane and the top trace of the RF tag's microstrip transmission line. The time profile of temperature, or any other target variable being sensed, is recorded in the spatially distributed permittivity profile of the electro-material line as described in Fig. 2 in section 1.3. Reconstructing the medium properties from the waves backscattered from a REMS sensor is a non-linear inverse problem, which is quite similar to 1D inverse scattering problems. Owing to the non-linear nature of the problem, analytical techniques have limited application and thus various numerical techniques have been investigated [22]. Researchers have explored methods such as the finite difference time domain technique [24] and 1-port and 2-port measurements [25] for extracting the material properties using the reflection/transmission methods. Artificial neural networks have been employed across a wide field of applications, including RF and microwave design [27, 28]; and inverse electromagnetic problems [29], [30], [34], and [31]. Neural networks are gaining popularity for material science based research as well, and are particularly suited to non-linear inverse profiling problems [16].

In this chapter, a neural network based method is demonstrated to reconstruct the permittivity profile of a multi-section lossless electro-material line for a REMS sensor using the complex input reflection coefficient of the backscattered wave.

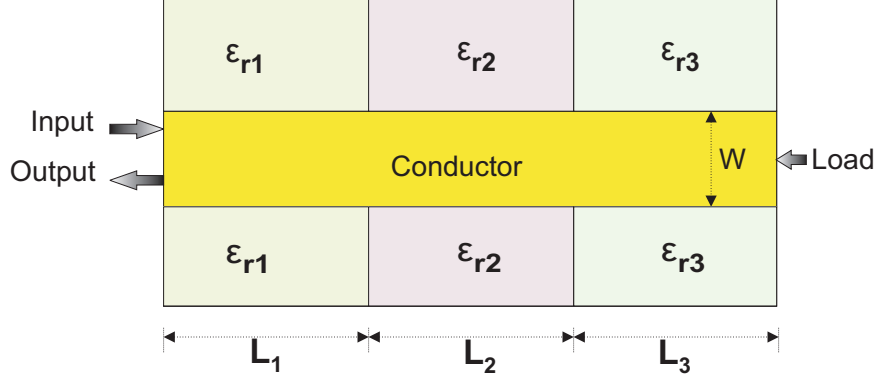


Figure 14: The microstrip line model with three discrete segments having different permittivity profiles, terminated in a load to emulate a REMS sensor with three wells of sensor material.

4.1 *Calculating the Reflection Coefficient from a Transmission line Model*

To test the REMS concept, the sensor is modeled using three cascaded microstrip transmission lines, emulating a three part step discontinuity in the electro-material line. The dimensions of each cascaded microstrip line are tabulated in Table 1. Different dielectric materials in the segments are used to emulate a REMS sensor with three wells of sensor material. The line is terminated in a resistive load. As the transmission line geometry is not specifically designed for a characteristic impedance of 50Ω , this load causes part of the wave to be absorbed and part reflected back. The microstrip line model with three discrete segments having different permittivity profiles is shown in Fig. 14.

Table 1: Dimensions of cascaded microstrip transmission lines

Length	1.25cm
Width	0.5cm
Substrate Height	0.05cm

The RF reader of the REMS sensor will extract the information from the backscattered wave. The complex reflection coefficient Γ contains the information about the spatially distributed permittivity profile of the electro-material line. To test this idea,

the relative permittivity, ϵ_r , of each segment was swept across a range of values for the frequency range of 1-5 GHz, and the values of reflection coefficient, Γ_{IN} , at the input of the system were computed. Each transmission line acts as a two port network cascaded together as shown in Fig. 15.

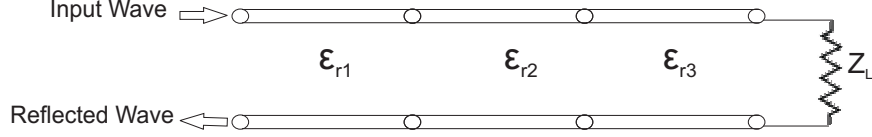


Figure 15: Three transmission lines cascaded together and terminated in a load.

The complete system of the cascaded lines is analyzed in terms of S-parameters using signal flow graphs as shown in Fig. 16. The input reflection coefficient is computed using Eq. 36 [15].

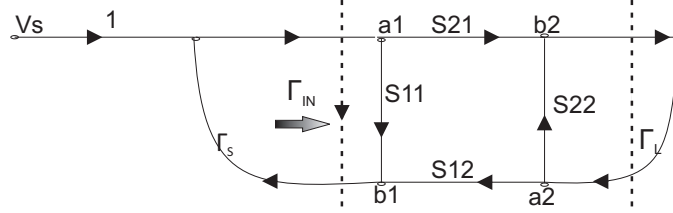


Figure 16: Signal Flow Graph for calculating Γ

$$\Gamma_{IN} = \frac{b_1}{a_1} = S_{11} + \frac{S_{12}S_{21}\Gamma_L}{1 - S_{22}\Gamma_L} \quad (36)$$

The complex-valued reflection coefficient contains information about magnitude as well as phase, and both will be used by the inversion algorithm. To demonstrate how the frequency-swept measurement of an RF reader changes for slight perturbations in the permittivity profiles, the dielectric constant of the second bin was changed for four different values, as illustrated in Fig. 17, and the reflection coefficient was calculated for each case. The effect on magnitude and phase of Γ_{in} , between four values of ϵ_{r2} , with $\epsilon_{r1} = 2.5$ and $\epsilon_{r3} = 3.5$, is shown in Fig. 18 and Fig. 19, respectively. Significant

alterations are observed in the magnitude and phase of the wave scattered out of the tag. Theoretically, every material profile will produce a unique frequency sweep - although designing a wide range of switchable loads (Z_A , Z_B , and possibly more) will greatly affect measurement resolution and sensitivity.

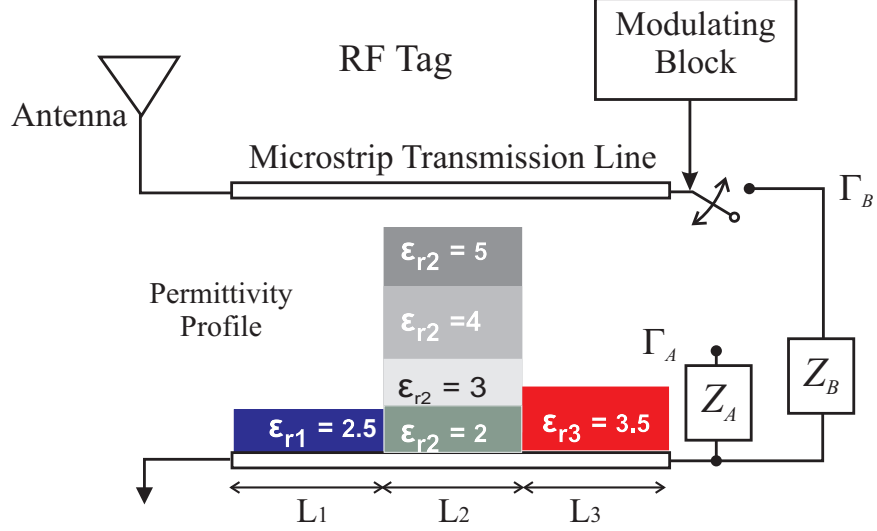


Figure 17: The transmission line model of the RF tag, illustrating four changing permittivity profiles of the center well of the REMS sensor.

4.2 Training Algorithm: Comparison and Selection

The complex reflection coefficient of the 3 section electro-material line is used as the training data for the neural network. The other two components of the network are the network architecture and the training algorithm. The weights described in the chapter 3 must be determined by a training process that attempts to match the actual output of the neural network with the desired output for a training data set. Function approximation problems are typically solved using backpropagation algorithms, which require the activation function to be differentiable. A common implementation is known as the *delta* rule, given by Eq. 27, which provides the adjustment in weights during one step of the training process.

The training algorithm must minimize the error between the desired and actual

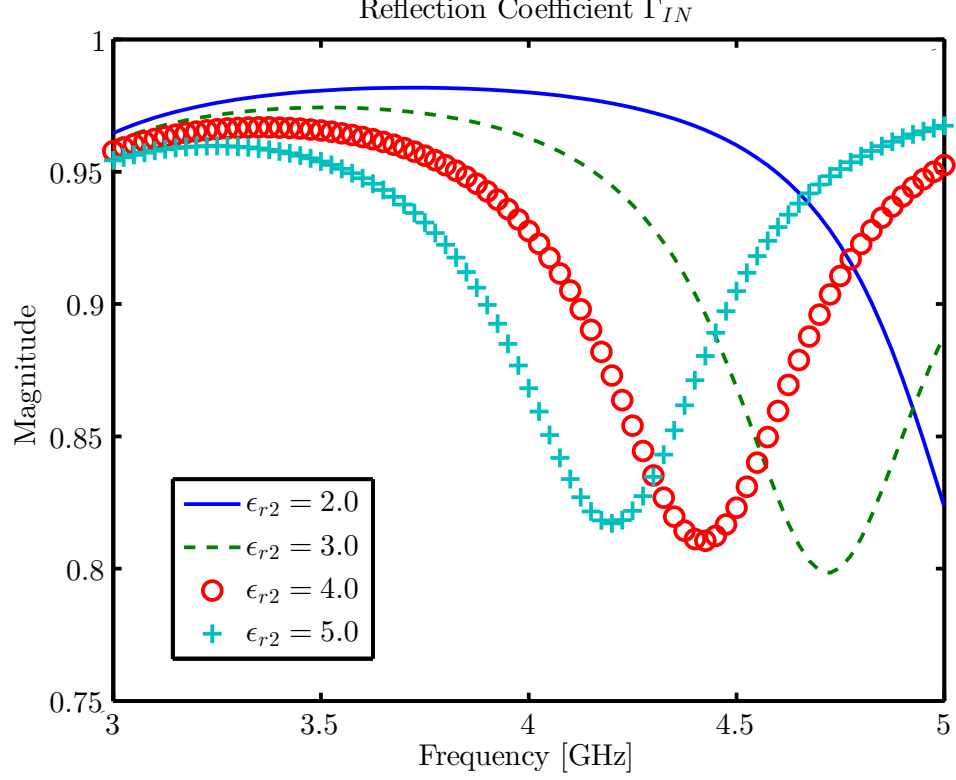


Figure 18: Magnitude of Γ_{IN} for $\epsilon_{r2} = 2, 3, 4$ and 5 calculated from the signal flow graph.

network outputs as quickly as possible. The learning rate (denoted by α or l_r) is a critical parameter in every algorithm. If l_r is too large, the algorithm may be unstable, and if l_r is too small, the algorithm converges too slowly. Each algorithm has its own merits and demerits depending upon the type of problem and computing resources. The gradient descent and gradient descent with momentum algorithms are considered too slow for practical problems [36]. Conjugate gradient methods were invented purely for quadratic functions, and some require excessive memory while others require more iterations to converge. Newton's method is an alternative to conjugate gradient methods for fast optimization, and often converges faster than the conjugate gradient method, but it involves the Hessian which is expensive to compute. In the quasi-Newton method, an approximate Hessian is updated at each iteration instead of being recomputed from scratch [36]. The Broyden, Fletcher, Goldfarb, and Shanno

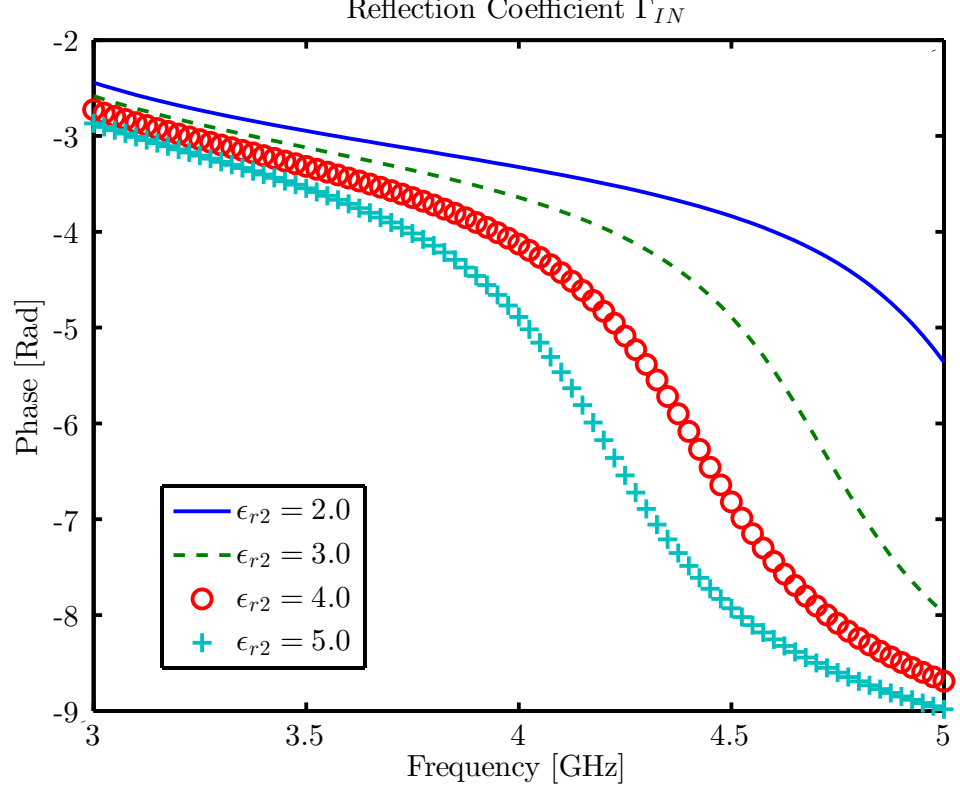


Figure 19: Phase of Γ_{IN} for $\epsilon_{r2} = 2, 3, 4$ and 5 calculated from the signal flow graph.

(BFGS) algorithm requires more computation and storage than the conjugate gradient algorithm and is not suited to large networks [36]. The one step secant algorithm is an effort to bridge the gap between conjugate gradient and quasi-Newton algorithms. In terms of accuracy (mean square error), speed, and memory requirements, which algorithm performs best depends upon a number of factors including the problem complexity, the number of points in the data set, weights, biases, the desired accuracy, and the type of problem (pattern recognition or function approximation). For a function approximation problem having a network with a few hundred weights, the Levenberg Marquardt (LM) algorithm often converges the fastest [36].

A number of simulations were carried out to determine the best algorithm, with the result that the LM algorithm exhibited superior absolute average error and computation time. The algorithm was designed to approach second order training speed without computing the Hessian H , instead using the approximation $H = J^T J$, where

J is the Jacobian containing the first derivative of network errors with respect to weights and biases. The gradient is computed as $g = J^T e$, where e is the vector of network errors [44]. The Jacobian is computed through a standard back propagation technique which is much less complex than computing the Hessian [45]. The algorithm is described in Eq. 34.

4.3 Application of Neural Networks for Extracting Material Properties (ϵ_r)

As a first step in using a neural network to extract material parameters, a simpler model is used. The electro-material line is assumed to be lossless ($\epsilon_r'' = 0$, $\epsilon_r = \epsilon_r'$). The dielectric constant, ϵ_{r2} , of the center segment of a 3-step microstrip line is varied from 2-8 with a step size of 0.1, while ϵ_{r1} and ϵ_{r3} were fixed at 3 and 3.8, respectively, as shown in Fig. 20. The dimensions and properties of this simple model are given in Eq. 37 - Eq. 45. A data set containing the magnitude and phase of Γ_{in} was generated for frequencies from 5 to 6 GHz with a step size of 100 MHz. The step size of 100 MHz was chosen to keep the data matrix dimensions within the computing capability of a modest desktop computer; it was observed that frequency steps smaller than 100MHz did not increase the accuracy of the results. The magnitude and phase values were combined in the data matrix D , which has the form shown in Eq. 46.

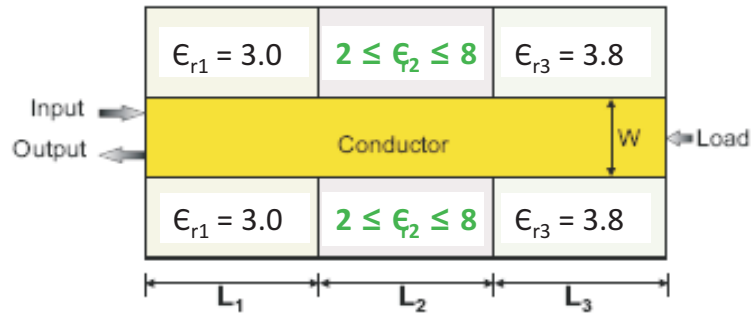


Figure 20: Overhead view on a PCB of a simple model of an electro-material line with $\epsilon_{r1} = 3$, $\epsilon_{r3} = 3.8$, and $2 \leq \epsilon_{r2} \leq 8$

$$\epsilon_{r1} = 3.0 \quad (37)$$

$$2 \leq \epsilon_{r2} \leq 8 \quad (38)$$

$$\Delta\epsilon_{r2} = 0.3 \quad (39)$$

$$\epsilon_{r3} = 3.8 \quad (40)$$

$$L_1 = L_2 = L_3 = 1.25cm \quad (41)$$

$$W = 0.5cm \quad (42)$$

$$h = 0.05cm \quad (43)$$

$$f = 5GHz \rightarrow 6GHz \quad (44)$$

$$\Delta f = 100MHz \quad (45)$$

$$D = \begin{bmatrix} |\Gamma| \\ \angle\Gamma \end{bmatrix} \quad (46)$$

For the initial test, $|\Gamma|$ and $\angle\Gamma$ were matrices of dimensions 11×61 , corresponding to 11 frequencies and 61 different values of ϵ_{r2} . A finer increment of the dielectric constant, 0.01 for instance, might improve the accuracy of the network model, but at a cost of increasing each matrix to 11×601 . The neural network with 10 neurons in single layer was trained using ϵ_{r2} in the range from 2-8. The neural network architecture is shown in Fig. 21. In this simple case, only ϵ'_{r2} is reconstructed and it corresponds to one neuron in the output layer. Once the network is trained and validated, it is then tested using the phase and magnitude of Γ_{in} generated from electro-material line with $\epsilon_{r2} = 2.1$, and 4.75. The results are shown in Table 2, which highlight a very accurate estimate of ϵ_{r2} with % error less than 1%.

In the next step, ϵ_{r1} and ϵ_{r3} were also varied as the frequency was swept across the 5-6 GHz range with a step size of 100 MHz. Values of ϵ_{r1} , ϵ_{r2} , and ϵ_{r3} were varied from 2-5 with a step size of 0.1. The resulting data matrix had dimensions $22 \times 29,971$.

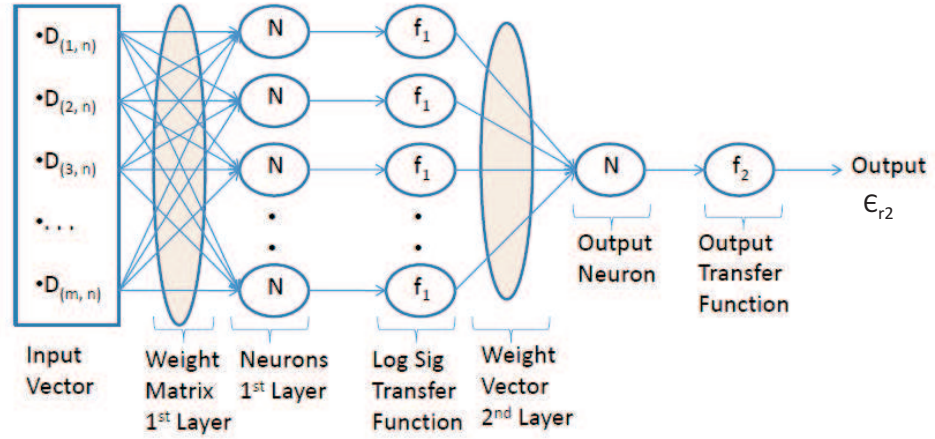


Figure 21: The neural network architecture with 10 neurons in the hidden layer, and one neuron in the output layer.

Table 2: Results for backsolving ϵ'_{r2} using a neural network with Levinberg Marquardt backpropagation algorithm.

	Target 1	NN Output	% error	Target 2	NN Output	% error
ϵ'_{r1}	3	3		3	3	
ϵ'_{r2}	2.1	2.12	0.9%	4.75	4.769	0.4%
ϵ_{r3}	3.8	3.8		3.8	3.8	

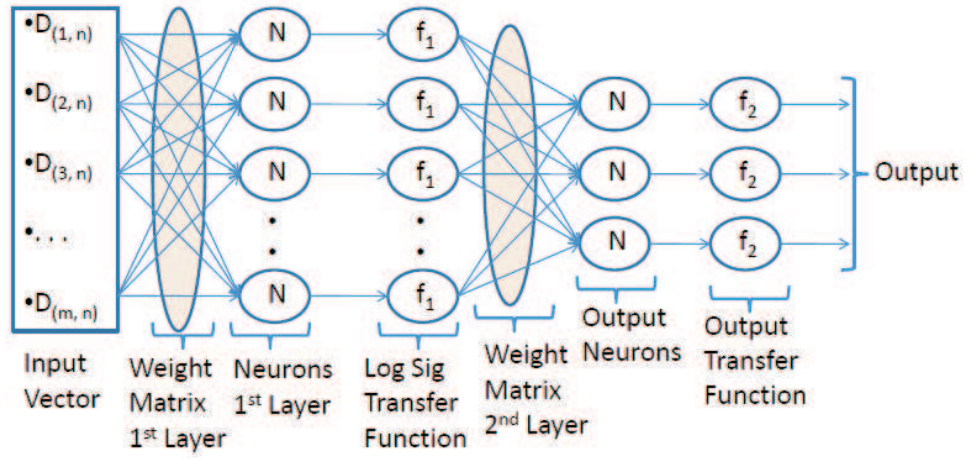
After training, the Levenberg Marquardt algorithm with 10 neurons in a single layer was able to produce relative permittivity values within ± 0.3 of the actual values, as summarized for three examples in Table 3.

The first two tests were carried out with a single neuron layer. Additional tests were carried out with single layer networks with 5, 10, 15, 20 and 25 neurons, and a two layer network with 10 neurons each. The neural network architecture for reconstructing ϵ_{r1} , ϵ_{r2} and ϵ_{r3} with one hidden layer is shown in Fig. 22. The output layer has three neurons corresponding to the three different permittivity values the network is backsolving.

The results were compared in terms of error and coefficient of regression analysis. Each network was tested for the set of permittivity values shown in Eq. 47 in matrix T . The rows of T correspond to ϵ_{r1} , ϵ_{r2} and ϵ_{r3} , while the columns show the set

Table 3: Comparison of actual values of $\epsilon_{r1,2,3}$ vs neural network output

	Actual Values	Neural Network output	Error
Set1	4	4.115	0.115
	4	4.024	0.024
	4	3.985	-0.015
Set2	2	2.018	0.018
	2.3	2.334	0.034
	4.8	4.501	-0.299
Set3	3	3.255	0.255
	2.5	2.495	0.005
	4.5	4.238	0.262

**Figure 22:** ANN architecture for backsolving permittivity profile of a microstrip line structure emulating a 3-bin electro-material line

of dielectric constants presented to the network at each time. It was observed that a single layer with 20 or 25 neurons is best suited in terms of absolute mean error and computation efficiency. The % errors for 20 neurons in the absence of noise are shown in matrix $\%E_{20}$ in Eq. 48.

$$T = \begin{bmatrix} 2.1 & 2.5 & 3.5 \\ 3.5 & 3.5 & 3 \\ 4.9 & 4.5 & 4 \end{bmatrix} \quad (47)$$

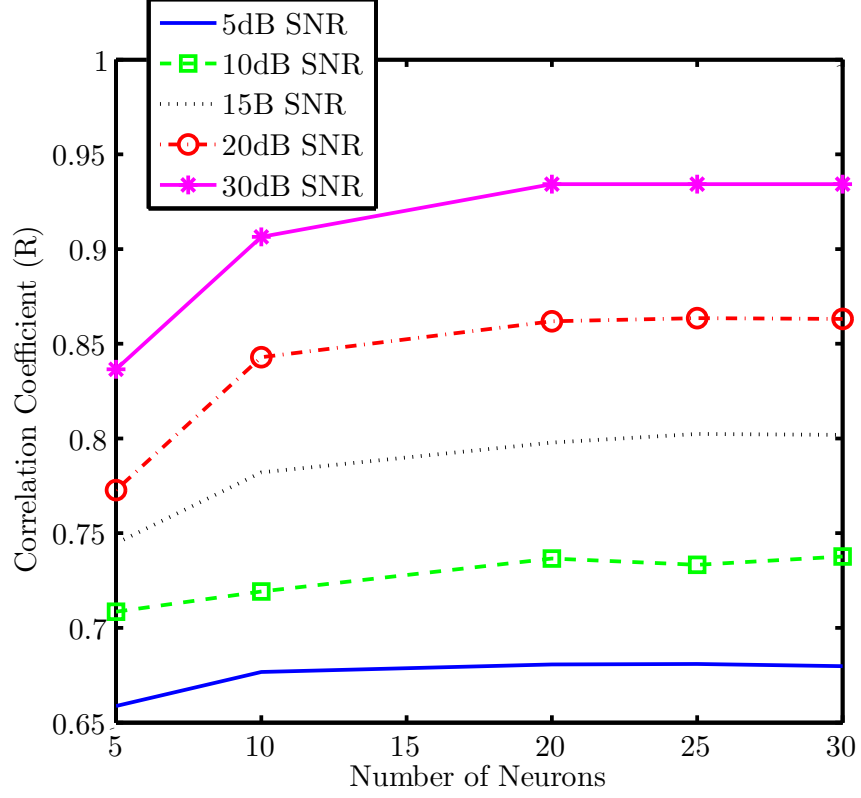


Figure 23: Correlation coefficient (R) of regression analysis plotted against the number of neurons for a network trained with data having white Gaussian noise. Number ‘30’ on the X-axis represents two hidden layers of 10 neurons each

$$\%E_{20} = \begin{bmatrix} 4.6\% & 1.04\% & 0.14\% \\ 1.37\% & 0.11\% & 0.5\% \\ 0.30\% & 0.17\% & 0.23\% \end{bmatrix} \quad (48)$$

To simulate the presence of white Gaussian measurement noise, random numbers were added to the training data. Five different levels of noise corresponding to a 5dB, 10dB, 15dB, 20dB and 30dB signal to noise ratio (SNR) were induced. The system was trained, validated and tested using the LM algorithm, and regression analysis was carried out. The coefficient of correlation from regression analysis for all different levels of SNR is plotted in Fig. 23 where it can be observed that higher SNR corresponds to higher coefficient of regression R and vice versa. The ideal value for R is 1.0.

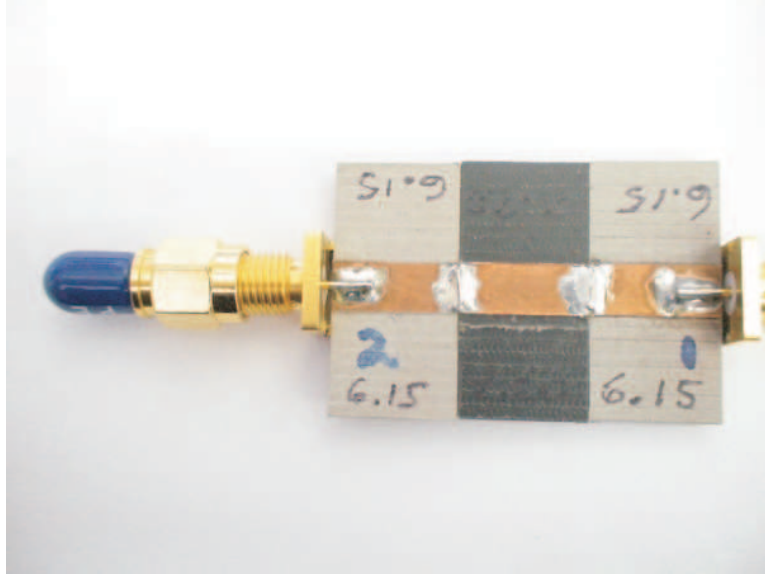


Figure 24: Snapshot of microstrip transmission line setup for experimental measurements.

4.4 *Experimental Measurement and Analysis*

To enable measurements, a device was fabricated with three microstrip transmission lines cascaded together in the fashion described in section III, as shown in Fig. 14 and Fig. 24. The dimensions and dielectric properties of the cascaded microstrip lines are tabulated in Table 4. Materials with parameter values of $\epsilon_{r1} = \epsilon_{r3} = 6.15$ and $\epsilon_{r2} = 2.2$ were used. The microstrip line was terminated in a 50Ω load.

Table 4: Dimensions of microstrip transmission lines in experimental setup.

	Trnas Line 1	Trans Line 2	Trans Line 3
Length (L)	1.25 cm	1.25 cm	1.25 cm
Width (W)	0.5 cm	0.5 cm	0.5 cm
Substrate Height	0.127 cm	0.157 cm	0.127 cm
Conductor Thickness	0.0017 cm	0.0017 cm	0.0017 cm
Loss Tangent	0.002	0.0009	0.002
Substrate	RO 3006	RT/Duroid 5880	RO 3006
Dielectric Constant	6.15	2.2	6.15

A network analyzer was used to record S-parameters over the frequency range 1-5 GHz. Comparisons between measured and simulated values of the magnitude

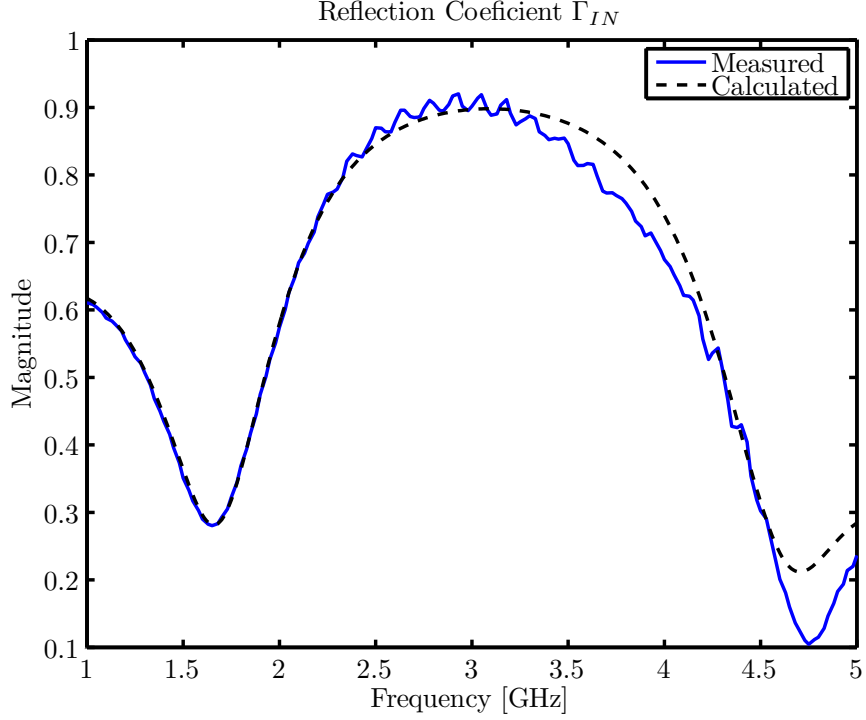


Figure 25: Comparison between magnitude of measured and calculated reflection coefficient ($|\Gamma_{in}|$).

and phase of the reflection coefficient are shown in Figs. 25 and 26. There is excellent agreement between measured and simulated results in the frequency range 1-2.5 GHz, and reasonable agreement at higher frequencies. Ripples and other deviations are observed for higher frequencies, which can be attributed at least in part to discontinuities introduced by the fabrication technique. The microstrip lines were soldered together horizontally, across the width, which caused a noticeable amount of solder paste to sit on the joints. Moreover, a thin wire was also inserted horizontally to strengthen the solder.

For training purposes, simulated data were generated for ϵ_{r1} and ϵ_{r3} swept across the range from 5 - 8, and for ϵ_{r2} from 1.1 - 3.6. This results in a dataset with $30 \times 25 \times 30 = 22,500$ vectors. The row dimension of the data matrix is determined by frequency range and frequency step size. The methodology was tested using the 1-5 GHz frequency range, with a frequency step size of 300 MHz. Using 20 neurons

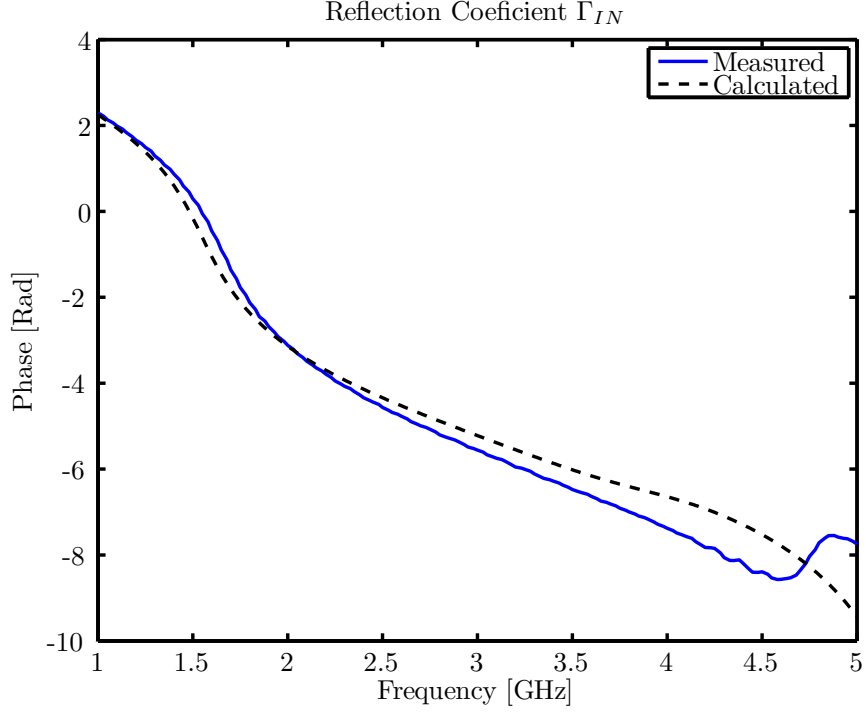


Figure 26: Comparison between measured and calculated phase of reflection coefficient ($\angle\Gamma_{in}$).

with the LM algorithm, a neural network was trained with simulated data containing white Gaussian noise. In terms of absolute error, the coefficient of regression R was determined to be 0.91, 0.95, 0.95 and 0.99 for an SNR of 5, 10, 20 and 30 dB, respectively. Table 5 shows the estimated values of dielectric constants and their absolute error levels. In this case, the best errors are achieved for a neural network trained with a data set containing white Gaussian noise with an SNR of 10dB. To verify the optimum number of neurons in the hidden layer, the same procedure was repeated for 25 neurons, and similar results were obtained for the coefficient of regression as a function of the SNR level. To avoid over fitting and to minimize the computation effort, it is desired to keep the number of neurons in the hidden layer as small as possible without compromising the accuracy of results. In this case 20 neurons is sufficient for an accurate approximation using a frequency range from 1-5GHz with a step size of 300 MHz.

Table 5: Comparison of actual values of $\epsilon_{r1,2,3}$ with the neural network results obtained with 1 layer of 20 neurons and trained on data having different levels of white noise, over the frequency range from 1-5 GHz.

	'R'	ϵ_{r1}	ϵ_{r2}	ϵ_{r3}	Average Error
Actual Value		6.15	2.2	6.15	
Estimated with AWGN (30dB SNR)	0.99	5.96	2.56	7.23	
Absolute Error		0.19	0.36	1.08	0.54
Estimated with AWGN (20dB SNR)	0.952	5.91	2.96	6.58	
Absolute Error		0.24	0.76	0.43	0.48
Estimated with AWGN (10dB SNR)	0.956	5.95	2.75	6.20	
Absolute Error		0.20	0.55	0.05	0.27
Estimated with AWGN (05dB SNR)	0.91	6.45	2.75	6.04	
AbsoluteError		0.30	0.55	0.11	0.32

For experimental verification, the training data were generated for the frequency range from 1-2.5 GHz. A neural network containing a single hidden layer of 20 neurons was trained with data containing white Gaussian noise (10dB SNR). To eliminate the element of coincidence, and verify the robustness of algorithm, the neural network was trained and tested three times on the same data, with different starting weights each time. The three sets of results are tabulated in Table 6.

Table 6: The actual values of $\epsilon_{r1,2,3}$ compared to the values estimated using neural networks for the frequency range 1-2.5 GHz.

	Trans Line 1	Trans Line 2	Trans Line 3	Average Error
	ϵ_{r1}	ϵ_{r2}	ϵ_{r3}	$(\epsilon_{rn} - \epsilon_{rne})$
Target Value (ϵ_{rn})	6.15	2.20	6.15	
Estimate 1 (ϵ_{rne})	5.72	2.73	5.60	
Error ($\epsilon_{rn} - \epsilon_{rne}$)	0.43	0.53	0.55	0.50
% Error	6.9%	24%	8.9%	13.2%
Estimate 2 (ϵ_{rne})	5.72	2.89	5.53	
Error ($\epsilon_{rn} - \epsilon_{rne}$)	0.43	0.69	0.62	0.58
% Error	6.9%	31%	10.1%	15.9%
Estimate 3 (ϵ_{rne})	5.67	2.81	5.69	
Error ($\epsilon_{rn} - \epsilon_{rne}$)	0.48	0.61	0.46	0.51
% Error	7.8%	27.7%	7.47%	14.3%

These results exhibit an average absolute error range of ± 0.6 and a coefficient of regression R greater than 0.92. The % error in the center bin (Trans Line 2) is

comparatively higher as compared to the % error in the estimated permittivities of transmission lines 1 and 3. However, the absolute error in the estimated relative dielectric constant of each section of the transmission line remains around ± 0.6 . The increased % error in the center bin is a consequence of the lower value of ϵ_{r2} in comparison to the others.

4.5 Discussion

For RFID-like REMS sensor, neural networks can be used to extract material parameter values from complex reflection coefficient data of a lossless electro-material line. The dielectric constant was varied across each of three lengths of microstrip transmission lines. With a priori knowledge of geometry of the structure and the range of varying dielectric constants, the neural network was trained with data for the magnitude and phase of Γ_{in} across the complete frequency range of interest. The frequency resolution was an important parameter for accuracy of results and computational efficiency. It was demonstrated that a frequency step size smaller than 100 MHz does not improve the accuracy of results. Furthermore, for a wide range of frequencies from 1-5 GHz, a frequency resolution of 300MHz is sufficiently dense to keep the results accurate while maintaining the computational efficiency of the algorithm. The Levenberg Marquardt backpropagation algorithm was determined to be well-suited to solve this one dimensional inverse scattering type problem using neural networks. White Gaussian noise with a 10dB SNR was induced in training data to simulate the measurement noise. The architecture of the neural network is an important parameter for any problem, and it was demonstrated that one hidden layer of 20 or 25 neurons enables optimum performance of the network in terms of average absolute error and computational efficiency. With the application of a neural network based on the LM backpropagation algorithm with one hidden layer of 20

neurons, the dielectric constant of a three cascaded microstrip transmission line system was estimated with absolute average error less than ± 0.5 . We note that this one dimensional inverse scattering problem would be more challenging to investigate with non deterministic boundaries and for material properties that vary across a greater range.

CHAPTER V

THERMO-RESPONSIVENESS AT MICROWAVE FREQUENCIES

The concept of REMS based sensor can be applied to a wide variety of applications. For example a thermotropic material can be used in the material line that records the time profile of temperature changes in the spatially distributed electrical properties. Similarly, piezoelectric materials or dielectric elastomers can be used where the target parameter to be sensed is related to stress or strain, respectively. To better understand the thermo-responsive nature of materials at microwave frequencies, a nematic liquid crystal *4-Cyano-4 Pentylbiphenyl*, commonly known as *5CB*, and isopropyl alcohol were studied using a monopole probe. *5CB* is a nematic liquid crystal which undergoes a phase transition from a crystalline state to a nematic state at 18°C and it goes from a nematic to an isotropic state at 35°C . The linear and non-linear dielectric measurements of *5CB* for the frequency range from 100kHz to 100MHz, demonstrating the effect of temperature on permittivity at lower frequencies, are reported in [46].

5.1 Variations in ϵ_r with Temperature Changes

5.1.1 Preliminary Experimental Observations

To observe the thermo-responsive nature of the liquid crystal *5CB* at microwave frequencies, a 10mm long monopole probe was immersed in *5CB*, and S11 measurements were recorded using a vector network analyzer (VNA) for temperatures varying from 19.8°C to 25.7°C . The measurement setup is shown in Fig. 27. Using the VNA, S11 was recorded over the frequency range from 2-5 GHz. The results are shown in Fig. 28. A noticeable change is observed in S11 measurements recorded for the

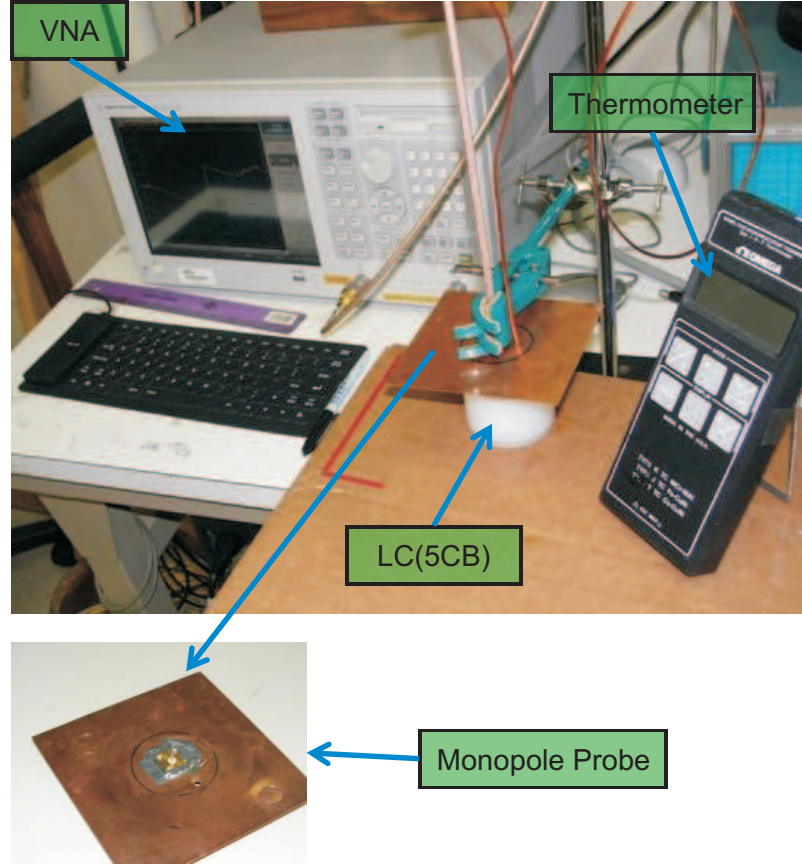


Figure 27: Measurement setup to measure S_{11} at different temperatures for a 10mm monopole probe immersed in Liquid Crystal 5CB

frequency range from 2 - 5 GHz, as the temperature is varied from 19.8°C to 25.7°C , suggesting the possibility of sensing temperature variations as small as approximately 2°C .

Similar thermotropic behavior was observed for isopropyl alcohol when temperature was varied from 9.7°C to 36.9°C using the measurement setup shown in Fig. 29. S_{11} measurement of a monopole probe immersed in isopropyl alcohol are shown in Fig. 30. Significant variations are observed in S_{11} with changes in temperature, which describes the changes in permittivity with change in temperature.

These experiments verify the thermotropic behavior of the liquid crystal 5CB and isopropyl alcohol at microwave frequencies. It can also be observed that it is not

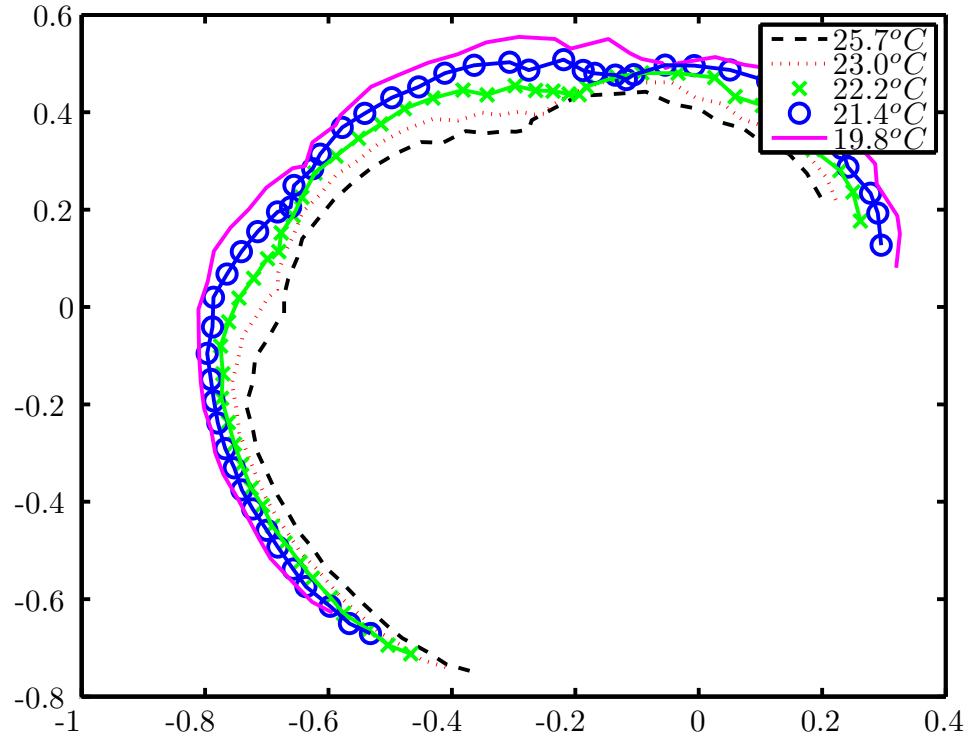


Figure 28: Measured S_{11} (complex-valued quantity displayed as a polar plot) for a 10mm monopole probe immersed in the liquid crystal 5CB

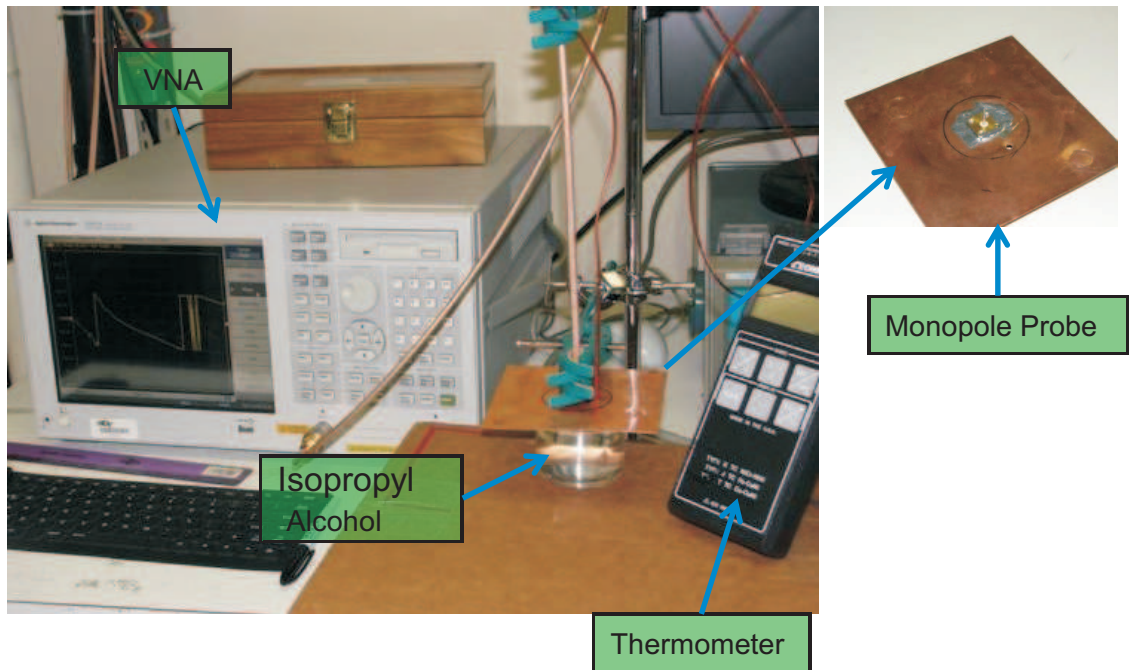


Figure 29: Measurement setup to measure S_{11} at different temperatures for a 10mm monopole probe immersed in isopropyl Alcohol

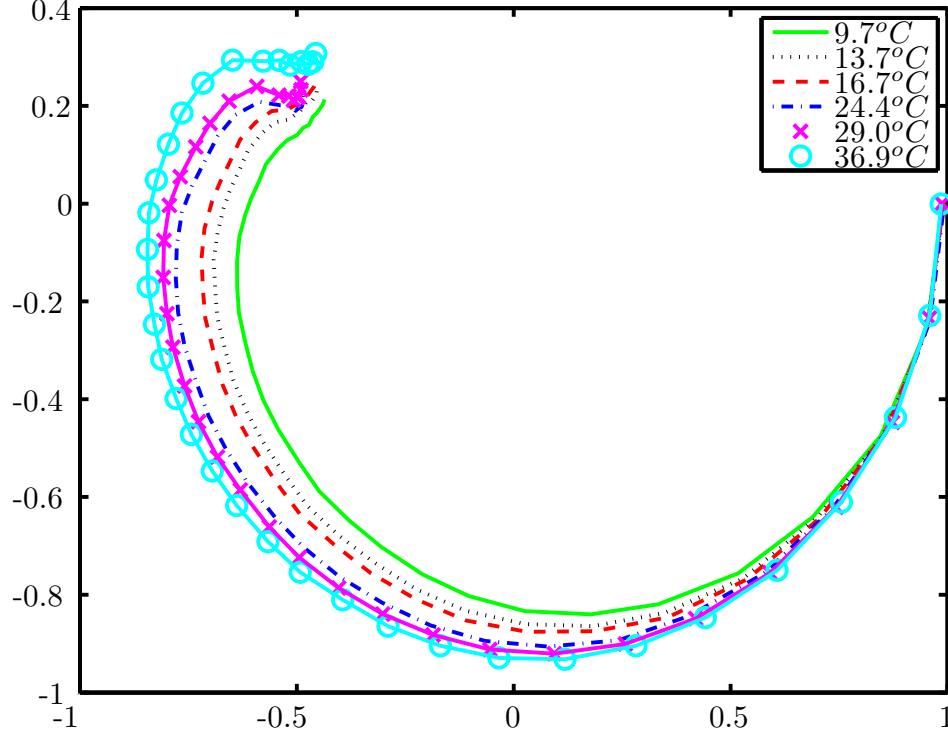


Figure 30: Measured S11(complex-valued quantity displayed as a polar plot) for a 10mm monopole probe immersed in isopropyl Alcohol

only the real part of ϵ_r which varies with temperature, but the imaginary part ϵ_r'' also displays temperature dependence.

5.2 *Experimental Verification of Thermo-responsiveness of LC 5CB and Isopropyl Alcohol*

For additional experimental verification of the thermo-responsive nature of LC 5CB and isopropyl alcohol, an Agilent 85070D Dielectric Probe Kit was used to conduct permittivity measurements. The dielectric probe kit measures ϵ_r' , ϵ_r'' , or $\tan \delta$ over a broad range of frequencies, 200MHz to 20GHz. The main component of the kit is the high-temperature dielectric probe, as shown in Fig. 31, which when immersed into the material under test (MUT), can measure complex permittivity for temperatures ranging from -40°C to $+200^\circ\text{C}$ [47].

The typical accuracy of the system is $\pm 5\%$ for ϵ_r' , and ± 0.05 for $\tan \delta$, as shown

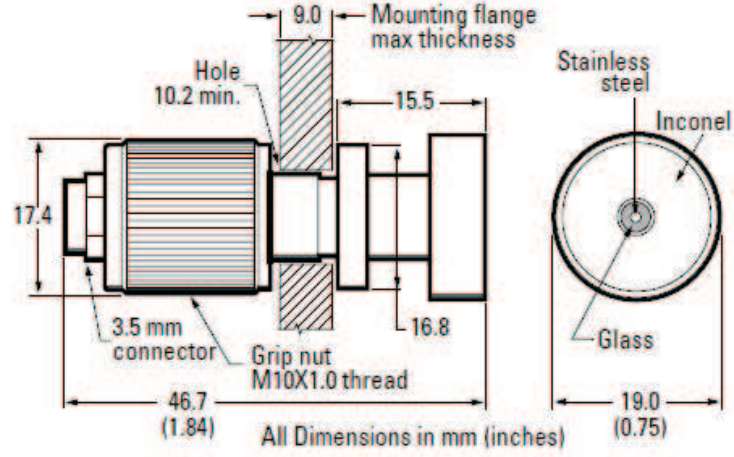


Figure 31: High-temperature dielectric probe of the Agilent 85070D Dielectric Probe Kit (From product overview).

versus frequency in Fig. 32 [47]. It is worth noticing that an increased error is observed for lower frequencies and for lower values of ϵ'_r . The accuracy of the probe kit is much worse than the typical values of accuracy in the frequency range of our interest, 3 - 6 GHz. For the LC 5CB, the error in ϵ'_r and $\tan \delta$ can be even larger than 20% and 0.20, respectively, especially for the lower frequencies.

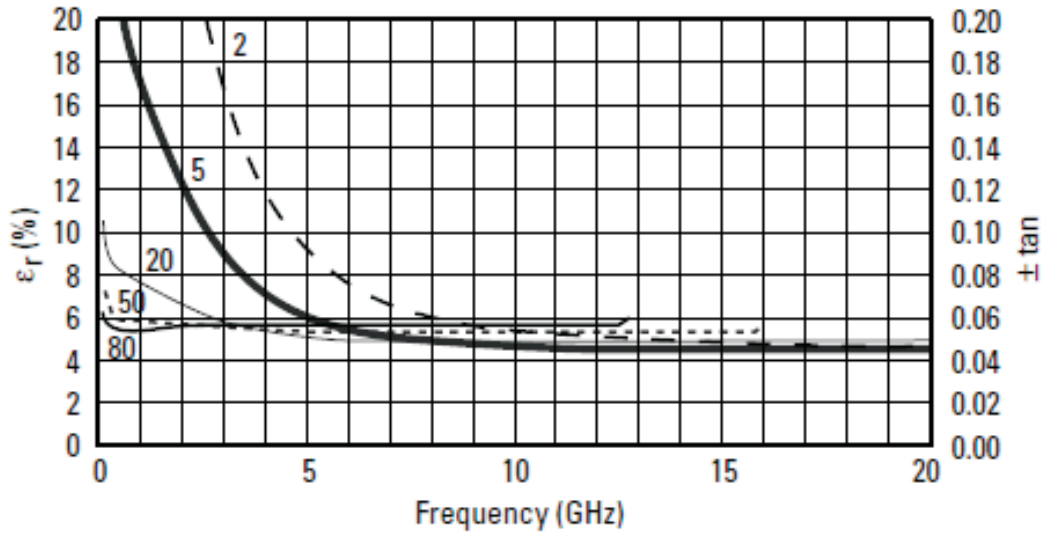


Figure 32: Dielectric probe kit accuracy vs frequency for $\epsilon'_r = 2, 5, 20, 50$ and 80 . (From product overview).

5.2.1 Measurement Setup

To measure the thermo-responsiveness in terms of ϵ'_r and $\tan \delta$, the MUT (LC 5CB or isopropyl alcohol) was placed in a small glass container positioned inside a temperature controlled oven or refrigerator. The dielectric probe was immersed in the MUT and connected to the VNA as shown in Fig. 33. The VNA was interfaced with the computer through a general purpose interface bus (GPIB) to record ϵ'_r and $\tan \delta$ for the selected temperature and frequency range.

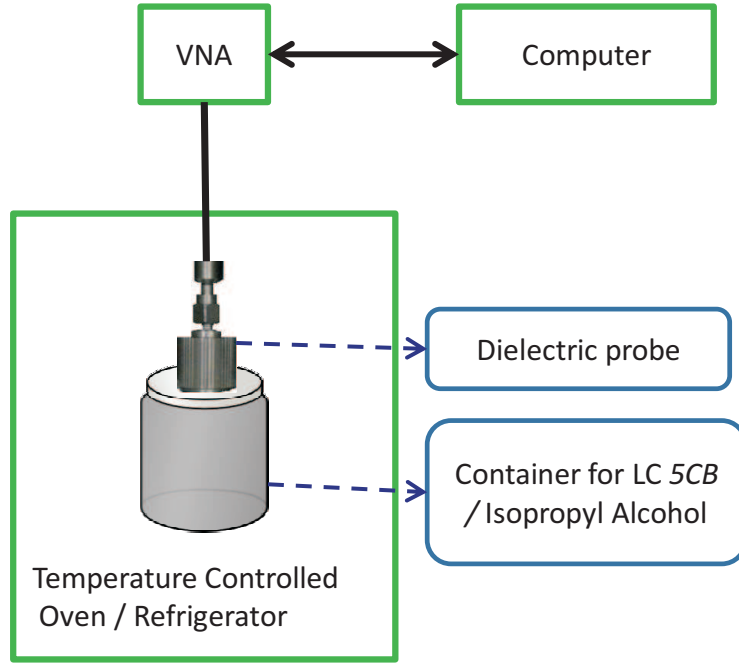


Figure 33: Measurement setup to measure S11 at different temperatures using the Agilent dielectric probe immersed in isopropyl alcohol

For experimental verification, a series of measurements were recorded for LC 5CB and isopropyl alcohol at different temperature settings ranging from approximately 10°C to 50°C . For recording the complex permittivity at temperatures higher than the room temperature, the small glass container (80mL) filled with MUT was placed inside a temperature controlled oven. The temperature in the oven is controlled by a temperature control unit coupled with a temperature probe. The dielectric probe

is immersed in the MUT and connected to the VNA, which is interfaced with a computer through a GPIB. The complete measurement setup is shown in Fig. 34. The temperature probe, MUT and the dielectric probe are visible in the part showing the ‘inside view’ of the oven.

For temperatures lower than the room temperature, the MUT was placed inside a refrigerator and the temperature was recorded using the temperature probe.

5.2.2 Variations in ϵ'_r and $\tan \delta$ of LC 5CB with temperature

For the ϵ'_r and $\tan \delta$ measurements, the liquid crystal 5CB was placed in the container inside the temperature controlled oven as shown in Fig. 34. The Agilent 85070d dielectric probe kit was calibrated before the measurement campaign. For every measurement, after the temperature controlled oven / refrigerator has reached the desired temperature, the MUT was allowed to settle at that particular temperature for approximately one hour. For the liquid crystal 5CB, a considerable change in permittivity was observed as the temperature was varied from $5^\circ C$ to $40^\circ C$. As the temperature is varied, the response in terms of ϵ'_r and $\tan \delta$ can be divided into three segments: $5^\circ C$ to $9^\circ C$, $22^\circ C$ to $26^\circ C$, and $27^\circ C$ to $40^\circ C$. The variations in ϵ'_r and $\tan \delta$ for $5^\circ C$ to $9^\circ C$ over the frequency range from 3.5 - 6 GHz are shown in Fig. 35 and Fig. 36, respectively.

As the temperature is increased from $22^\circ C$ to $23^\circ C$, a large variation is observed in ϵ'_r and $\tan \delta$ as shown in Fig. 37 and Fig. 38, respectively.

As the temperature is further increased from $23^\circ C$ to $26^\circ C$, smaller variations are observed in ϵ'_r and $\tan \delta$ as shown in Fig. 39 and Fig. 40, respectively.

In the last segment, the variations in ϵ'_r and $\tan \delta$ are recorded as the temperature is varied from $27^\circ C$ to $40^\circ C$ as shown in Fig. 41 and Fig. 42, respectively.

It can be observed that for all temperature ranges the value of ϵ'_r first decreases as the frequency is increased from 3.5 GHz to 5 GHz, and then it starts to increase

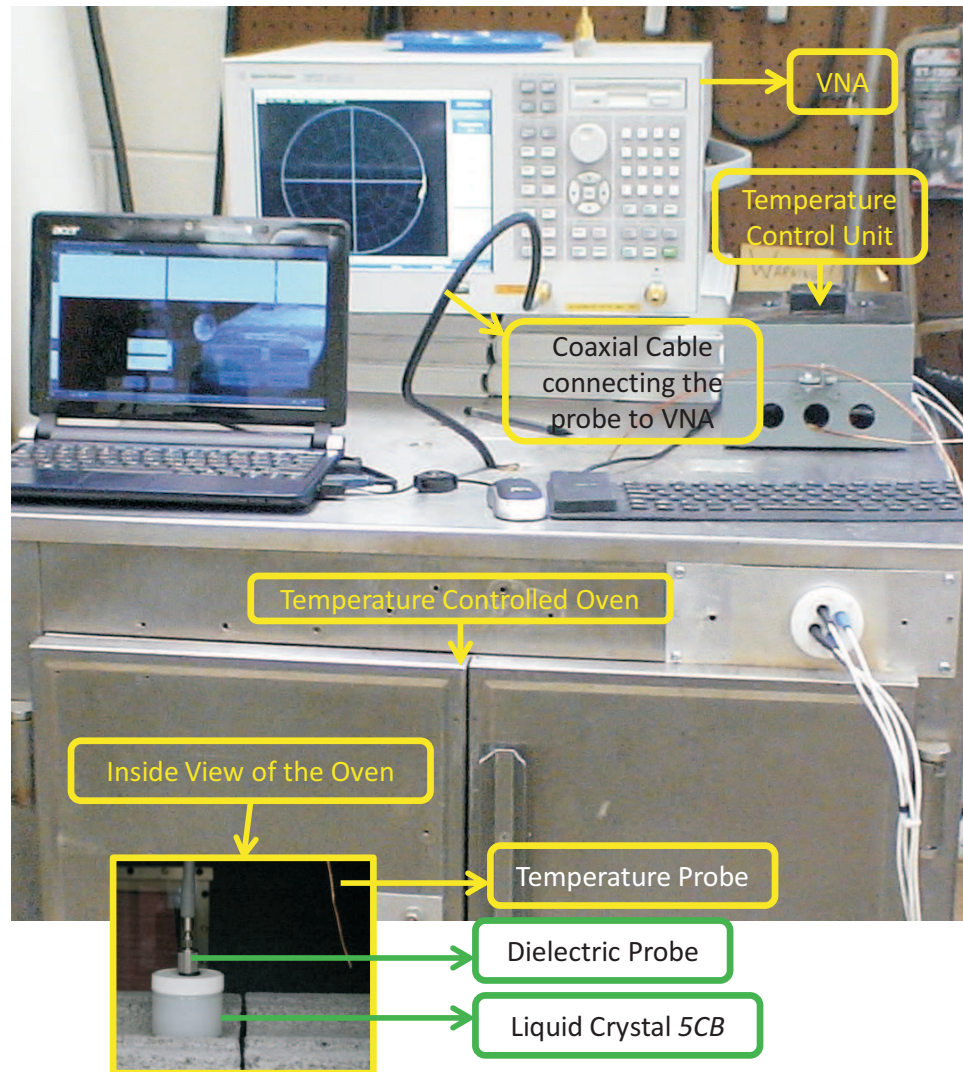


Figure 34: Measurement setup to measure S_{11} at different temperatures using the Agilent dielectric probe immersed in isopropyl alcohol

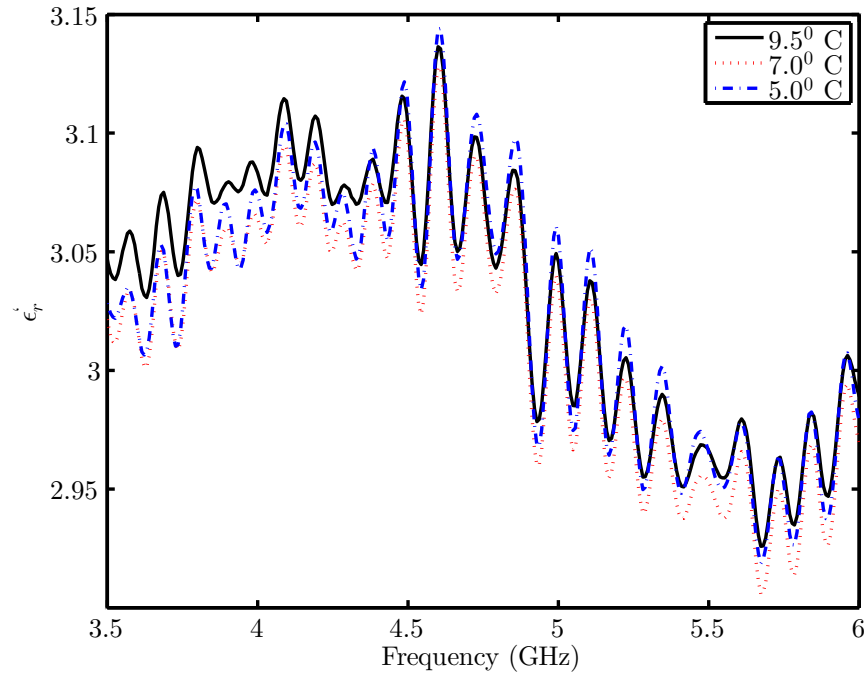


Figure 35: Variations in ϵ'_r of LC 5CB as the temperature is varied from 5°C to 9°C over the frequency range from 3.5 GHz to 6 GHz.

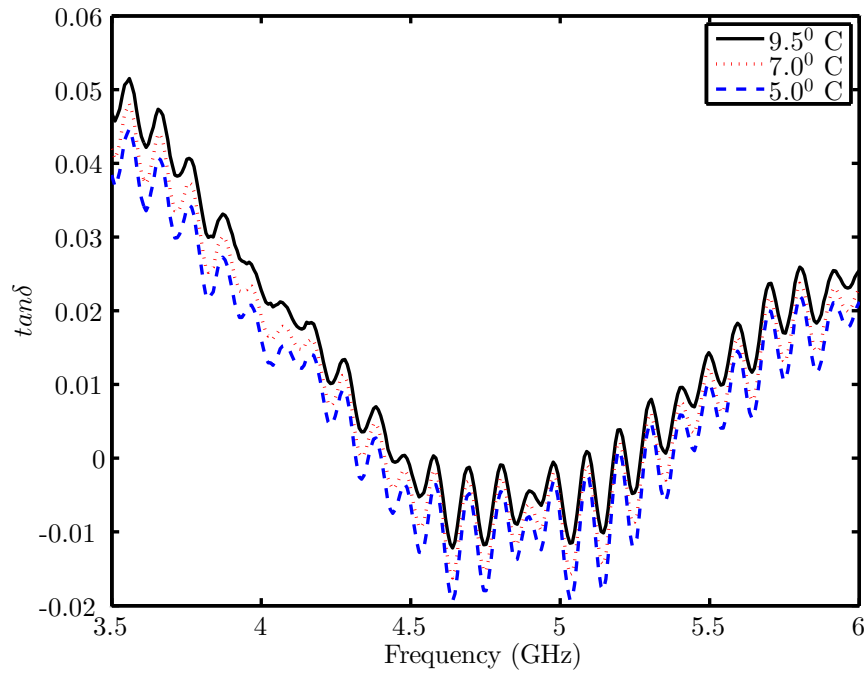


Figure 36: Variations in $\tan \delta$ of LC 5CB as the temperature is varied from 5°C to 9°C over the frequency range from 3.5 GHz to 6 GHz.

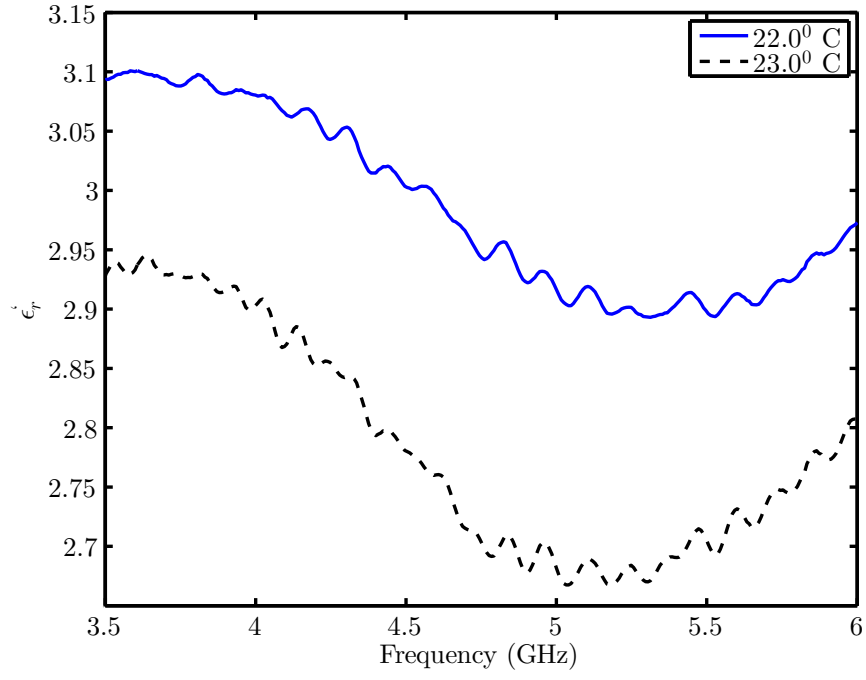


Figure 37: Variations in ϵ'_r of LC 5CB as the temperature is increased from 22°C to 23°C over the frequency range from 3.5 GHz to 6 GHz.

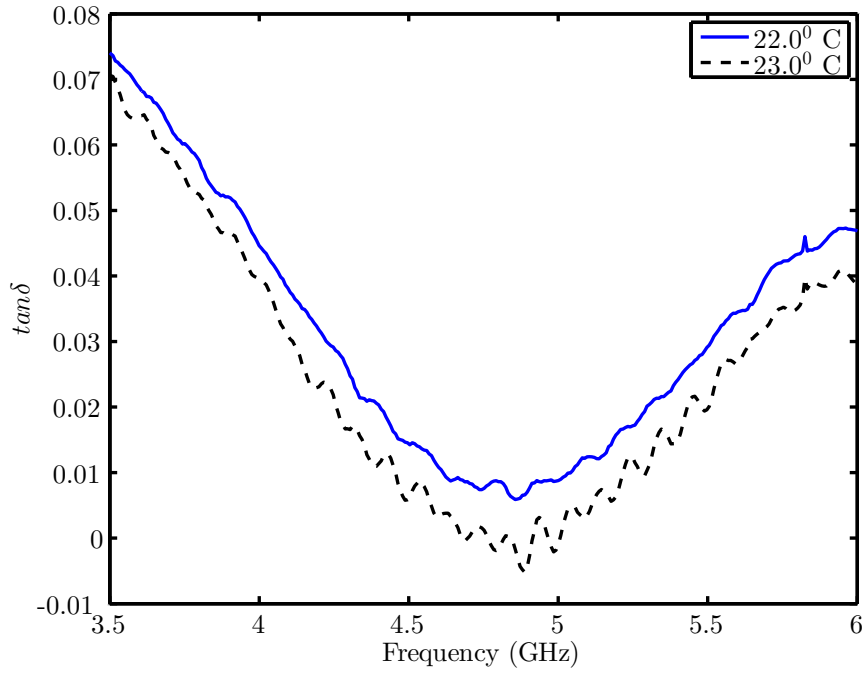


Figure 38: Variations in $\tan \delta$ of LC 5CB as the temperature is increased from 22°C to 23°C over the frequency range from 3.5 GHz to 6 GHz.

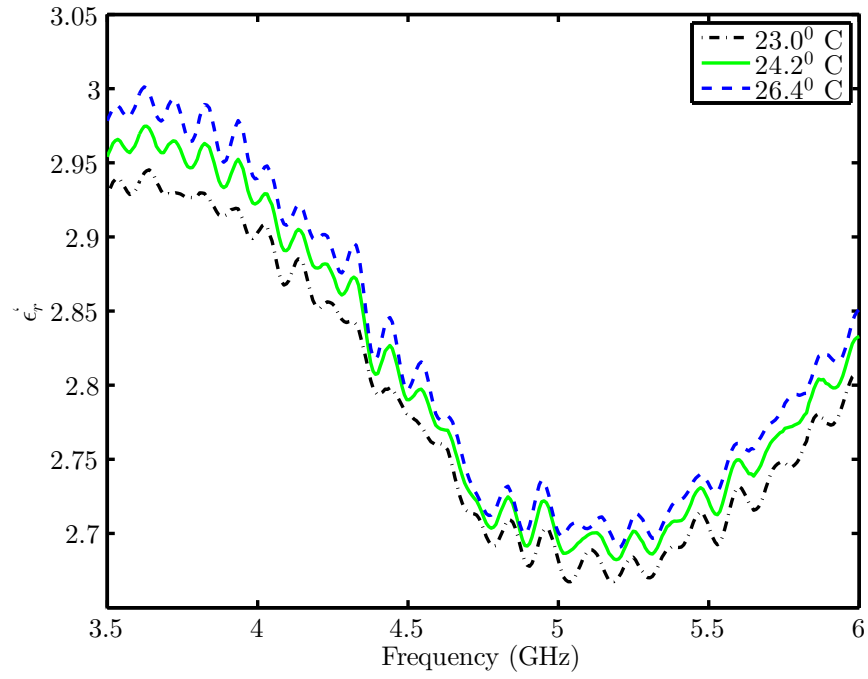


Figure 39: Variations in ϵ'_r of LC 5CB as the temperature is increased from 23°C to 26°C over the frequency range from 3.5 GHz to 6 GHz.

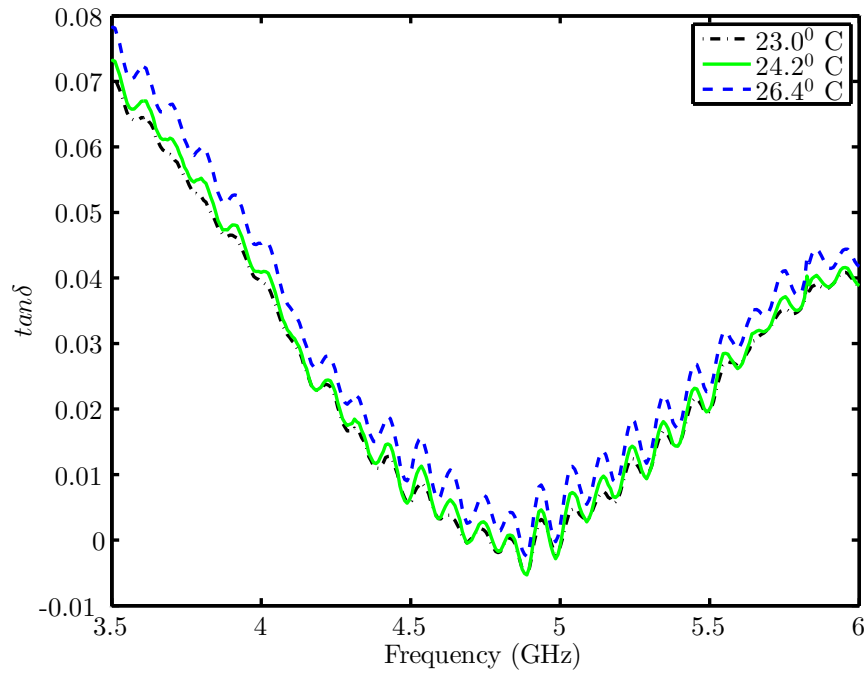


Figure 40: Variations in $\tan \delta$ of LC 5CB as the temperature is increased from 23°C to 26°C over the frequency range from 3.5 GHz to 6 GHz.

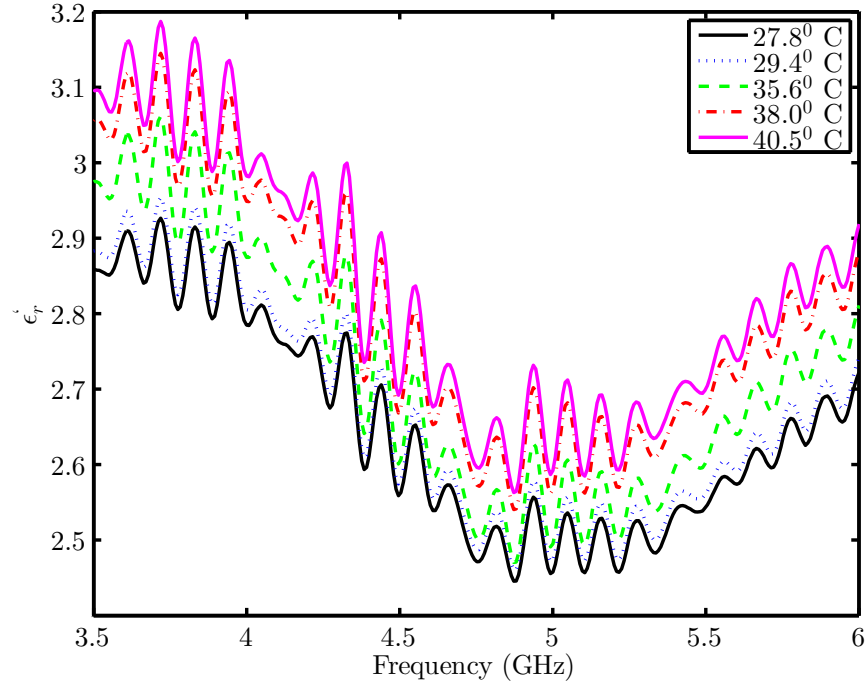


Figure 41: Variations in ϵ'_r of LC 5CB as the temperature is increased from 27°C to 40°C over the frequency range from 3.5 GHz to 6 GHz.

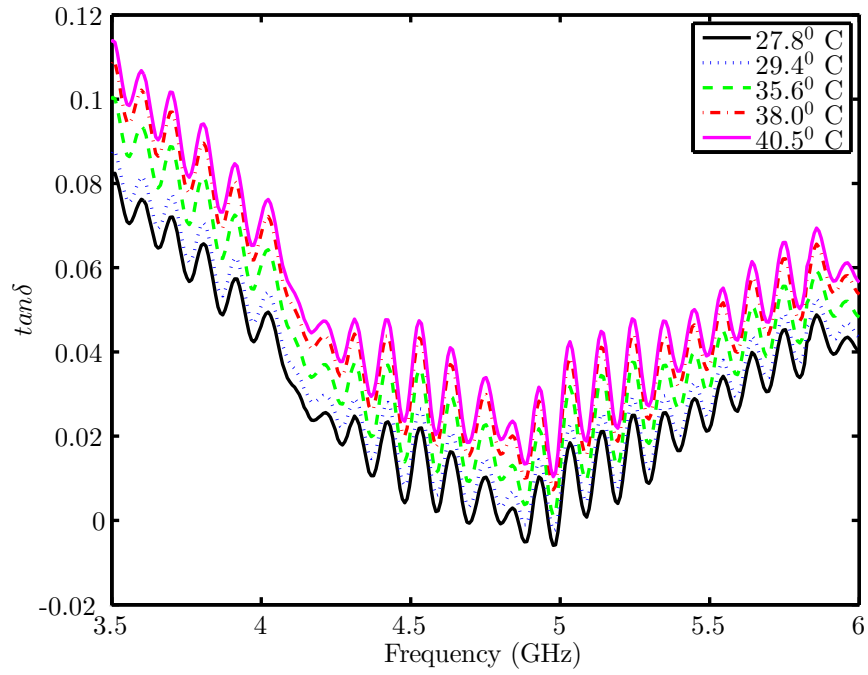


Figure 42: Variations in $\tan \delta$ of LC 5CB as the temperature is increased from 27°C to 40°C over the frequency range from 3.5 GHz to 6 GHz.

as the frequency is further increased from 5 GHz to 6 GHz. The response indicates the nonlinear response of liquid crystal in terms of electrical properties. It is also observed that ϵ_r' varies from a maximum value of approximately 3.2 to the lowest value of 2.4 over the given frequency range as the temperature varies from $5^\circ C$ to $40^\circ C$. However, the change is not uniform across the complete range of temperatures. For values ranging from $5^\circ C$ to $9^\circ C$, the response has noticeable oscillations, with slight change with temperature. A significant change in ϵ_r' is observed as the temperature is increased from $22^\circ C$ to $23^\circ C$, and then as the temperature is increased further from $23^\circ C$ to $26^\circ C$, the magnitude of change decreases. The response in terms of ϵ_r' is least oscillatory in the temperature range from $23^\circ C$ to $26^\circ C$. For the values of temperature ranging from $27^\circ C$ to $40^\circ C$, there is a noticeable change in the permittivity values with the change in temperature, but at the same time there are considerable oscillations in ϵ_r' values as the frequency is swept from 3.5 - 6 GHz.

The response to changes in temperature in terms of $\tan \delta$ for LC 5CB is similar to the ϵ_r' response in terms of shape, oscillations and variations with temperature, except that the variations span a smaller range of values. Also for the frequency range 4.75 GHz to 5.1 GHz, the value of $\tan \delta$ reaches almost zero and even goes negative at a few points. The liquid crystal 5CB has not been characterized at microwave frequencies, to the best of our knowledge, and therefore the reasons for oscillatory response in ϵ_r' of LC 5CB, and the negative values of $\tan \delta$ are not obvious. However, the possible reasons can be attributed to the internal reflections of the dielectric probe, the reflections from the glass container in which MUT was placed, and the phase transitions of LC 5CB from crystalline to nematic to isotropic. Moreover the dielectric probe kit is also not as accurate for the lower frequencies (less than 6 GHz) and for the lower values of ϵ_r' and $\tan \delta$ as shown in Fig. 32 [47].

The internal reflections of the dielectric probe and the glass container can be addressed by making similar measurements for water, which has been well characterized

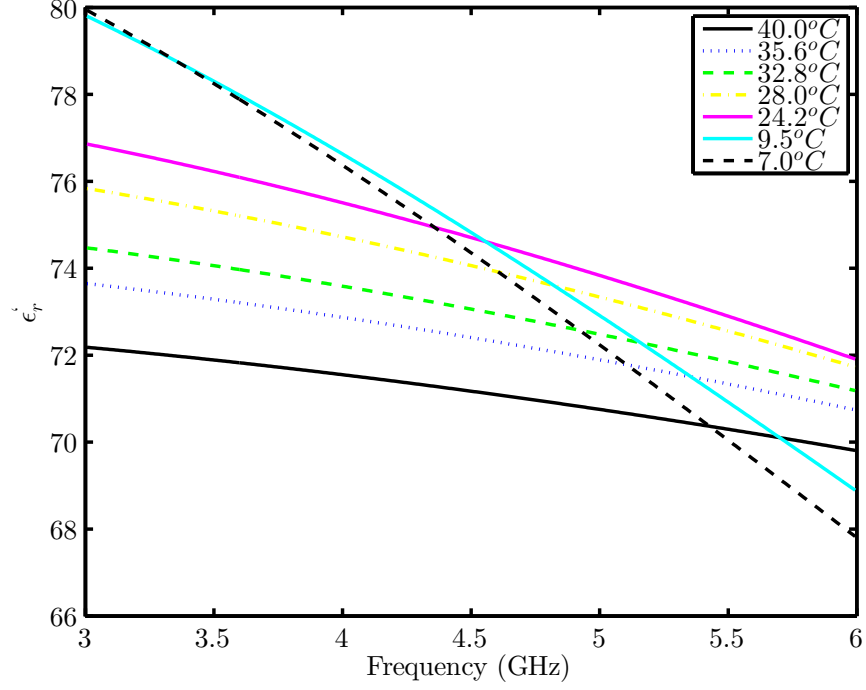


Figure 43: ϵ'_r for water computed using Miessner and Wentz model for the frequency range from 3-6 GHz

by other researchers. Specifically, we will use the Meissner and Wentz model for the complex permittivity of ionized water to recalibrate the measurements. The method will involve computing the ϵ'_r and $\tan \delta$ for different temperatures using the model for complex permittivity of pure water as reported in [48]. The computed values for ϵ'_r and $\tan \delta$ of water for different temperatures of interest are shown in Fig. 43 and Fig. 44, respectively.

In the next step, ϵ'_r and $\tan \delta$ are measured for water for the temperatures of interest over the frequency range from 3 - 6 GHz, using the dielectric probe setup described in Fig. 34. For each temperature value, the difference between the computed and measured values of ϵ'_r and $\tan \delta$ will provide a correction factor. This correction factor, once added to the measured values of ϵ'_r and $\tan \delta$ for given temperatures, will compensate for any internal reflections of the dielectric probe and the glass container holding the MUT. This process was adopted from the work performed by Danny

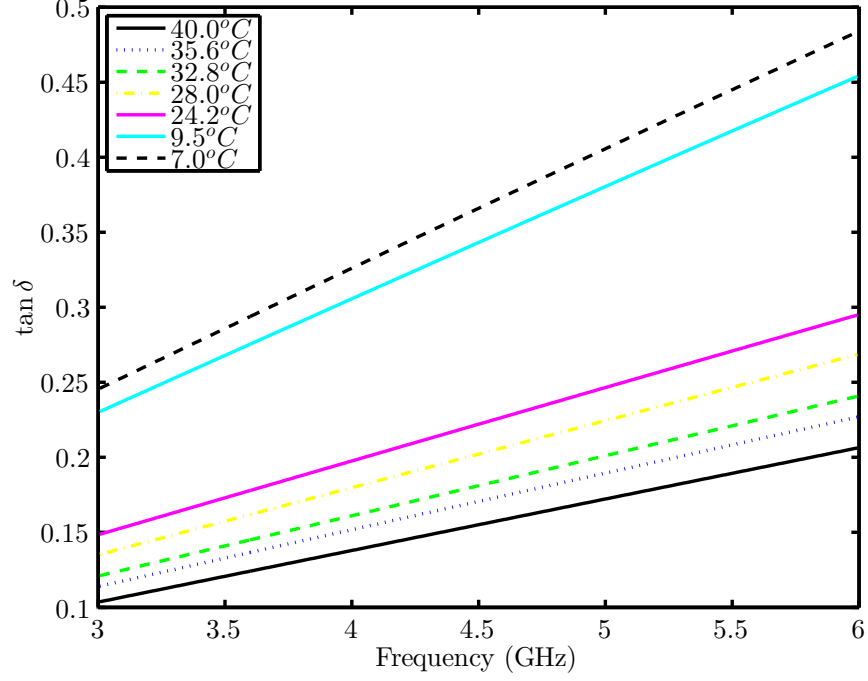


Figure 44: $\tan \delta$ for water computed using Miessner and Wentz model for the frequency range from 3-6 GHz

Duong in measuring the complex permittivity of ammonia gas [49]. Using the correction method, the resultant ϵ'_r and $\tan \delta$ for LC 5CB are shown in Fig. 45 and Fig. 46, respectively.

The results are significantly improved using the aforesaid correction method. The oscillations are considerably flattened and the response with temperature shows a more consistent behavior over the complete frequency range, i.e. same pattern over the complete frequency range with a shift with changes in temperature. It can be observed that the ϵ'_r increases as the temperature is increased from 26.6°C to 38.0°C . A similar behavior in reverse direction is observed for $\tan \delta$: it decreases as the temperature is increased from 26.6°C to 38.0°C . In case of $\tan \delta$, however, still some values are touching the negative region at the lower frequencies, which may be attributed to the sources of error cited earlier.

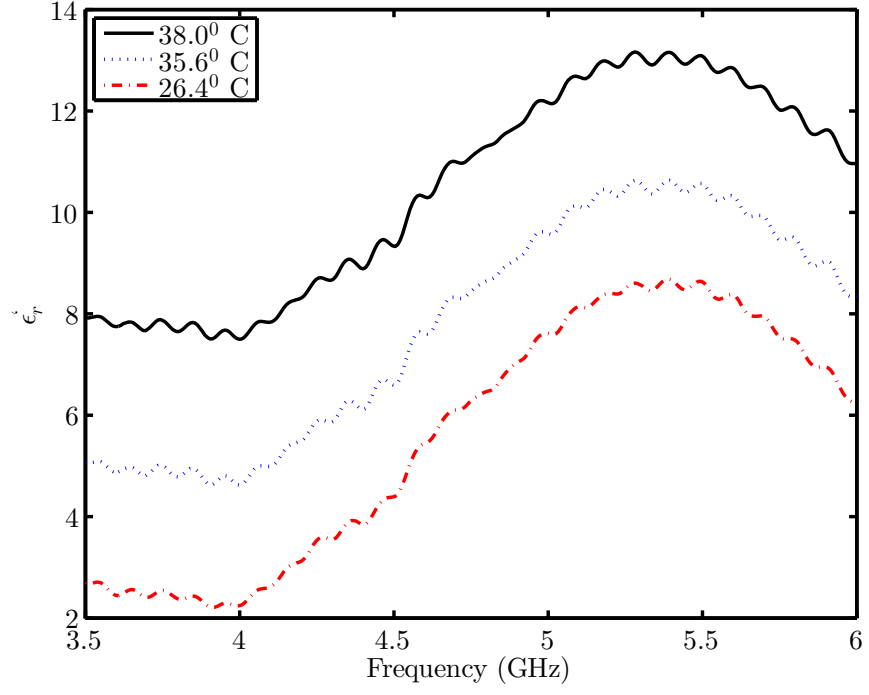


Figure 45: ϵ'_r of LC 5CB for different temperatures over the frequency range from 3.5 GHz to 6 GHz, after using the Meissner & Wentz model correction.

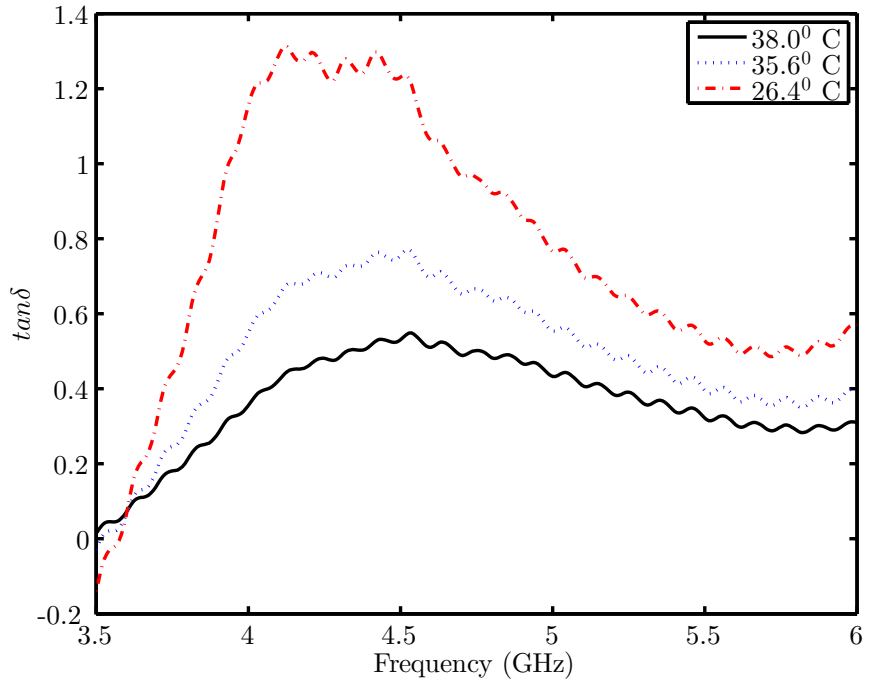


Figure 46: $\tan \delta$ of LC 5CB for different temperatures over the frequency range from 3.5 GHz to 6 GHz, after using the Meissner & Wentz model correction.

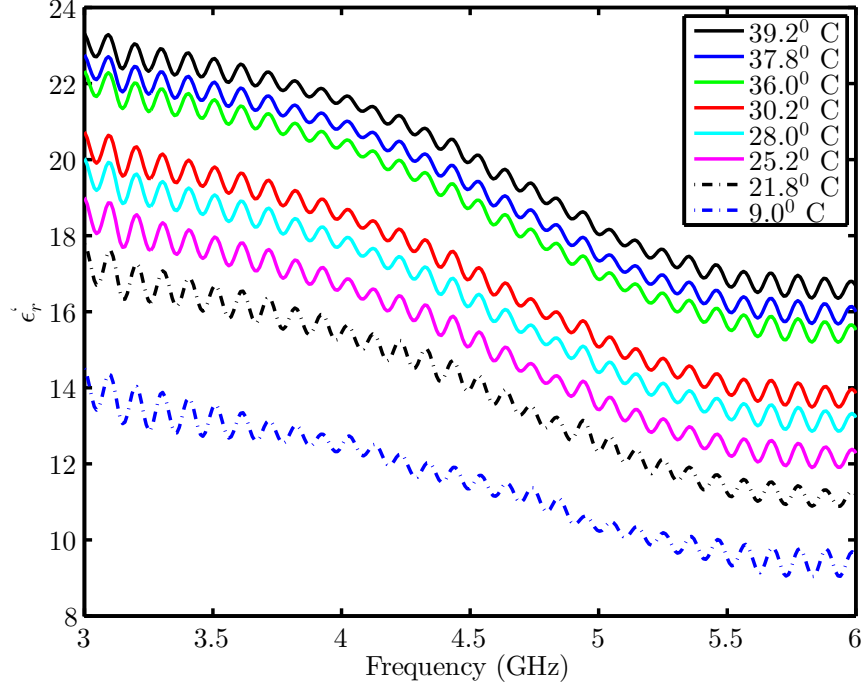


Figure 47: Variations in ϵ'_r of Isopropyl alcohol as the temperature is varied from 9°C to 40°C over the frequency range from 3 - 6 GHz.

5.2.3 Variations in ϵ'_r and $\tan \delta$ of Isopropyl Alcohol with temperature

Variations in the complex permittivity of isopropyl alcohol due to temperature changes at microwave frequencies were recorded using a similar experimental setup, as shown in Fig. 34. The response to changes in temperature in terms of ϵ'_r and $\tan \delta$ is shown in Fig. 47 and Fig. 48, respectively.

It is observed that as the temperature increases, ϵ'_r increases and $\tan \delta$ decreases. Moreover, ϵ'_r decreases and $\tan \delta$ increases with the increase in frequency. There are noticeable oscillations in both the ϵ'_r and $\tan \delta$ over the complete frequency range of interest. The measured data are recalibrated using the correction obtained from the Meissner & Wentz model for complex permittivity of water [48]. The resultant ϵ'_r and $\tan \delta$, corrected for any internal reflections of the dielectric probe, or the container, are shown in Fig. 49 and Fig. 50, respectively.

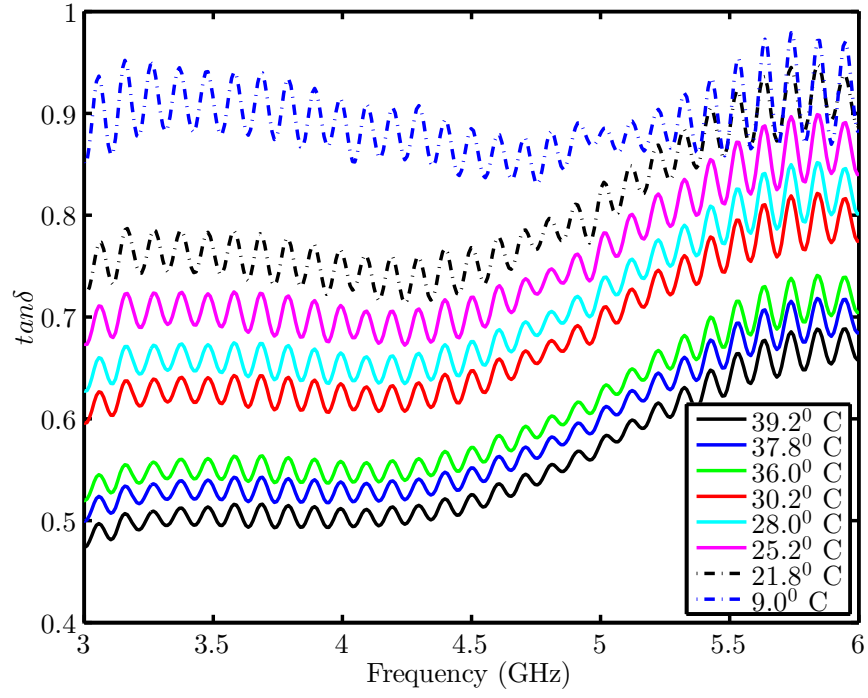


Figure 48: Variations in $\tan \delta$ of Isopropyl alcohol as the temperature is varied from 9°C to 40°C over the frequency range from 3 - 6 GHz.

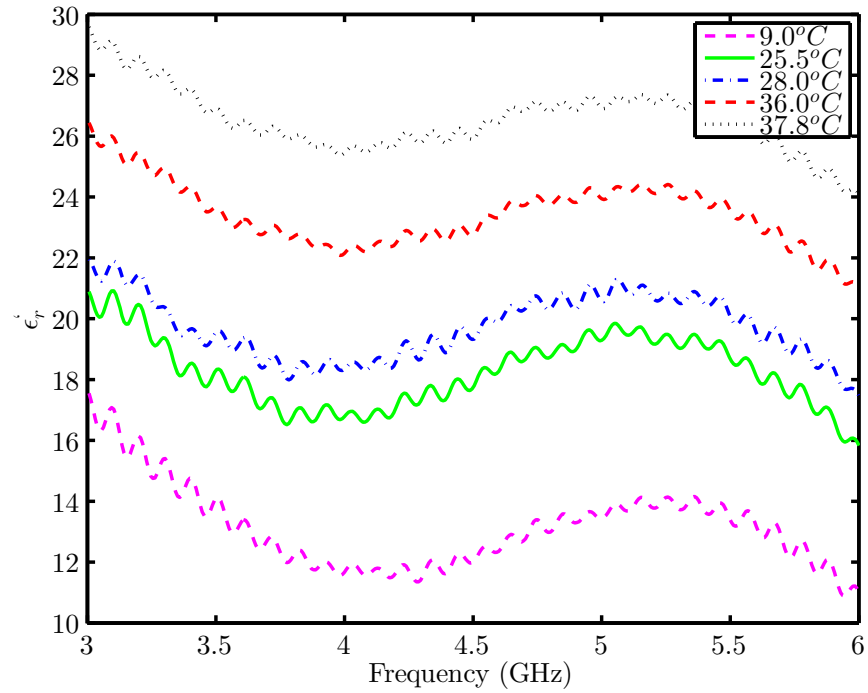


Figure 49: ϵ'_r of Isopropyl alcohol for different temperatures over the frequency range from 3 - 6 GHz, after using the Meissner & Wentz model correction.

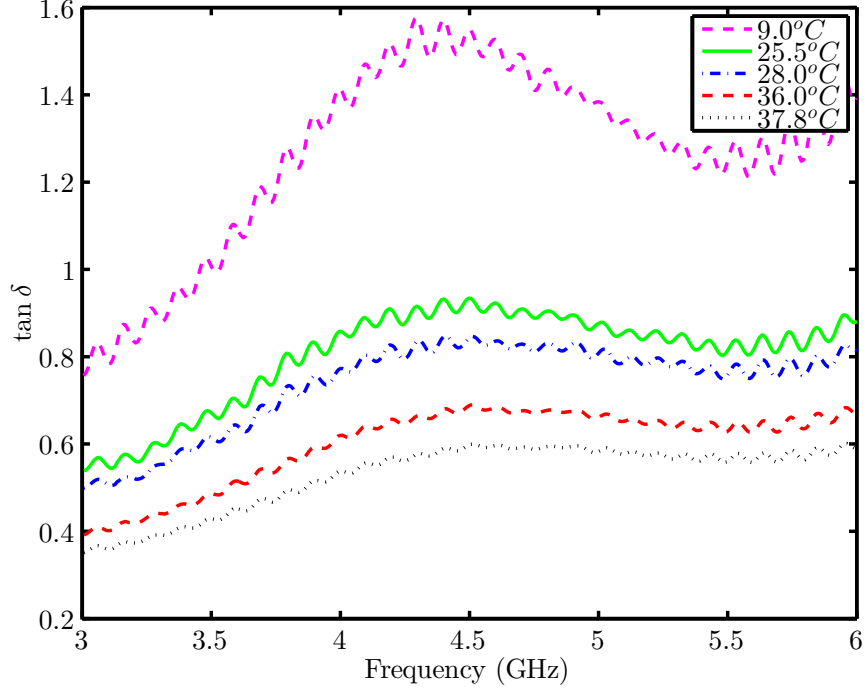


Figure 50: $\tan \delta$ of Isopropyl alcohol for different temperatures over the frequency range from 3.5 GHz to 6 GHz, after using the Meissner & Wentz model correction.

5.3 Conclusion

In this chapter, the thermo-responsiveness of materials at microwave frequencies is verified experimentally. Two materials, the liquid crystal 5CB and isopropyl alcohol, are investigated. Both the MUTs exhibit variations in ϵ'_r and $\tan \delta$ with changes in temperature. Two main conclusions are : 1) the variations in temperature result in a noticeable change in the electrical properties of these materials at microwave frequencies (3 - 6GHz), and 2) the variations in loss tangent warrant the need for reconstructing the *complex* permittivity. This suggested that for an application like REMS sensor, it will be necessary to develop a methodology to extract the complex permittivity of the material from reflected signals. Neural networks using the Levenberg Marquardt back-propagation algorithm have demonstrated the ability to reconstruct the permittivity profile of a non-dissipative material line [50]. In the next chapter, a neural network based methodology is presented to extract the complex

permittivity of materials at microwave frequencies.

CHAPTER VI

RECONSTRUCTING THE COMPLEX PERMITTIVITY

The electrical properties of materials are characterized by the complex permittivity ϵ , which describes the interaction of a material with an applied electric field. The *relative complex permittivity* is a dimensionless quantity ϵ_r defined by Eq. 2.

The real part of permittivity (ϵ'_r) is related to energy storage and the imaginary part (ϵ''_r) to dissipation. For most substrates, microstrip lines have a very low loss tangent and may be approximated as lossless. However, in liquids, ϵ''_r can be as high as ϵ'_r . For a REMS sensor electro-material line that relies on the spatially distributed electrical properties of thermotropic liquid crystals, it is important to extend the neural network based methodology to extract the complex material properties.

6.1 Reconstructing the Complex Permittivity

Different resonant and non-resonant methods have been reported in the research literature for measuring the complex permittivity of materials [17]. A monopole probe immersed into the material under investigation, as shown in Fig. 51, is considered a simple and efficient technique for determining the electrical properties of the medium. The input impedance of a monopole probe immersed in an approximately semi-infinite dielectric medium provides valuable information for extracting the complex permittivity of the medium. In the method reported in [51], the normalized impedance of the monopole probe is expressed as a rational function of order three and the coefficients of the function are determined using the profile of a standard medium. Based on the rigorous expression for the impedances of monopole antennas in half space by Gooch et al. [52], various *in-situ* procedures are reported in the literature for solving the non-linear inverse problem of calculating complex permittivities. In one approach,

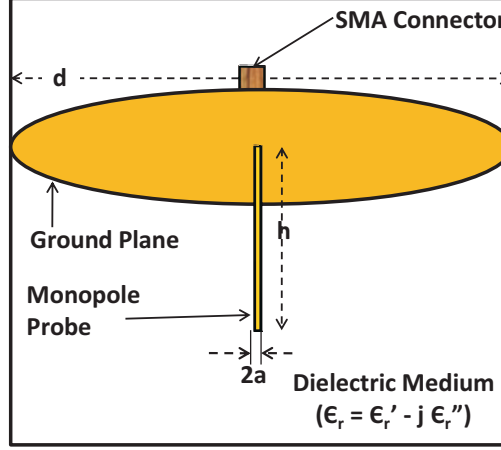


Figure 51: A monopole probe of height h , radius a , and connected to ground plane with diameter d , immersed in a dissipative dielectric medium with permittivity $\epsilon_r = \epsilon_r' - j\epsilon_r''$

the dielectric values are calculated by comparing the measured and predicted values of the input impedance using an iterative two dimensional complex zero finding routine [53]; in another a least square fit is used to match the measured and predicted input impedance [54]; and in a third an analysis of resonant peaks determined from the analytical model is used with Prony's method [55].

Neural networks using the back-propagation algorithm have demonstrated the ability to reconstruct the permittivity profile of lossless stratified medium from complex reflection coefficients [50]. For a dissipative medium, the complex-valued nature of the permittivity makes the problem incompatible with conventional neural networks, which are designed to process real-valued data. One possible approach is to use a complex-valued back-propagation neural network, which might result in better accuracy, but these are considered more difficult to implement [56]. Another possible approach is to split the network into two networks, one dealing with the real part and the other dealing with the imaginary part (with both using real valued input data). Such an approach, for a broad-band evaluation of complex permittivity, employed the finite difference time domain technique to generate training data [57]. However,

this approach has limitations such as the loss of correlation between the real and imaginary parts of the complex input data [58]. In fact, there is usually considerable correlation between the real and imaginary parts of the complex data, which can not be effectively utilized if real and imaginary values of data are manipulated independently [59].

In the proposed research, a different approach is presented which employs two back propagation networks to reconstruct the complex permittivity of dissipative media. In contrast to using the real and imaginary parts separately, the phase and magnitude of complex reflection coefficient are used as inputs to each of the two back propagation networks, out of which one solves for the real part and the other solves for the imaginary part of the complex permittivity. The network uses analytical data generated for a monopole probe using the monopole antenna model presented in [52].

6.2 The Monopole Antenna Model

The simple construction and easy application of a monopole antenna makes it a suitable option for the dielectric measurement of materials. Monopoles have been used as probes for the *in-situ* characterization of soil moisture content [55], sensors for snow and soil wetness [54], and for the measurement of electrical properties of general materials [51]. The input impedance of the monopole probe immersed in a dielectric medium depends on the electrical properties of the medium, and thus the measured reflection coefficient should provide sufficient information to extract the complex permittivity. Using the same principle, a monopole probe with a ground plane is immersed in the dielectric medium, and connected to a Vector Network Analyzer (VNA). The VNA is used to obtain the reflection coefficient of the probe through S_{11} measurements across the frequency range from 2.5 to 5GHz. The reflection coefficient is related to the input impedance of the probe through the simple relationship given by Eq. 49.

$$\Gamma = \frac{Z_{in} - Z_o}{Z_{in} + Z_o} \quad (49)$$

In Eq. 49, Γ is the complex reflection coefficient, Z_{in} is the input impedance of the monopole probe, and Z_o is the characteristic impedance of the coaxial cable connected to the probe, which in this case is 50Ω . The input impedance Z_{in} is computed using rigorous expression developed by Wu [52], and is given by

$$Z_{in}^* = \frac{\omega\mu_o}{j4k(S + CU)} \quad (50)$$

where

$$k = \beta + j\alpha = \omega \left[\mu \left(\epsilon' - j\epsilon'' \right) \right]^{1/2} \quad (51)$$

The functions S , C and U , along with the approximations inherent in these expressions, are described in detail in *Appendix A* of [53]. These functions along with k depend on the measurement frequency, the geometrical dimensions of the monopole probe (height and radius), and the dielectric properties of the medium ($\epsilon_r = \epsilon'_r - j\epsilon''_r$).

The monopole probe geometry is shown in Fig. 52, where h is the height and a is the radius of the probe, while d is the diameter of the ground plane. The probe is connected to the VNA and is immersed in the dielectric medium of relative permittivity ϵ_r . The reflection coefficient is measured using the VNA.

The size of the ground plane of the monopole, indicated by diameter d in Fig. 52, needs to be at least 4λ to be assumed infinite [55]. This assumption about the ground plane makes the application of image theory valid and enables the analytical model of Wu [52] to be used for the input impedance and reflection coefficient calculations. The validity of the model depends upon the ratio of monopole length to wavelength (h/λ), but the model is not limited to small values of h/λ . Approximations made in the model limit its range of validity to $(a/h) \ll 1$, $(a/\lambda) \ll 1$, $\beta h > 1$ and

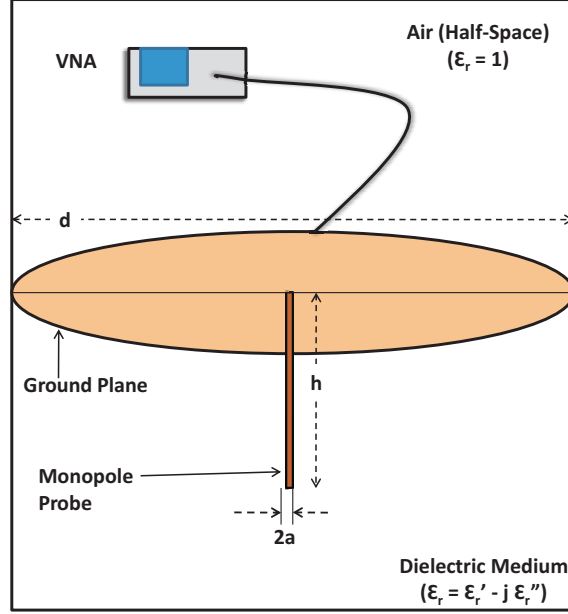


Figure 52: A monopole probe of height h and radius a , immersed in a dissipative dielectric medium with permittivity $\epsilon_r = \epsilon'_r - j\epsilon''_r$, and connected to a VNA

$(\sigma/\omega\epsilon) \leq \infty$. For a monopole antenna, the current at the top of antenna must be zero, so the current varies from its maximum value at the base to zero at the top. For short monopole antennas ($h \leq \lambda/10$), the current distribution is approximately linear, while for longer antennas ($h \approx \lambda/4$) the current distribution would be approximately sinusoidal.

In this research a 10mm long monopole probe is used, which corresponds to the first resonant frequency of around 7GHz in air. The validity of the model for a monopole probe of given length (height) is limited to a specific frequency range depending upon the ratio h/λ . For a 10mm long probe, values of relative permittivity ranging from 3 - 10 correspond to the resonant frequencies ranging from 4.5 GHz to 2.76 GHz, respectively. The phase and magnitude response to a change in complex permittivity is more pronounced close to the resonance and therefore, this model is kept limited to the frequency range from 2.5 to 5GHz for the real part of complex permittivity ranging from 3 - 10. The other factor which limits the capability of model is determined by the loss tangent of the medium. It was observed that the

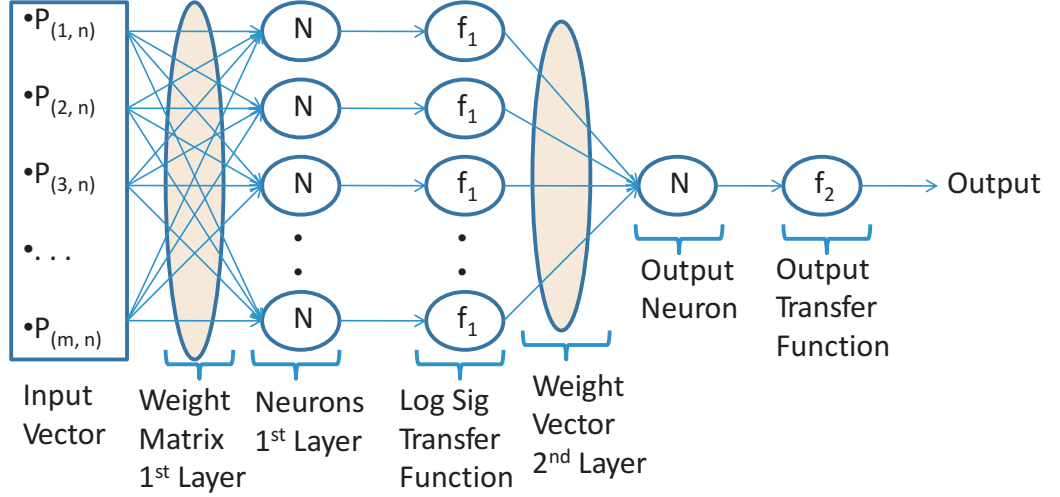


Figure 53: A two layer multiple neuron neural network

model only worked well for values of $\tan \delta \leq 0.2$, and consequently the values of ϵ_r'' were restricted to the range from 0 to 0.5. The purpose of the analytical model in this research is to generate data within the target range of permittivity values to train the back-propagation neural network.

6.3 Neural Network Model for Complex Permittivity

A two-layered artificial neural network, using the Levenberg Marquardt back-propagation algorithm, is used to back solve the complex permittivity of the medium. The proposed network can be trained using an analytical model, numerical model, or measurement data spread over the complete range of parameters of interest. The input training data for the non-linear inverse problem of reconstructing the complex permittivity comprises the complex reflection coefficient of the monopole probe. The network is trained using the analytical model for impedances of monopole antennas in a half space by Gooch et al. [52].

The methodology employed uses the input data in polar representation (magnitude and phase) instead of Cartesian representation (real and imaginary) and thus allows the use of real-valued artificial neural networks for solving the complex permittivity.

The architecture of a two layered back-propagation neural network is shown in Fig. 53. The input to the network consists of the magnitude and phase of the measured reflection coefficient, arranged in the fashion similar to the vectors of matrix D .

Two separate networks are integrated, using the complex reflection coefficient as the input in the form described in Eq. 46. Each input vector corresponds to the reflection coefficient for one specific value of complex permittivity, computed using the analytical model described in previous section. An appropriate number of neurons was determined through simulations and comparison, and it was found that a network with a hidden layer having 25 neurons gives superior performance in terms of mean square error. Despite having the same input training data and neuron layer architecture, the two networks differ in terms of weight matrices. They are tracking different outputs and thus the performance function will respond differently to the same weights for tracking the output and minimizing the error. The setup comprises two networks, identical in architecture, but having different performance functions, weight matrices and outputs. The two outputs are combined together to reconstruct the complex permittivity as shown in Fig. 54. In the input vector $|\Gamma_{fn}|$ and $\angle\Gamma_{fn}$ indicates the magnitude and phase of input reflection coefficient computed/measured for frequency f_n . The complete frequency range of interest is divided into n steps.

The training data comprising the complex reflection coefficients was generated for 21 frequency steps of 130MHz each from 2.5GHz to 5GHz. The real part of complex permittivity (ϵ'_r) was swept from 3.0 to 10.0 with an increment of 0.05, while the imaginary part (ϵ''_r) was swept across 0 to 0.5 with a step size of 0.005. The setup resulted in a training matrix D of dimension 42×14241 , easily handled by a common desktop computer.

The computed values of input vectors corresponding to different values of complex permittivity are shown in Fig. 55. The network was then tested using test data corresponding to 231 different values of ϵ_r , which were not used for training the

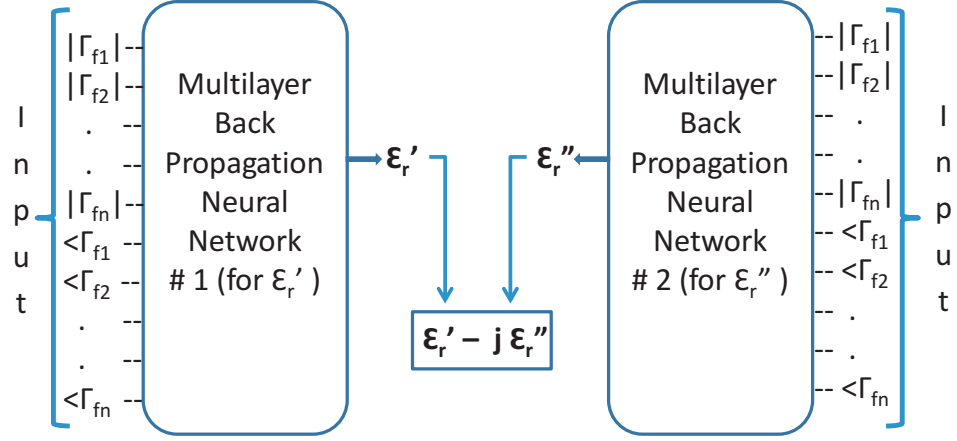


Figure 54: The neural network model comprising two networks, #1 solving for ϵ_r' and #2 reconstructing ϵ_r'' , using the Levenberg Marquardt back-propagation algorithm

network. The results were very accurate and 6 randomly picked results are listed in Table 7. To confirm that network has converged to the global minima and not a local minima, the simulation was repeated multiple times and the results were observed for consistency, following [36]. The network was tested thrice and each time correct values of complex permittivity were reconstructed. In each case, the error observed was less than 1%.

Table 7: The actual values of complex permittivity ($\epsilon_r = \epsilon_r' - j\epsilon_r''$) compared to the neural network output

Actual Values	Neural Network Output	% Error
3.01 - j0.015	3.01 - j0.015	0
4.59 - j0.36	4.59 - j0.36	0
5.9 - j0.213	5.9 - j0.213	0
7.23 - j0.5	7.23 - j0.5	0
8.9 - j0.3	8.9 - j0.3	0
9.79 - j0.03	9.79 - j0.03	0

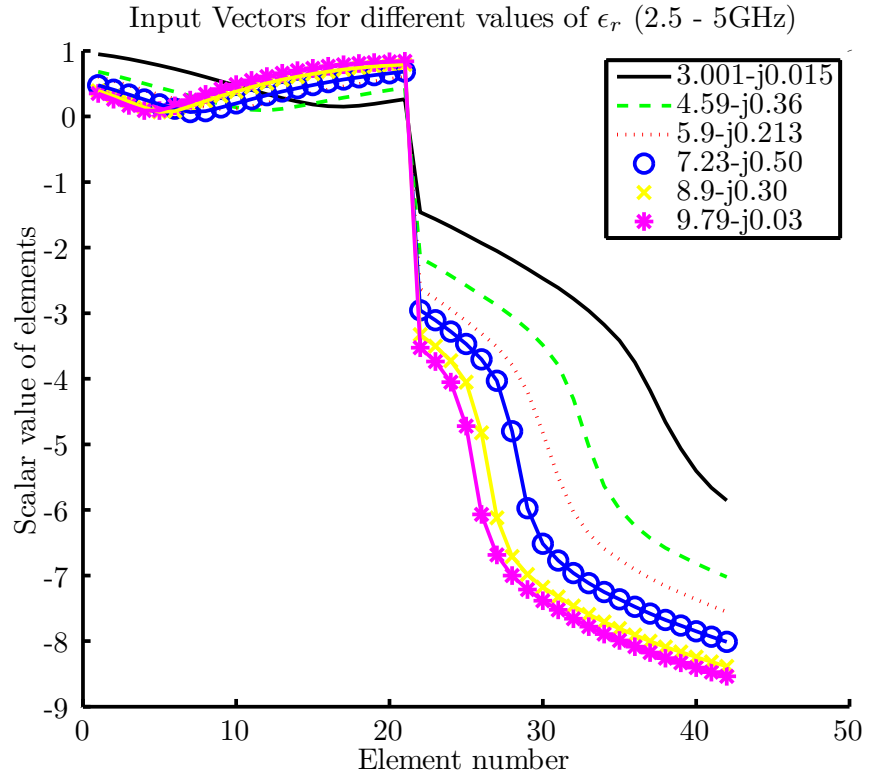


Figure 55: The input vectors corresponding to different values of the complex permittivity $\epsilon_r = \epsilon'_r - j\epsilon''_r$

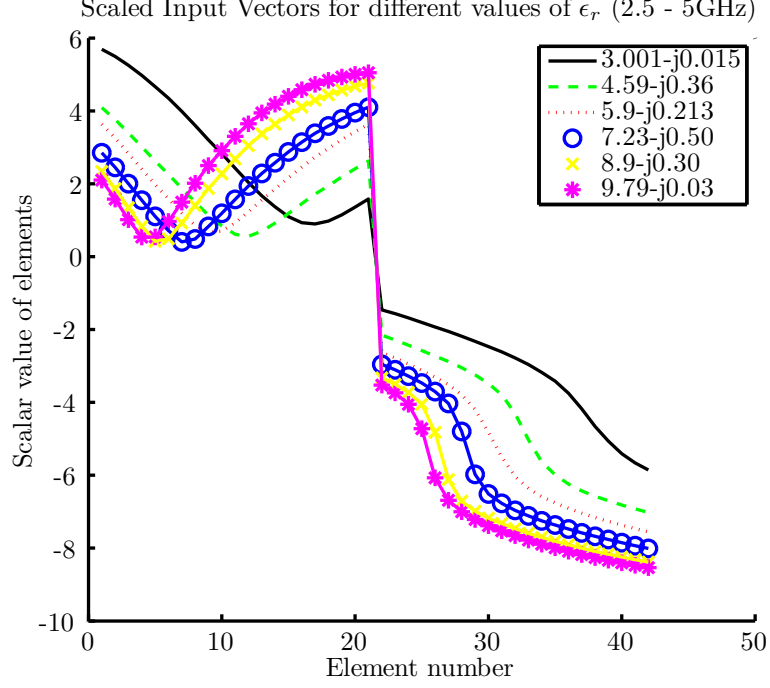


Figure 56: Scaled input vectors corresponding to different values of the complex permittivity $\epsilon_r = \epsilon'_r - j\epsilon''_r$

6.4 Measurement of Complex Permittivity using Scaled Inputs

The model presented in the previous sections works accurately for pure data [60], however it was observed to be sensitive to the presence of measurement noise (simulated by adding white Gaussian noise) and comparatively higher percentage of errors was observed in the estimated values of ϵ''_r . A relationship was observed for the change in $|\Gamma|$ in response to the change in ϵ''_r . To address the problem, the data matrix D was modified to D_{sc} by scaling the magnitude of reflection coefficient by a factor N as shown in Eq. 52.

$$D_{sc} = \begin{bmatrix} N \times |\Gamma| \\ \angle \Gamma \end{bmatrix} \quad (52)$$

The appropriate value of scaling factor was found to be $N \approx 6$. Different vectors from D_{sc} corresponding to the different values of complex ϵ_r are shown in Fig. 56.

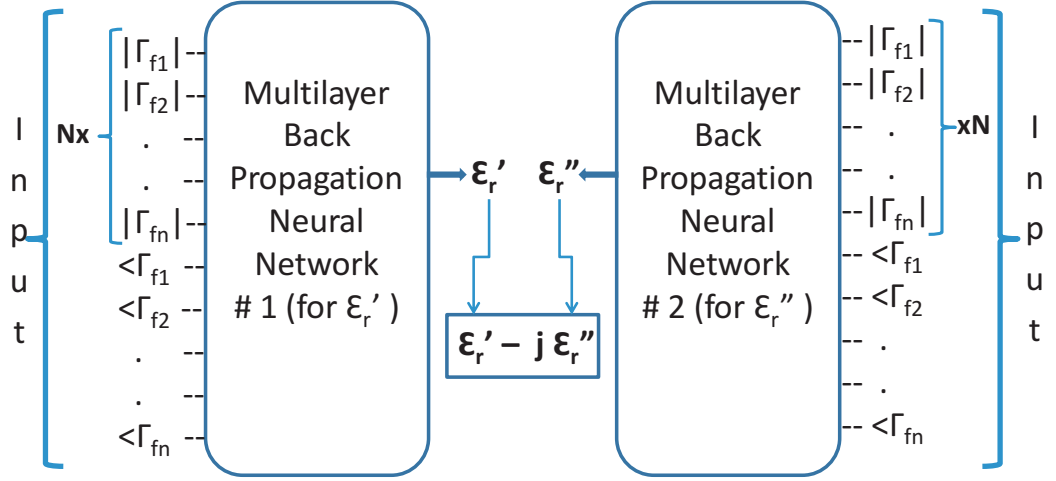


Figure 57: The neural network model comprising two networks with scaled inputs, #1 solving for ϵ_r' , and #2 reconstructing ϵ_r'' , using the Levenberg Marquardt back-propagation algorithm

Two separate networks are employed using the complex reflection coefficient as the input in the form described in Eq. 52. The two outputs are combined together to reconstruct the complex permittivity as shown in Fig. 57.

Measurement noise was simulated by adding white Gaussian noise with 10dB SNR to the training data, and then same proportion of noise was induced in the test data as well. The network was then tested using test data corresponding to 231 different values of ϵ_r that were not used for training the network. The results were found to be quite accurate and the recorded percent error was less than 3.5%. The results are tabulated in Table 8.

Table 8: The actual values of complex permittivity ($\epsilon_r = \epsilon_r' - j\epsilon_r''$) compared to the two sets of estimated values and the respective percent error over the frequency range 2.5-5GHz

Actual Values	NN Output(Set1)	% Error	NN Output(Set2)	% Error
3.01 - j 0.015	2.98 - j0.037	0.84	2.98 - j0.023	0.59
4.59 - j 0.36	4.49 - j0.25	3.21	4.56 - j0.41	1.26
5.27 - j 0.213	5.29 - j0.18	0.78	5.21 - j0.25	1.37
5.9 - j 0.5	5.82 - j0.45	1.49	5.91 - j0.45	0.87

The frequency range was selected by the resonant frequency of the monopole

corresponding to the ϵ_r values of the medium. It was observed that the frequency range could be further narrowed down by shrinking the range of complex permittivity values. The same setup was used with the frequency range from 3.5 to 5 GHz by limiting the sweep range of ϵ'_r from 3 to 6. The input vectors for 4 different ϵ_r values are shown in Fig. 58.

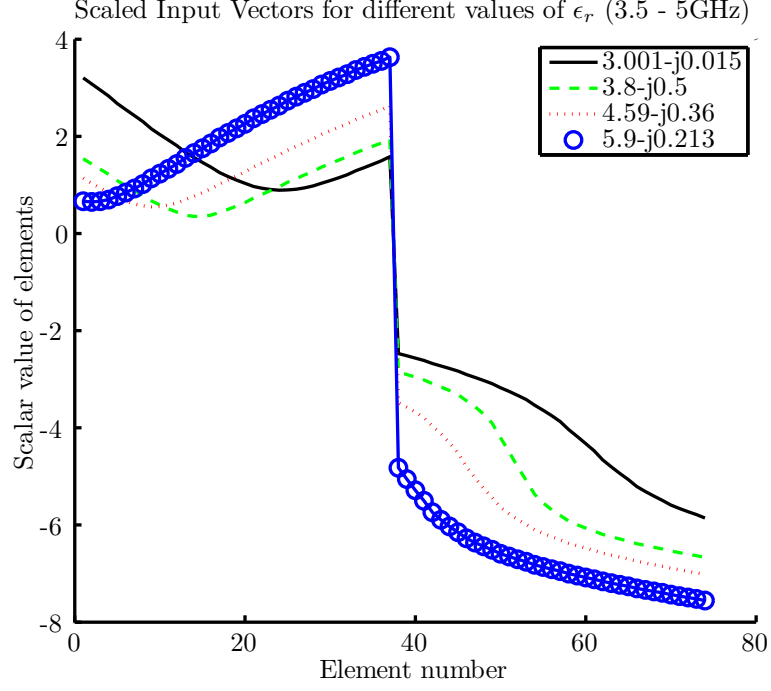


Figure 58: Scaled input vectors corresponding to the different values of complex permittivity $\epsilon_r = \epsilon'_r - j\epsilon''_r$

The back-propagation based neural network model was trained with the input data arranged in the form identified by matrix D_{sc} in Eq. 52. The training data matrix was

Table 9: The actual values of complex permittivity ($\epsilon_r = \epsilon'_r - j\epsilon''_r$) compared to the two sets of estimated values and the respective percent error over the frequency range 3.5-5GHz

Actual Values	NN Output(Set1)	% Error	NN Output(Set2)	% Error
3.01 - j0.015	3.08 - j0.05	2.87	3.04 - j0.026	1.36
4.59 - j0.36	4.67 - j0.51	3.86	4.62 - j0.35	0.78
5.27 - j0.213	5.32 - j0.21	0.97	5.24 - j0.19	0.75
5.9 - j0.5	5.69 - j0.49	3.51	5.86 - j0.37	2.29

generated using the same step size for frequency and ϵ_r'' , while the incremental step was reduced to 0.025 for ϵ_r' , resulting in a training data matrix with dimensions 38×12221 . The network with reduced frequency range was tested with the test vectors, and the percent error observed in presence of the white Gaussian noise (10dB SNR) was less than 4% . The results for two sets of 4 randomly selected values, incorporating white gaussian noise with 10dB SNR, are tabulated in Table 9.

The frequency range was further reduced to 4 - 5 GHz, and the same network model was employed to reconstruct the complex ϵ_r . The error remains less than 4% as shown in Table. 10.

Table 10: The actual values of complex permittivity ($\epsilon_r = \epsilon_r' - j\epsilon_r''$) compared to the two sets of estimated values and the respective percent error over the frequency range 4-5GHz

Actual Values	NN Output(Set1)	% Error	NN Output(Set2)	% Error
3.01 - j0.015	3.1092 - j0.1149	1.1691	3.1570 - j0.1273	1.9768
4.59 - j0.36	4.6174 - j0.3403	0.733	4.5729 - j0.2114	3.2489
5.27 - j0.213	5.0794 - j0.2960	3.9415	5.2315 - j0.2461	0.9626
5.9 - j0.5	5.5745 - j0.3278	3.0636	5.7088 - j0.4846	0.6244

6.5 Complex ϵ_r Measurements using One Neural Network

After developing the capability to backsolve complex ϵ_r using two neural networks integrated together, the same approach was evaluated for single neural network with scaled inputs. The complex reflection coefficient was used as the input training data and it was scaled and organized in the form of a data matrix D_{sc} as shown in Eq. 52. The network architecture comprised one hidden layer with 25 neurons and an output layer with 2 neurons. The output neurons track ϵ_r' and ϵ_r'' as real valued scalars, and the complex valued ϵ_r is recreated as shown in Fig. 59.

For the same frequency range and permittivity parameters, the setup was trained and tested in presence of white Gaussian noise with 10dB SNR. The results for two sets of 4 randomly selected values out of 231 test vectors are tabulated in Table 11.

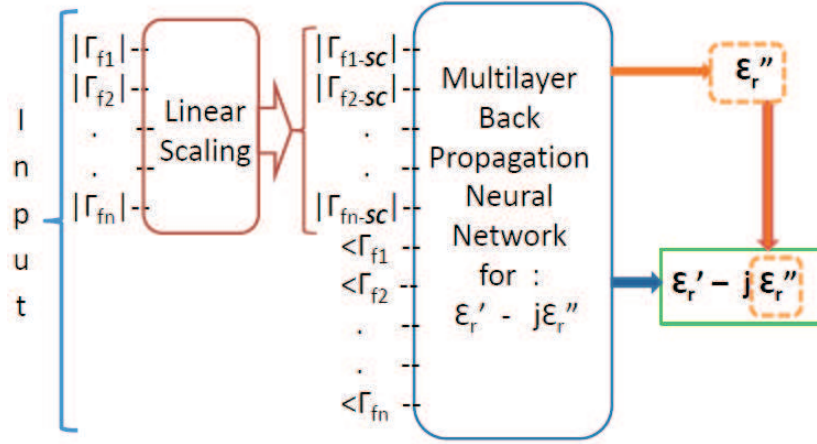


Figure 59: The neural network model having only one network with scaled inputs, #1 solving for ϵ_r' , and #2 reconstructing ϵ_r'' , using the Levenberg Marquardt back-propagation algorithm

It can be observed from the results that the complex ϵ_r was reconstructed with an error less than 7%. In addition to the overall increase in error, the mean error in ϵ_r'' soared to 31.5%.

6.6 Discussion

Reconstructing complex permittivity by tracking ϵ_r' and ϵ_r'' or $\tan \delta$ comprises two non-linear inverse problems. When using one neural network, one of the factors causing degradation in performance is that one network is solving two non-linear problems while when using two networks integrated together, each network is solving one non-linear inverse problem. The model with two networks integrated together

Table 11: The actual values of complex permittivity ($\epsilon_r = \epsilon_r' - j\epsilon_r''$) compared to the two sets of estimated values using 1 neural network, and the respective percent error over the frequency range 4-5GHz

Actual Values	NN Output(Set1)	% Error	NN Output(Set2)	% Error
3.01 - j0.015	3.0978 - j0.1972	1.52	3.2167 - j0.2736	5.476
4.59 - j0.36	4.7019 - j0.1587	5	4.7442 - j0.1062	6.45
5.27 - j0.213	5.1822 - j0.2655	1.94	5.4121 - j0.2870	3.04
5.9 - j0.5	5.8122 - j0.3837	2.28	5.6529 - j0.3280	2.28

gives superior performance in terms of accuracy, and therefore it is selected for reconstructing the spatially distributed permittivity profile of a lossy electro-material line. The accuracy of the network output is dependent upon the accuracy of the analytical / numerical model used for training the network. The problem complexity will vary with the type of medium, for which some a priori knowledge is required to train the neural networks. This approach can be used successfully for any range of values for real and imaginary part of complex permittivity as long as the size of data set remains within the computing capability of the computer. For example, if the permittivity values of an unknown medium fall somewhere in the range of $2 \geq \epsilon'_r \leq 100$ and $0 \geq \epsilon''_r \leq 100$, the data matrix may be generated with a comparatively coarser step size with less resolution. The accuracy of the results would then depend upon the accuracy of the model and the resolution of the training data, and it was observed in a limited domain that the accuracy of the model does cover up for the coarseness of training data. This methodology can be utilized for the measurements of complex permittivity of thermotropic liquid crystals and thermo-responsive materials used in the REMS sensor.

CHAPTER VII

DISSIPATIVE ELECTRO-MATERIAL LINE

The thermo-responsiveness of dissipative materials, such as liquid crystals, at microwave frequencies, warrants the need of formulating a system to backsolve the spatially distributed permittivity profile of a lossy electro-material line. The method to backsolve the permittivity profile of a lossless electro-material line is described in Chapter IV, and the ability to reconstruct complex permittivity of a homogeneous material using an ANN is demonstrated in Chapter VI. In this chapter, an ANN based method is demonstrated to reconstruct the spatially distributed permittivity profile of a lossy electro-material line.

7.1 Setting up the Problem

For a n segment lossless electro-material line, if the real permittivity values are discretized such that the complete range is divided into m discrete values, then the training data set will have m^n vectors. For a lossy electro-material line, we are dealing with complex permittivity, which can either be split into ϵ'_r and ϵ''_r , or can be expressed in terms of ϵ'_r and $\tan \delta$. In either case, if ϵ'_r is discretized into m discrete values and ϵ''_r or $\tan \delta$ is discretized into mm discrete values over the respective ranges, the resultant training data will have $(m \times mm)^n$ vectors. This increase in the training data size poses an initial challenge in terms of memory limitations of a common desktop computer using the backpropagation algorithm.

For a three section lossy electro-material line, if $2 \leq \epsilon'_{r1,2,3} \leq 4$, with $\Delta \epsilon'_{r1,2,3} = 0.2$, and $0 \leq \tan \delta \leq 0.1$ (or $0 \leq \epsilon''_{r1,2,3} \leq 0.4$) with $\Delta \tan \delta = 0.01$, the training data set requires with 100^3 vectors, which becomes challenging for the backpropagation NN algorithm in terms of memory handling of a common computer. Therefore, a

narrower range of permittivity values was selected, $2.2 \leq \epsilon'_r \leq 2.6$ with $\Delta\epsilon'_r = 0.1$, and $0.01 \leq \tan \delta \leq 0.05$ with step size $\Delta \tan \delta = 0.01$, resulting in a data set comprising $(5 \times 5)^3 = 15625$ vectors.

Training vectors for the three section lossy electro-material line were obtained by cascading the magnitude and phase of the input reflection coefficient (Γ_{in}) into a single vector as described in Eq. 46

The input training vectors for 17 different values of complex permittivity ($2.2 \leq \epsilon'_{r1,2,3} \leq 2.6$ and $0.022 \leq \epsilon''_{r1,2,3} \leq 0.13$) are shown in Fig. 60. The frequency was swept from 3.25 GHz to 4.75 GHz with a step size $\Delta f = 100 MHz$. It can be observed that as the value of ϵ'_r is varied from 2.2 to 2.6 and $\tan \delta$ is varied from 0.01 to 0.05 in the three bins of lossy electro-material line, the variations in $|\Gamma|$ (the first half of the training vector) are much more pronounced than the variations in $\angle \Gamma$ (the second half of the training vector).

The offset between variations in $|\Gamma|$ and $\angle \Gamma$ leads to the idea that for systematic training of the neural network, linear scaling $\angle \Gamma$ with a factor N , will effectively distribute the information evenly. For the lossy electro-material line with given parameters, the linear scaling factor to scale $\angle \Gamma$ was calculated to be $N \approx 5$. The resultant evenly spread input vectors for 17 different values of complex permittivity ($2.2 \leq \epsilon'_{r1,2,3} \leq 2.6$ and $0.022 \leq \epsilon''_{r1,2,3} \leq 0.13$) are shown in Fig. 61, and the scaled data matrix is given by:

$$D = \begin{bmatrix} |\Gamma| \\ N \times \angle \Gamma \end{bmatrix} \quad (53)$$

The problem of reconstructing complex permittivity is made compatible with the real valued conventional neural networks by backsolving the real and imaginary parts of complex permittivity as real numbers and then adding them together to recreate the complex permittivity [61]. The problem is split into two parts: reconstructing the

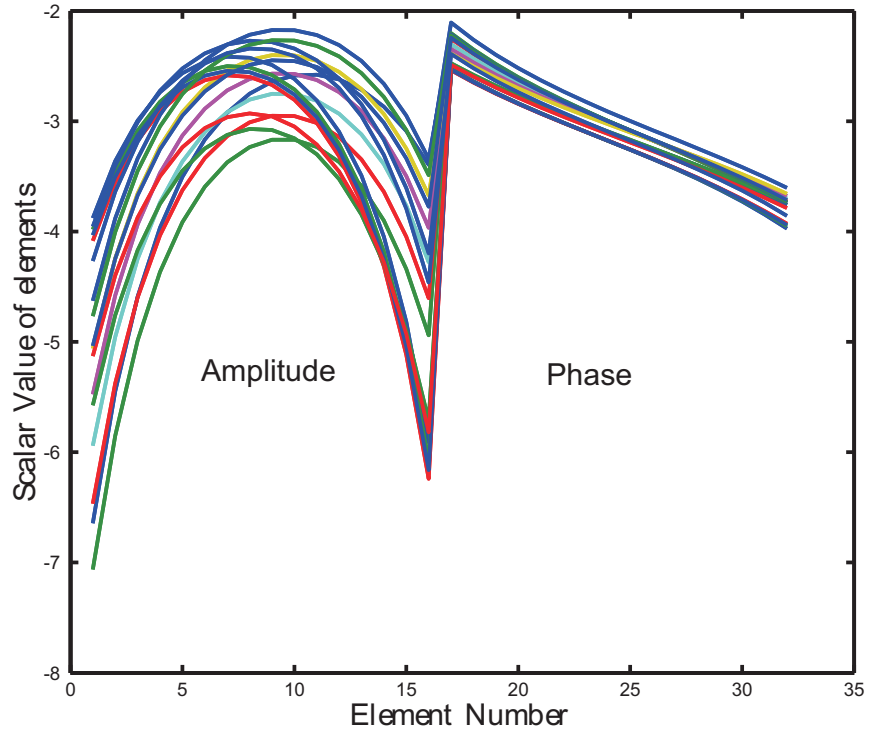


Figure 60: Input training vectors for 17 different sets of $\epsilon_{r1,2,3}$. The change in magnitude of Γ_{in} is much more pronounced as compared to the change in phase across the range complex permittivity values of interest.

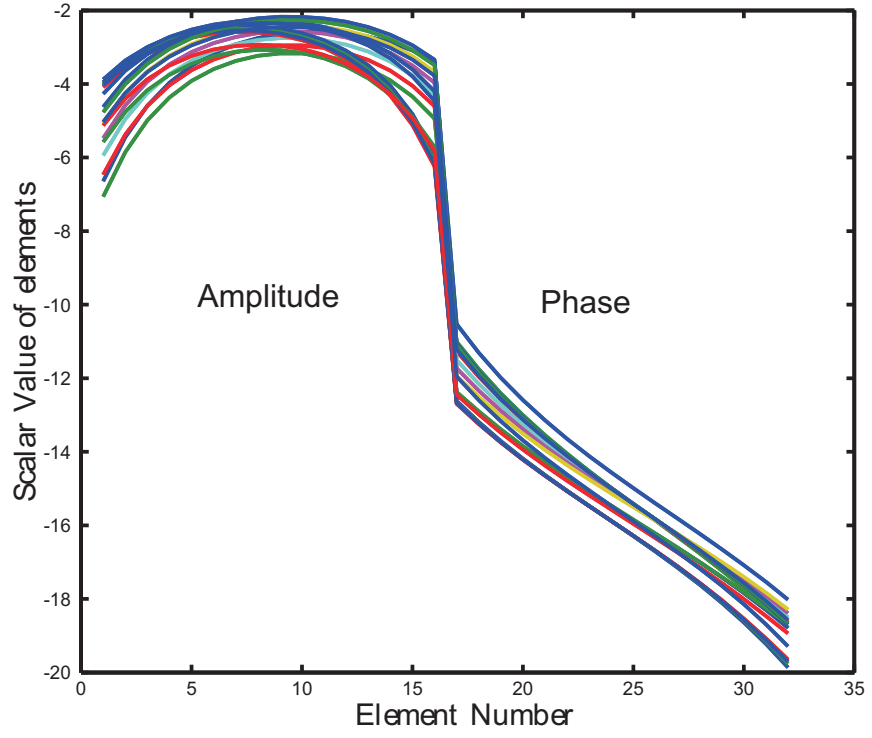


Figure 61: Input training vectors for 17 different sets of $\epsilon_{r1,2,3}$. Phase is scaled by the 5 to evenly distribute the information across all elements of input vector. The scaling factor is determined through linear scaling.

1) real part of permittivity ϵ'_r , and 2) the imaginary part ϵ''_r , of a lossy electro-material line. To simplify the algorithm and make it more easily interpretable for all ranges of real part of permittivity, the relationship between the real part and imaginary part is expressed in terms of $\tan \delta$.

7.2 Variation in Γ_{in} in response to variations in ϵ_r

There can be different scenarios in terms of variations in permittivity of different segments of an electro-material line. In this section, four different scenarios are discussed, in which $\epsilon'_{r1,2,3}$ and $\tan \delta_{1,2,3}$ of the electro-material line are varied in different combinations, and the response is discussed in terms of magnitude and phase of Γ_{in} .

7.2.1 Case 1 : Varying ϵ'_{r2} only

To understand the effect of variations in complex permittivity on Γ_{in} of an electro-material line, a three section lossy electro-material line was simulated by cascading three microstrip transmission lines. In the first scenario, the real part of permittivity of the first and third segments are set to 3.5 and 5.5, respectively ($\epsilon'_{r1} = 3.5$, $\epsilon'_{r3} = 5.5$). The loss tangents of the three sections are denoted by $\tan \delta_1$, $\tan \delta_2$, and $\tan \delta_3$, and are also fixed to a constant value of 0.01. The real part of permittivity of the center bin, ϵ'_{r2} , is varied from 2 to 5 as given in the complete configuration in Eq. 54 - Eq. 60:

$$\epsilon'_{r1} = 3.5 \quad (54)$$

$$2 \leq \epsilon'_{r2} \leq 5 \quad (55)$$

$$\Delta \epsilon_{r2} = 0.3 \quad (56)$$

$$\epsilon'_{r3} = 5.5 \quad (57)$$

$$\tan \delta_1 = \tan \delta_2 = \tan \delta_3 = 0.01 \quad (58)$$

$$f = 1GHz \rightarrow 6GHz \quad (59)$$

$$\Delta f = 100MHz \quad (60)$$

The magnitude and phase of Γ_{in} for four different values of ϵ'_{r2} are shown in Fig. 62 and Fig. 63, respectively.

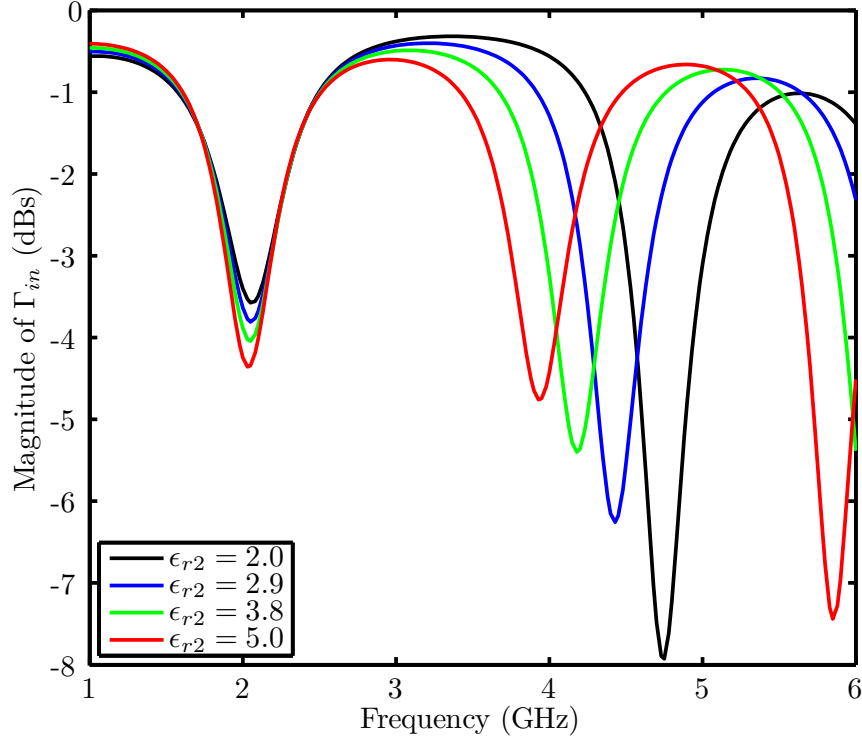


Figure 62: $|\Gamma_{in}|$ for three section lossy electro-material line with $\epsilon'_{r1} = 3.5$, $\epsilon'_{r3} = 5.5$, $\tan \delta_1 = \tan \delta_2 = \tan \delta_3 = 0.01$. Four different values of ϵ'_{r2} are used, $\epsilon'_{r2} = 2.0, 2.9, 3.8, 5.0$, to demonstrate the effect of varying ϵ'_r while keeping $\tan \delta$ fixed.

It can be observed from Fig. 62 and Fig. 63 that as the value of ϵ'_{r2} increases, the resonant frequency decreases. The shift in the resonant frequency with change in permittivity is explained through the dependence of characteristic impedance (Z_o) on the permittivity of the transmission line. With an increase in ϵ'_r , Z_o decreases, and causes the resonant frequency to decrease. The important observation here is that to backsolve the change in ϵ'_r , the information is embedded in both the magnitude and phase of Γ_{in} , as also highlighted in [50].

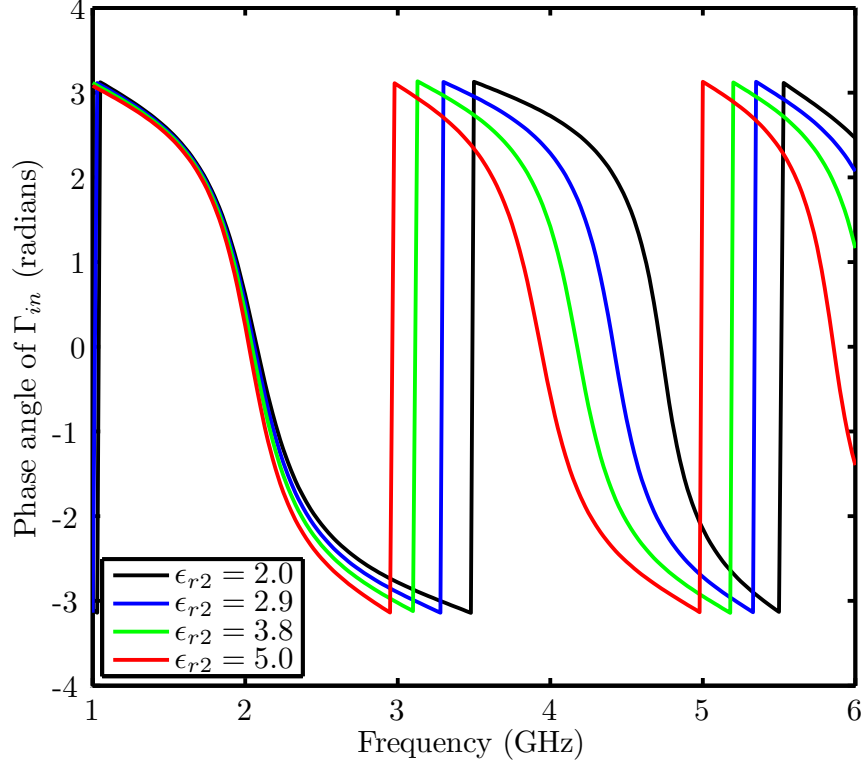


Figure 63: Phase of Γ_{in} for three section lossy electro-material line with $\epsilon'_{r1} = 3.5$, $\epsilon'_{r3} = 5.5$, $\tan \delta_1 = \tan \delta_2 = \tan \delta_3 = 0.01$. Four different values of ϵ'_{r2} are used, $\epsilon'_{r2} = 2.0, 2.9, 3.8, 5.0$, to demonstrate the effect of varying ϵ'_r while keeping $\tan \delta$ fixed.

7.2.2 Case 2 : Varying $\tan \delta_2$ only

In this case, all parameters are fixed to constant values except $\tan \delta_2$. The complete configuration is given by Eq. 61 - Eq. 68:

$$\epsilon'_{r1} = 3.5 \quad (61)$$

$$\epsilon'_{r2} = 2 \quad (62)$$

$$\epsilon'_{r3} = 5.5 \quad (63)$$

$$\tan \delta_1 = \tan \delta_3 = 0.01 \quad (64)$$

$$0.01 \leq \tan \delta_2 \leq 0.31 \quad (65)$$

$$\Delta \tan \delta_2 = 0.03 \quad (66)$$

$$f = 1GHz \rightarrow 6GHz \quad (67)$$

$$\Delta f = 100MHz \quad (68)$$

The magnitude and phase of Γ_{in} for four different values of $\tan \delta_2$ are shown in Fig. 64 and Fig. 65, respectively.

It can be observed from Fig. 64 and Fig. 65 that as the value of $\tan \delta_2$ varies, there is no affect on the resonant frequency (f_0). Fluctuations in $\tan \delta$ does not cause a shift in f_0 , and thus there is no noticeable/significant change in the phase angle of Γ_{in} as $\tan \delta$ is varied. However, $|\Gamma_{in}|$ varies as $\tan \delta$ is increased or decreased. This leads to an important conclusion that the information about changes in $\tan \delta$ is completely embedded in $|\Gamma_{in}|$, and there is not sufficient useful information in the phase of Γ_{in} . Therefore, to reconstruct the complex permittivity of a lossy electro-material line, if the electrical properties are represented in terms of ϵ'_r and $\tan \delta$, $|\Gamma_{in}|$ provides sufficient information to reconstruct $\tan \delta$. However, to backsolve ϵ'_r , both the phase and magnitude of Γ_{in} are required, as highlighted in case 1 and demonstrated in [50, 62].

7.2.3 Case 3 : Varying $\tan \delta_1, \tan \delta_2$ and $\tan \delta_3$ while $\epsilon'_{r1} = \epsilon'_{r2} = \epsilon'_{r3}$

In this scenario, $\tan \delta$ is varied in all the three sections of electro-material line while keeping $\epsilon'_{r1} = \epsilon'_{r2} = \epsilon'_{r3} = 3.5$. The details of parameters are given in Eq. 69 - Eq. 74:

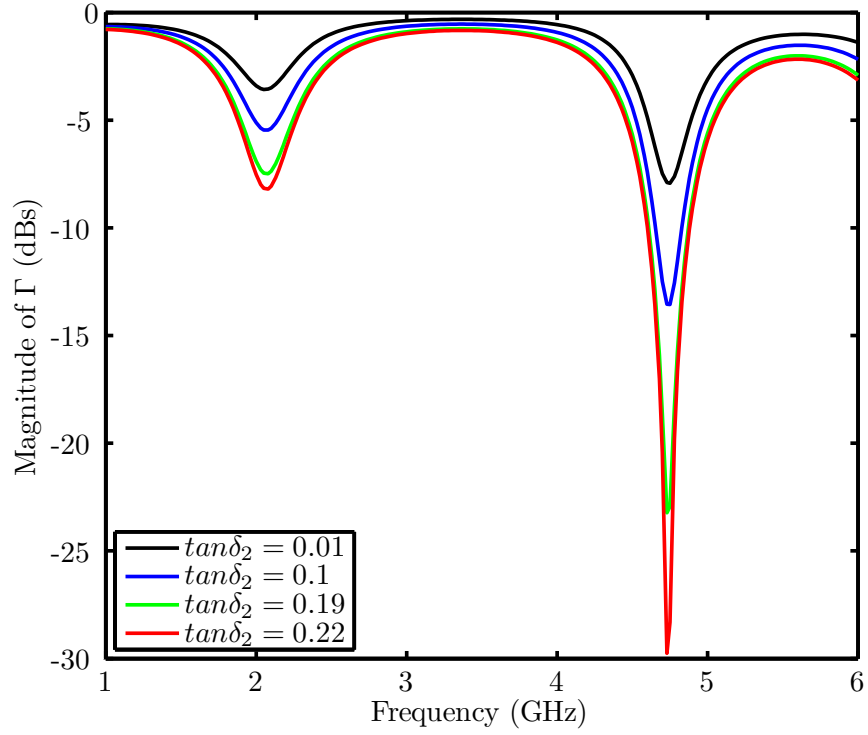


Figure 64: $|\Gamma_{in}|$ for three section lossy electro-material line with $\epsilon'_{r1} = 3.5$, $\epsilon'_{r2} = 2$, $\epsilon'_{r3} = 5.5$, $\tan \delta_1 = \tan \delta_3 = 0.01$. To demonstrate the effect of varying $\tan \delta$ while keeping ϵ'_r fixed, four different values of $\tan \delta_2$ are used, $\tan \delta_2 = 2.0, 2.9, 3.8, 5.0$.

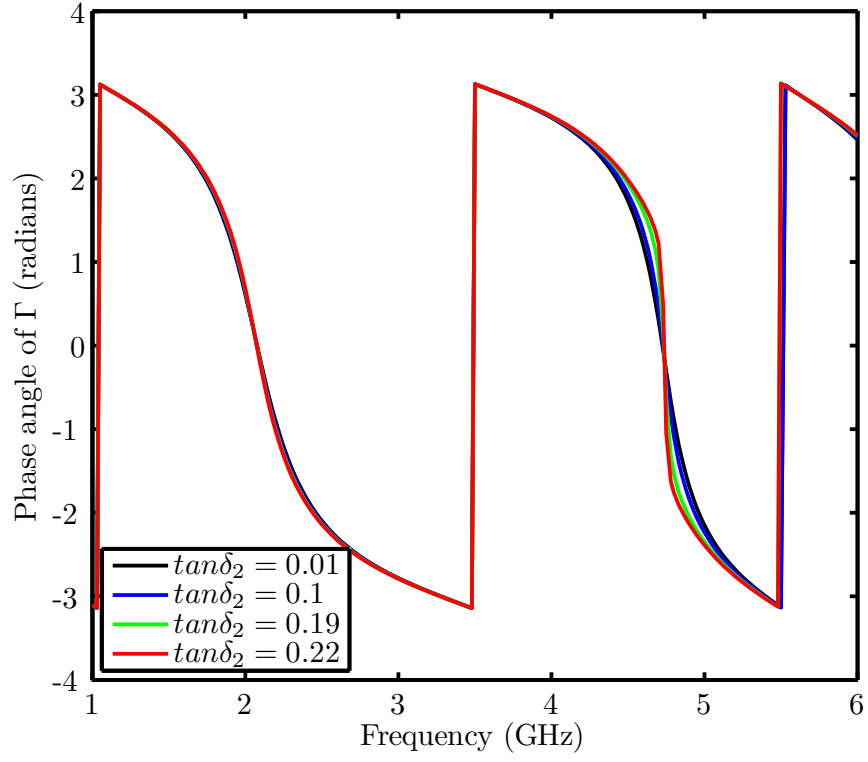


Figure 65: Phase of Γ_{in} for three section lossy electro-material line with $\epsilon'_{r1} = 3.5$, $\epsilon'_{r2} = 2$, $\epsilon'_{r3} = 5.5$, $\tan \delta_1 = \tan \delta_3 = 0.01$. To demonstrate the effect of varying $\tan \delta$ while keeping ϵ'_r fixed, four different values of $\tan \delta_2$ are used, $\tan \delta_2 = 2.0, 2.9, 3.8, 5.0$.

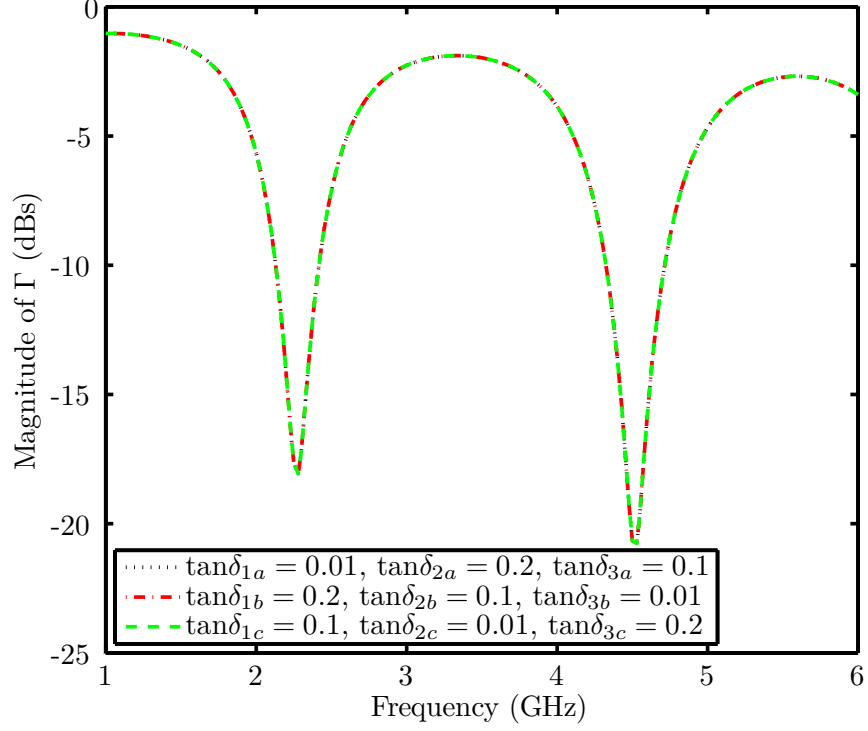


Figure 66: $|\Gamma_{in}|$ for three section lossy electro-material line with $\epsilon'_{r1} = \epsilon'_{r2} = \epsilon'_{r3}$, while varying $\tan \delta_{1,2,3}$. To demonstrate the effect of varying $\tan \delta$ while keeping ϵ'_r fixed, three different combinations of $\tan \delta_{1,2,3}$ are used satisfying the equality described in Eq. 75.

$$\epsilon'_{r1} = \epsilon'_{r2} = \epsilon'_{r3} = 3.5 \quad (69)$$

$$\tan \delta_{1a} = 0.01, \tan \delta_{1b} = 0.2, \tan \delta_{1c} = 0.1 \quad (70)$$

$$\tan \delta_{2a} = 0.2, \tan \delta_{2b} = 0.1, \tan \delta_{2c} = 0.01 \quad (71)$$

$$\tan \delta_{3a} = 0.1, \tan \delta_{3b} = 0.01, \tan \delta_{3c} = 0.2 \quad (72)$$

$$f = 1 \text{ GHz} \rightarrow 6 \text{ GHz} \quad (73)$$

$$\Delta f = 100 \text{ MHz} \quad (74)$$

The magnitude and phase of Γ_{in} of the lossy electro-material line are shown in Fig. 66 and Fig. 67, respectively. Three different combinations of $\tan \delta_{1,2,3}$ are used as highlighted in Eq. 69 - Eq. 74.

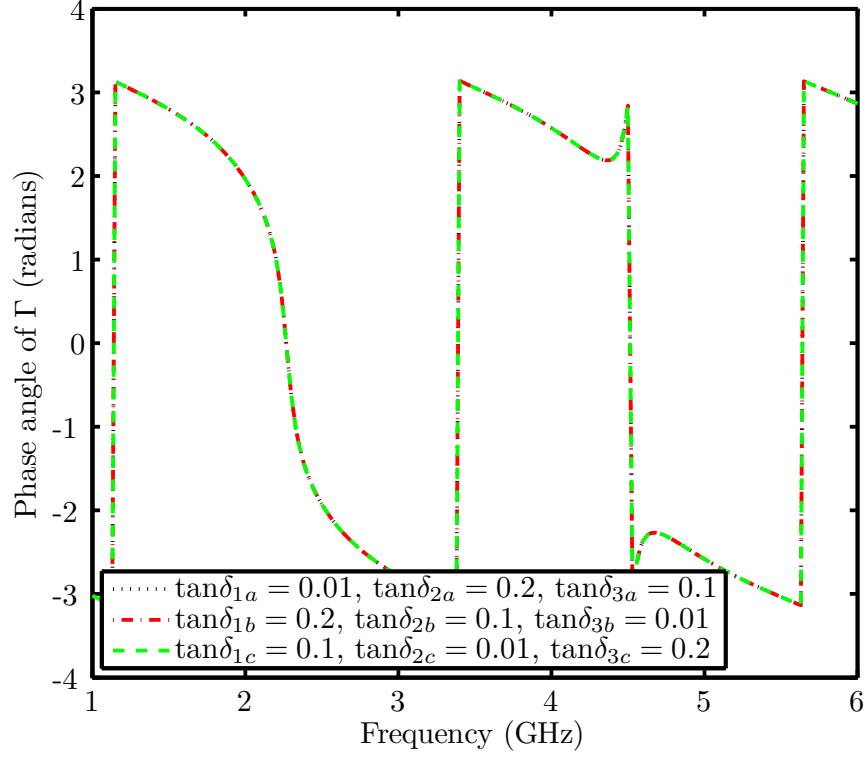


Figure 67: Phase of Γ_{in} for three section lossy electro-material line with $\epsilon'_{r1} = \epsilon'_{r2} = \epsilon'_{r3}$, while varying $\tan\delta_{1,2,3}$. To demonstrate the effect of varying $\tan\delta$ while keeping ϵ'_r fixed, three different combinations of $\tan\delta_{1,2,3}$ are used satisfying the equality described in Eq. 75.

$$\tan \delta_{1a} + \tan \delta_{2a} + \tan \delta_{3a} = \tan \delta_{1b} + \tan \delta_{2b} + \tan \delta_{3b} = \tan \delta_{1c} + \tan \delta_{2c} + \tan \delta_{3c} = \tan \delta_{sum} \quad (75)$$

From Fig. 66 and Fig. 67, it can be noticed that if $\epsilon'_{r1} = \epsilon'_{r2} = \epsilon'_{r3}$, no detectable change in phase and magnitude of Γ_{in} is caused by varying the values of $\tan \delta_1$, $\tan \delta_2$ and $\tan \delta_3$, as long as the equality defined in Eq. 75 is satisfied. There is neither any shift in f_0 nor any variation in $|\Gamma_{in}|$. The reason for this behavior is that since $\epsilon'_{r1} = \epsilon'_{r2} = \epsilon'_{r3}$, the three section lossy electro-material line behaves like a single transmission line equal in length to the three cascaded transmission lines. If three different cases are defined such that sum of $\tan \delta_{1,2,3}$ remains equal in all the three cases, the response cannot be differentiated in terms of Γ_{in} . In terms of wave propagation, this is equal to three identical transmission lines with $\epsilon'_r = 3.5$ and $\tan \delta = \tan \delta_{sum}$. This also means that in a lossy electro-material line with $\epsilon_{r1} = \epsilon_{r2} = \epsilon_{r3} = \dots = \epsilon_{rn}$, the distinct loss tangents of each segment cannot be estimated correctly. However, $\tan \delta_{sum}$, as defined in Eq. 75, can be detected quite accurately. This result is also explained and verified using an ANN in the forthcoming sections.

7.2.4 Case 4 : Varying $\tan \delta_1$, $\tan \delta_2$ and $\tan \delta_3$ with $\epsilon'_{r1} \neq \epsilon'_{r2} \neq \epsilon'_{r3}$

In the fourth scenario, $\tan \delta$ is varied in all the three sections but this time $\epsilon'_{r1} \neq \epsilon'_{r2} \neq \epsilon'_{r3}$. The complete configuration is given by Eq. 76 - Eq. 84:

$$\epsilon'_{r1} \neq \epsilon'_{r2} \neq \epsilon'_{r3} \quad (76)$$

$$\epsilon'_{r1} = 3.5 \quad (77)$$

$$\epsilon'_{r2} = 2 \quad (78)$$

$$\epsilon'_{r3} = 5.5 \quad (79)$$

$$\tan \delta_{1a} = 0.01, \tan \delta_{1b} = 0.2, \tan \delta_{1c} = 0.1 \quad (80)$$

$$\tan \delta_{2a} = 0.2, \tan \delta_{2b} = 0.1, \tan \delta_{2c} = 0.01 \quad (81)$$

$$\tan \delta_{3a} = 0.1, \tan \delta_{3b} = 0.01, \tan \delta_{3c} = 0.2 \quad (82)$$

$$f = 1GHz \rightarrow 6GHz \quad (83)$$

$$\Delta f = 100MHz \quad (84)$$

The magnitude and phase of Γ_{in} of a lossy electro-material line with $\epsilon'_{r1} \neq \epsilon'_{r2} \neq \epsilon'_{r3}$ and varying $\tan \delta_{1,2,3}$ are shown in Fig. 68 and Fig. 69, respectively. Three different combinations of $\tan \delta_{1,2,3}$ are used as highlighted in Eq. 76 - Eq. 84.

From the $|\Gamma_{in}|$ and $\angle \Gamma_{in}$ plots in Fig. 68 and Fig. 69, it can be observed that for a lossy electro-material line with $\epsilon'_{r1} \neq \epsilon'_{r2} \neq \epsilon'_{r3}$, the $|\Gamma_{in}|$ varies for different combinations of $\tan \delta_{1,2,3}$. A small shift in resonant frequency is also observed. In terms of $\angle \Gamma_{in}$, the change in response gets slightly pronounced for higher frequencies. Although $\angle \Gamma_{in}$ contains some information about $\tan \delta$, the resonant frequency and $|\Gamma_{in}|$ contains the major part of it.

7.3 Neural Networks for a Lossy Electro-material Line

To reconstruct permittivity profile of a lossy electro-material line, a neural network with the Levenberg Marquardt backpropagation algorithm is used based on the analysis reported in [50]. The training data structure is of prime importance in this setup. Based on the 4 cases presented above, the neural network architecture will comprise two subnetworks, one solving for the real part of permittivity, ϵ'_r , and the second

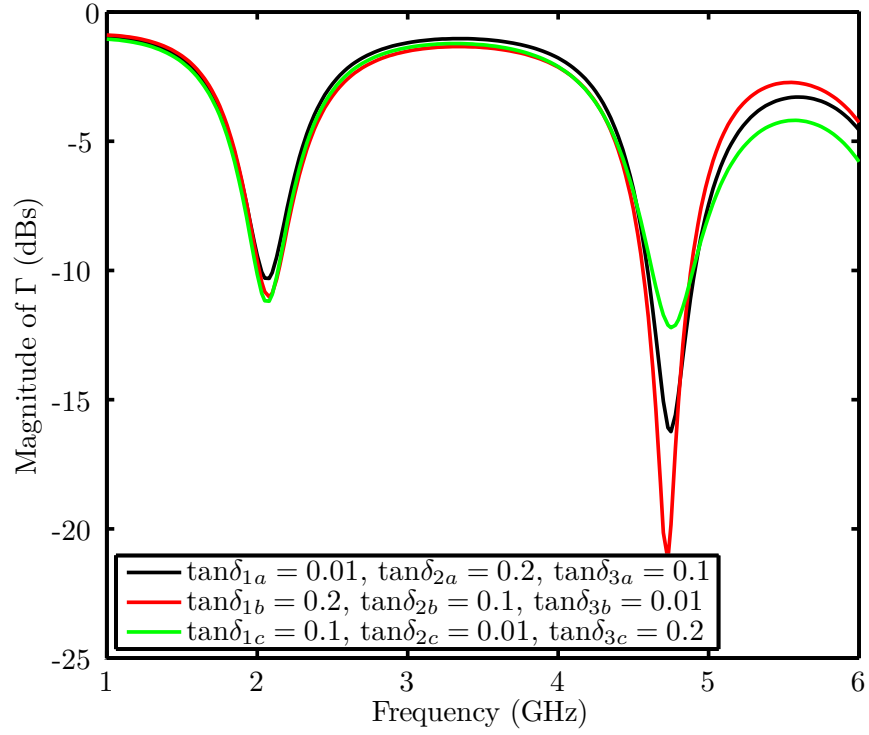


Figure 68: $|\Gamma_{in}|$ for three section lossy electro-material line with $\epsilon'_{r1} \neq \epsilon'_{r2} \neq \epsilon'_{r3}$, while varying $\tan\delta_{1,2,3}$. To demonstrate the effect of varying $\tan\delta$, three different combinations of $\tan\delta_{1,2,3}$ are used as highlighted in Eq. 84 - Eq. 76.

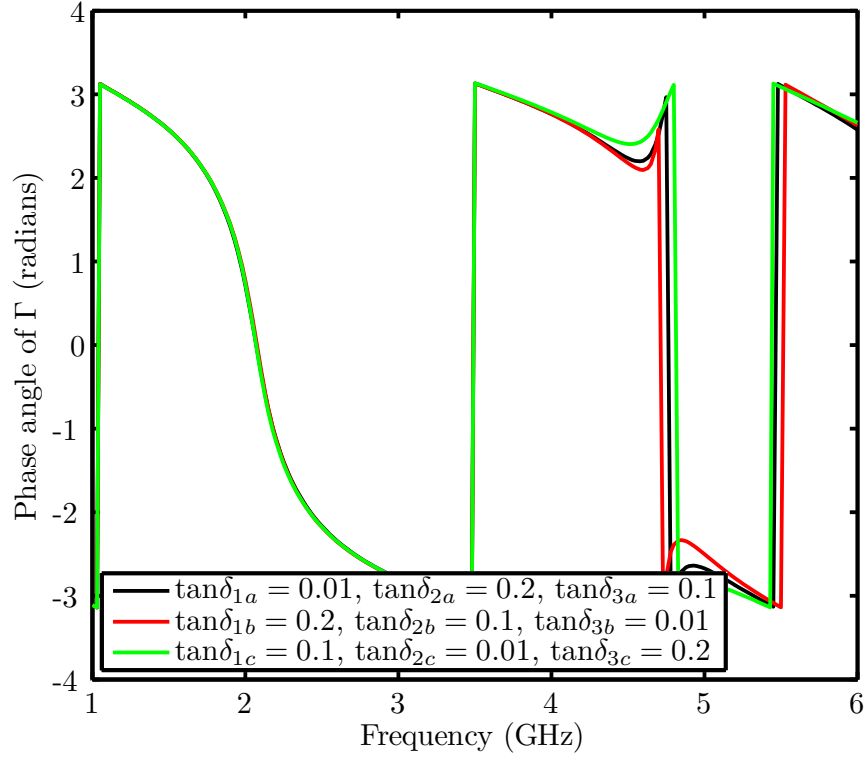


Figure 69: Phase of Γ_{in} for three section lossy electro-material line with $\epsilon'_{r1} \neq \epsilon'_{r2} \neq \epsilon'_{r3}$, while varying $\tan \delta_{1,2,3}$. To demonstrate the effect of varying $\tan \delta$, three different combinations of $\tan \delta_{1,2,3}$ are used as highlighted in Eq. 84 - Eq. 76.

one for $\tan \delta$. Instead of dividing the complex permittivity into real and imaginary part as demonstrated in [61], to reconstruct the complex permittivity for a stratified medium, ϵ'_r and $\tan \delta$ are used. The reason for using $\tan \delta$ is for the ease of interpreting permittivity in terms of lossiness of the electro-material line, which is an important parameter for a passive RFID based sensor.

The training data used to train the neural network using the Levenberg Marquardt(LM) backpropagation algorithm, consist of the phase and magnitude of Γ_{in} of the three section lossy electro-material line, as the permittivity of the line sections is varied. Each data set comprise 27,000 training vectors covering the complete range of complex permittivity in the three sections of the lossy electro-material line. The dimensions of the resultant training data set are 27000×16 , where 16 corresponds to the frequency range from 3.25 GHz to 4.75 GHz with $\Delta f = 100 MHz$. When both the magnitude and phase are required to reconstruct the permittivity profile, the data matrices are cascaded together as shown in Eq. 46.

In case of a lossless electro-material line with n segments and with m possible values of ϵ'_r with in each segment, the number of vectors generated for the training data is given by $NN = m^n$. The length of vectors is determined by the frequency range of interest and frequency step size. If the frequency is swept from f_1 to f_2 with a step size of Δf , then the length of each vector will be $L = (f_2 - f_1)/\Delta f$. The size of D as shown in Eq. 46 will be $NN \times 2L$. For a lossy electro-material line, the size of the training data matrix will increase depending upon the range and resolution of $\tan \delta$. For g possible values of $\tan \delta$ in each bin, the number of vectors would be $\widetilde{NN} = (g \times m)^n$. While reconstructing ϵ'_r or $\tan \delta$, the resolution is not limited to m or g respectively. However, given the non-linear nature of this problem, accuracy of results can become questionable beyond the range for which the network was trained.

With a large size training data matrix, LM requires storage of quite a large matrix. The size of the Jacobian is $Q \times nn$, where Q is the number of training sets and nn

is the number of weights and biases. To handle this problem of large matrix size, the Jacobian can be divided into equal sub matrices as shown in Eq. 35.

To develop a method using an ANN to reconstruct the spatially distributed complex permittivity profile, two simpler scenarios of lossy electro-material line are studied:

7.3.1 Lossy electro-material line with $\epsilon'_{r1} = \epsilon'_{r2} = \epsilon'_{r3}$

This is a simple scenario, similar to *Case 3*, in which $\tan \delta_1, \tan \delta_2$ and $\tan \delta_3$ are varied while $\epsilon'_{r1} = \epsilon'_{r2} = \epsilon'_{r3}$ for a three section lossy electro-material line. As ϵ'_r is fixed and not varying in any of the segment of transmission line, we will focus only on back solving the $\tan \delta$. The training data was generated for three section microstrip line, with the configuration is given by Eq. 85 - Eq. 88:

$$\epsilon'_{r1} = \epsilon'_{r2} = \epsilon'_{r3} = 2.4 \quad (85)$$

$$0.01 \leq \tan \delta_{1,2,3} \leq 0.3 \quad (86)$$

$$f = 3.25GHz \rightarrow 4.75GHz \quad (87)$$

$$\Delta f = 100MHz \quad (88)$$

As already discussed in *case 3*, there is negligible information in the phase of Γ_{in} when only $\tan \delta$ is varied. Therefore, only $|\Gamma|$ is used for training the network and the data matrix structure is given by Eq. 89.

$$D = [|\Gamma|] \quad (89)$$

For the specific parameters, the dimensions of the resultant training data set are 27000×16 , where 16 corresponds to the frequency range from 3.25 GHz to 4.75 GHz with $\Delta f = 100MHz$. The size of frequency step, determining the length of the vector, is selected based on the results presented in [50]. The dimensions of the three

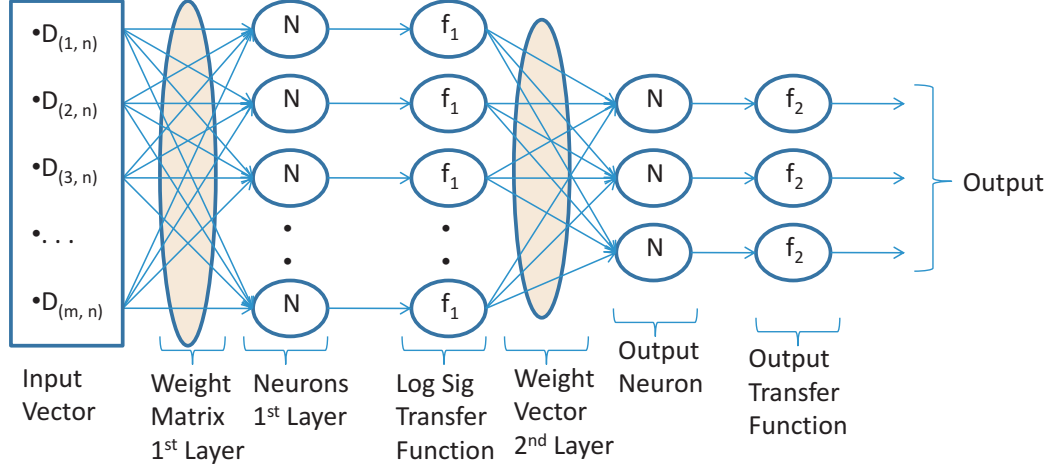


Figure 70: A neural network with one hidden layer and three output neurons.

transmission lines are given in Table 12. The neural network architecture with one hidden layer and 3 output neurons is shown in Fig. 70.

Table 12: Dimensions of the microstrip transmission lines used for lossy electro-material line

	Trans Line 1	Trans Line 2	Trans Line 3
Length (L)	1.25 cm	1.25 cm	1.25 cm
Width (W)	0.5 cm	0.5 cm	0.5 cm
Substrate Height	0.127 cm	0.127 cm	0.127 cm
Conductor Thickness	0.0017 cm	0.0017 cm	0.0017 cm
Loss Tangent	$\tan \delta_1$	$\tan \delta_2$	$\tan \delta_3$
Dielectric Constant (ϵ'_r)	2.4	2.4	2.4

Different networks were tested with 15, 20, 25, 30 and 35 neurons in the hidden layer of the ANN using the backpropagation LM algorithm. Before commenting on the accuracy of the models in terms of neuron architecture, the results from networks with 20 and 35 neurons in the hidden layer are shown in Tables 13 and 14. In each table, results for three different cases of lossy electro-material line, *A*, *B*, and *C* are shown in terms of the actual and estimated value for each section.

As $\epsilon'_{r1} = \epsilon'_{r2} = \epsilon'_{r3} = 2.4$, the results are focused only on $\tan \delta$. The estimated value of loss tangent is denoted by $\widetilde{\tan \delta}$, and $\sum \tan \delta$ denotes the sum of actual / estimated values of loss tangent in all the bins of lossy electro-material line.

It can be observed for both networks, with 20 neurons and 35 neurons in the hidden layer, that the distinct values of $\tan \delta$ could not be estimated with reasonable accuracy. However, an interesting result was observed that in terms of $\sum \tan \delta$ the estimated value is very close to the actual value with an error less than 4%. It can be concluded based on the results shown in Tables 13 and 14, that in the case when ϵ'_r is the same for all sections of the line, the distinct values of $\tan \delta$ for each section of the lossy electro-material line cannot be estimated accurately. However, the sum of loss tangents can be very accurately estimated. With $\epsilon'_{r1} = \epsilon'_{r2} = \epsilon'_{r3}$, the three section electro-material line can be viewed as a single section lossy electro-material line, with inhomogeneous $\tan \delta$. Although individual values of $\tan \delta_{1,2,3}$ cannot be estimated, the sum of actual values of $\tan \delta_{1,2,3}$, which is the total loss across the complete electro-material line, can be estimated very accurately.

Table 13: Results for estimating $\tan \delta_{1,2,3}$ using neural networks with 20 neurons in the hidden layer for a lossy electro-material line with $\epsilon'_{r1,2,3} = 2.4$.

	$\tan \delta_1$	$\tan \delta_2$	$\tan \delta_3$	$\sum \tan \delta$
Actual-A ($\tan \delta$)	0.03	0.15	0.25	0.43
Estimated-A ($\tan \delta$)	0.1107	0.1768	0.1466	0.4341
Actual-B ($\tan \delta$)	0.26	0.1	0.06	0.42
Estimated-B ($\tan \delta$)	0.108	0.1771	0.1472	0.4324
Actual-C ($\tan \delta$)	0.04	0.28	0.13	0.45
Estimated-C ($\tan \delta$)	0.1111	0.1764	0.1463	0.4328

Table 14: Results for estimating $\tan \delta_{1,2,3}$ using neural networks with 35 neurons in the hidden layer for a lossy electro-material line with $\epsilon'_{r1,2,3} = 2.4$.

	$\tan \delta_1$	$\tan \delta_2$	$\tan \delta_3$	$\sum \tan \delta$
Actual-A ($\tan \delta$)	0.03	0.15	0.25	0.43
Estimated-A ($\tan \delta$)	0.1101	0.1758	0.1470	0.4329
Actual-B ($\tan \delta$)	0.26	0.1	0.06	0.42
Estimated-B ($\tan \delta$)	0.1092	0.1753	0.1457	0.4302
Actual-C ($\tan \delta$)	0.04	0.28	0.13	0.45
Estimated-C ($\tan \delta$)	0.1106	0.1764	0.1466	0.433

$$\sum \tan \delta = \tan \delta_1 + \tan \delta_2 + \tan \delta_3 \approx \widetilde{\tan} \delta_1 + \widetilde{\tan} \delta_2 + \widetilde{\tan} \delta_3 \quad (90)$$

In this scenario only $\tan \delta_{1,2,3}$ was being tracked and therefore the network comprised of a single network with one hidden layer. The main idea of presenting this scenario was to highlight the limitation that if the real part of permittivity (ϵ'_r) is same, then the total $\tan \delta$ can be estimated but the loss in each bin cannot be distinguished correctly.

7.3.2 Lossy electro-material line with $\epsilon'_{r1} \neq \epsilon'_{r2} \neq \epsilon'_{r3}$

In this scenario, the lossy electro-material line is configured such that the three bins are set at three different values of ϵ'_r while $\tan \delta$ is varied in each segment. To overcome the problem highlighted in the previous section, the lossy electro-material line under test is configured such that $\epsilon'_{r1} = 2.4$, $\epsilon'_{r2} = 4.4$, and $\epsilon'_{r3} = 6.6$. To simplify the problem, $\epsilon'_{r1,2,3}$ are fixed while $\tan \delta_{1,2,3}$ are varied across a range from 0.01 to 0.3. ($0.01 \leq \tan \delta_{1,2,3} \leq 0.3$), with a step size ($\Delta \tan \delta$) of 0.01. The frequency is swept over a range of 3.25 to 4.75 GHz with a step size (Δf) of 100 MHz. In this particular situation, as ϵ'_r is fixed to distinct values in each segment and not varying, we will keep the focus on backsolving $\tan \delta_{1,2,3}$. Sufficient information about $\tan \delta$ is contained in $|\Gamma|$, and thus the data set is arranged in the format given by Eq. 89.

The network was trained using the Levenberg Marquardt backpropagation algorithm and the network was then tested with different numbers of neurons in the hidden layer. Quite accurate results were obtained with 20 to 30 neurons in the hidden layer with a logsigmoidal transfer function. The results for estimating $\tan \delta$ using neural networks with 20 neurons and 30 neurons in the hidden layer are shown in Tables 15 and 16, respectively.

It can be observed that the complex permittivity of a lossy electro-material line can be accurately reconstructed using neural networks with the Levenberg Marquardt

Table 15: Results for estimating $\tan \delta_{1,2,3}$ using neural networks with 20 neurons in hidden layer for a lossy electro-material line with $\epsilon'_{r1} = 2.4$, $\epsilon'_{r2} = 4.4$, and $\epsilon'_{r3} = 6.6$.

	$\epsilon'_{r1} = 2.4$	$\epsilon'_{r2} = 4.4$	$\epsilon'_{r3} = 6.6$	
	$\tan \delta_1$	$\tan \delta_1$	$\tan \delta_3$	error
Actual-A ($\tan \delta$)	0.03	0.26	0.04	
Estimated-A ($\widetilde{\tan \delta}$)	0.03	0.26	0.04	0%
Actual-B ($\tan \delta$)	0.15	0.1	0.28	
Estimated-B ($\widetilde{\tan \delta}$)	0.15	0.1	0.28	0%
Actual-C ($\tan \delta$)	0.25	0.06	0.13	
Estimated-C ($\widetilde{\tan \delta}$)	0.25	0.06	0.13	0%

Table 16: Results for estimating $\tan \delta_{1,2,3}$ using neural networks with 30 neurons in hidden layer for a lossy electro-material line with $\epsilon'_{r1} = 2.4$, $\epsilon'_{r2} = 4.4$, and $\epsilon'_{r3} = 6.6$.

	$\epsilon'_{r1} = 2.4$	$\epsilon'_{r2} = 4.4$	$\epsilon'_{r3} = 6.6$	
	$\tan \delta_1$	$\tan \delta_1$	$\tan \delta_3$	error
Actual-A ($\tan \delta$)	0.03	0.26	0.04	
Estimated-A ($\widetilde{\tan \delta}$)	0.03	0.26	0.04	0%
Actual-B ($\tan \delta$)	0.15	0.1	0.28	
Estimated-B ($\widetilde{\tan \delta}$)	0.15	0.1	0.28	0%
Actual-C ($\tan \delta$)	0.25	0.06	0.13	
Estimated-C ($\widetilde{\tan \delta}$)	0.25	0.06	0.13	0%

backpropagation algorithm. However, this model was limited in two aspects: a) it was tested with noise free data, and b) $\epsilon_{r1,2,3}$ were not varied and were fixed to a single value.

The performance of this model in presence of measurement noise is tested by adding white Guassian noise to the training and testing data. The results of reconstructing complex permittivity using a network with one hidden layer of 20 neurons in the presence of white Guassian noise with 10dB SNR are shown in Table. 17.

Table 17: Results for estimating $\tan \delta_{1,2,3}$ using neural networks with 20 neurons in hidden layer for a lossy electro-material line with $\epsilon'_{r1} = 2.4$, $\epsilon'_{r2} = 4.4$, and $\epsilon'_{r3} = 6.6$, in presence of white Gaussian noise with 10 dB SNR.

	$\epsilon'_{r1} = 2.4$	$\epsilon'_{r2} = 4.4$	$\epsilon'_{r3} = 6.6$	
	$\tan \delta_1$	$\tan \delta_2$	$\tan \delta_3$	Avg % error
Actual-A ($\tan \delta$)	0.03	0.26	0.04	
Estimated-A ($\tan \delta$)	0.0379	0.2596	0.0348	
% error	26.3%	0.15%	13%	13.15%
Actual-B ($\tan \delta$)	0.15	0.1	0.28	
Estimated-B ($\tan \delta$)	0.1438	0.1073	0.2774	
% error	4.13%	7.3%	0.93%	4.12%
Actual-C ($\tan \delta$)	0.25	0.06	0.13	
Estimated-C ($\tan \delta$)	0.254	0.0451	0.1370	
% error	1.6%	24.83%	5.38%	10.6%

The results show that the average % error is less than 14% in any of the three test cases. The results are accurate with an error less than 7.5%, except for the three situations where the % errors soared to 26.3%, 24.8%, and 13.0%. The absolute errors in these three estimated values were 0.0079 , 0.0073 and 0.0052 respectively. In all these three cases the absolute error was not too high and the high % error can be attributed to the small target value of $\tan \delta$.

In the next section, the complete model to solve a lossy electro-material line is presented, in which $\epsilon'_{r1,2,3}$ are also varied along with $\tan \delta_{1,2,3}$ in each section of the electro-material line.

7.4 Reconstructing spatially distributed ϵ'_r and $\tan \delta$

In this section, an ANN is employed to reconstruct the spatially distributed permittivity profile of a three section lossy electro-material line. ϵ'_r is varied along with $\tan \delta$ in all the three bins. The parameters for the electro-material line model along with the frequency range are given by Eq. 91 - Eq. 100:

$$3.5 \leq \epsilon'_{r1} \leq 4.0 \quad (91)$$

$$2.5 \leq \epsilon'_{r2} \leq 3.0 \quad (92)$$

$$4.5 \leq \epsilon'_{r3} \leq 5.0 \quad (93)$$

$$\Delta \epsilon'_{r1} = \Delta \epsilon'_{r2} = \Delta \epsilon'_{r3} = 0.13 \quad (94)$$

$$0.0 \leq \tan \delta_1 \leq 0.1 \quad (95)$$

$$0.0 \leq \tan \delta_2 \leq 0.1 \quad (96)$$

$$0.0 \leq \tan \delta_3 \leq 0.1 \quad (97)$$

$$\Delta \tan \delta_1 = \Delta \tan \delta_2 = \Delta \tan \delta_3 = 0.012 \quad (98)$$

$$f = 4GHz \rightarrow 5.5GHz \quad (99)$$

$$\Delta f = 75MHz \quad (100)$$

The dimensions and the range of electrical properties of the electro-material line are selected such that the resonant frequency falls in the selected frequency range. As ϵ_r varies, the resonant frequency will shift, but it remains in the desired frequency range. The training data is generated using the parameters given in Eq. 91 - Eq. 100.

The complete network for the lossy line comprises two neural networks integrated together as shown in Fig. 71. The real part of permittivity is reconstructed using the methodology demonstrated for the lossless electro-material line. The training data set for ϵ'_r has $|\Gamma|$ and $\angle \Gamma$ (phase) cascaded together in the shape of a matrix given by

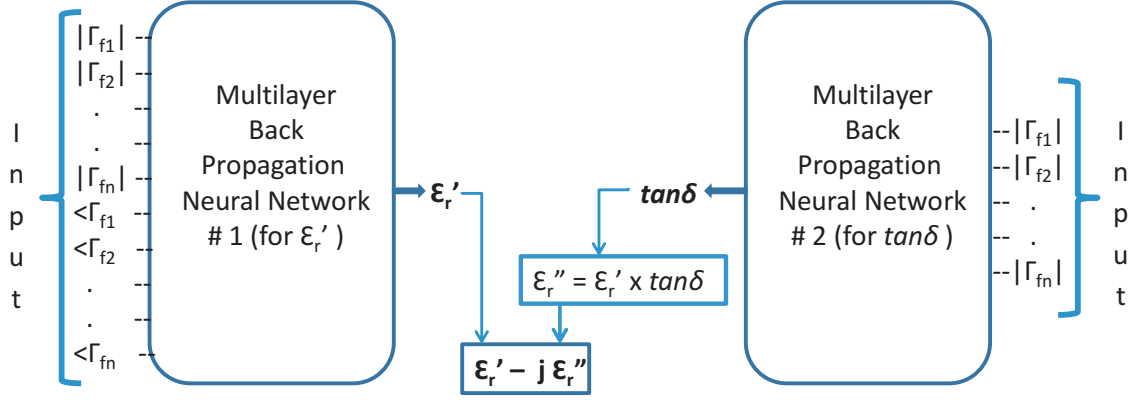


Figure 71: Two neural networks integrated together to backsolve ϵ_r of lossy electro-material line. Network 1 solves for ϵ_r' and network 2 reconstructs the $\tan\delta$.

Eq.46. Owing to the range of $\epsilon_{r1,2,3}'$ and $\tan\delta_{1,2,3}$, the phase of Γ_{in} is linearly scaled to even out the information distribution and increase robustness against measurement noise. As a result the data set D is modified to D_{sc} as given in Eq. 101, where N is the linear scaling factor.

$$D_{sc} = \begin{bmatrix} |\Gamma| \\ N \times \angle \Gamma \end{bmatrix} \quad (101)$$

The data sets, D and D_{sc} are different in structure although they are generated from the lossy electro-material line with similar parameters. Input, training algorithm and architecture of the two networks when integrated to solve for complex permittivity, can be different and in fact are independent from each other. Therefore, for better explanation, the complete method is split into a three step process: 1) reconstructing $\tan\delta$, 2) reconstructing ϵ_r' , and 3) combining the two outputs to reconstruct complex permittivity.

7.4.1 Reconstructing $\tan\delta$

A backpropagation neural network with one hidden layer and three output neurons is used to back-solve the $\tan\delta$ for the three section lossy electro-material line. The

neural network architecture is shown in Fig. 70. Using the Levenberg Marquardt back propagation algorithm, the number of neurons in the hidden layer is determined through an iterative process. The training data is generated with the parameters given in Eq. 91 - Eq. 100. The size of data set for the given parameters is $21 \times 46,656$. To handle the large data set, the Jacobian is divided into 4 equal matrices, J_1 , J_2 , J_3 and J_4 , as given in Eq. 102.

$$H = J^T J = J_1^T J_1 + J_2^T J_2 + J_3^T J_3 + J_4^T J_4 \quad (102)$$

The neural network algorithm was tested for three different electro-material lines. The three configurations along with the initial results of estimating $\tan \delta$ using 20 neurons in the hidden layer are shown in Table 18. The three configurations are identified as *Actual-A*, *Actual-B* and *Actual-C*, while the estimates are denoted by *Estimate-A*, *Estimate-B* and *Estimate-C*.

Table 18: Results for estimating $\tan \delta_{1,2,3}$ using neural networks with 20 neurons in hidden layer for a lossy electro-material line with $3.5 \leq \epsilon'_{r1} \leq 4.0$, $2.5 \leq \epsilon'_{r2} \leq 3.0$, and $4.5 \leq \epsilon'_{r3} \leq 5.0$, for the frequency range of 4.0 - 5.5 GHz with $\Delta f = 75 MHz$.

	ϵ_{r1}	ϵ_{r2}	ϵ_{r3}		
	$\tan \delta_1$	$\tan \delta_2$	$\tan \delta_3$	Avg % error	R
Actual-A ($\tan \delta$)	0.02	0.05	0.1		
Estimate-A ($\widetilde{\tan \delta}$)	0.0223	0.0506	0.0999	% 4.267	0.9991
% error	% 11.500	% 1.200	% 0.100		
Actual-B ($\tan \delta$)	0.05	0.03	0.08		
Estimate-B ($\widetilde{\tan \delta}$)	0.0495	0.0306	0.081	% 1.417	0.9998
% error	% 1.000	% 2.000	% 1.250		
Actual-C ($\tan \delta$)	0.09	0.08	0.03		
Estimate- C ($\widetilde{\tan \delta}$)	0.0883	0.0836	0.0303	% 2.463	0.9995
% error	% 1.889	% 4.500	% 1.000		

The results show that with 20 neurons, the % error remains less than 12%. In terms of % error, the results are quite accurate except for estimate-A for $\tan \delta_1$. This comparatively high error can be attributed to the low target value: $\tan \delta_1 = 0.02$. The network architecture is determined through an iterative process, in which the

network is tested for different combinations of neurons in the hidden layer. Moreover, the performance of algorithms in presence of measurement noise is also tested by adding white Gaussian noise to the training data and the test vectors. The results for $\tan \delta$ estimates using test vectors emulating three different electro-material lines, for different levels of white Gaussian noise for 20 neurons in hidden layer, are shown in Table 19. It can be observed that for all the three electro-material lines, the accuracy improves with SNR of measurement noise. However, for electro-material line A, a higher error is observed for data having gaussian noise with 30 dB SNR. This unexpected increase in error can be attributed to high % error for lowest value of $\tan \delta_1$. A high % error was observed generally for low values of $\tan \delta$.

It can be observed that as the SNR of the added white Gaussian noise is improved, the coefficient of regression ' R ' increases, as shown in Fig. 72.

In terms of *Avg % error*, in all the three electro-material lines under test, the results get more accurate as the SNR of the added noise is improved. However there are two noticeable facts in this regard: 1) there is an increase in the error for $\tan \delta$ estimates for electro-material line A with 25dB SNR of added noise, 2) the first bin in electro-material line A ($\tan \delta_{1A} = 0.02$), the second segment of electro-material line B ($\tan \delta_{2B} = 0.03$), and the third section of electro-material line C ($\tan \delta_{3C} = 0.03$) have the largest % error in all cases.

For the second observation, one of the factors causing this phenomena is the small values of $\tan \delta$. Also it is observed that estimates are more accurate for smaller values in the second bin, as compared to the first and third. The errors are particularly high for smaller values of $\tan \delta$ in the first bin. This fact will be further investigated in the results for other ANN configurations with hidden layers having 25, 30, 35 and 40 neurons. Regarding an increased error with 25dB SNR for electro-material line A, it can be caused by insufficient architecture of the network. This fact will also be investigated while comparing results for different neural network architectures.

Table 19: Results for estimating $\tan \delta_{1,2,3}$ using neural networks with 20 neurons in hidden layer for three different lossy electro-material lines with $3.5 \leq \epsilon'_{r1} \leq 4.0$, $2.5 \leq \epsilon'_{r2} \leq 3.0$, and $4.5 \leq \epsilon'_{r3} \leq 5.0$. The results are presented for the frequency range of 4.0 - 5.5 GHz with $\Delta f = 75 MHz$, in presence of white Guassian noise with 10dB, 15dB, 20dB, 25dB and 30dB SNR. (Est. denotes estimated)

	ϵ'_{r1}	ϵ'_{r2}	ϵ'_{r3}		
	$\tan \delta_1$	$\tan \delta_2$	$\tan \delta_3$	Avg % error	R
Actual-A ($\tan \delta$)	0.02	0.05	0.1		
Est-A ($\widetilde{\tan \delta}$) AWGN 30dB SNR	0.0374	0.0463	0.091		0.8981
% error	87.000	7.400	9.000	34.467	
Est-A ($\widetilde{\tan \delta}$) AWGN 25dB SNR	0.0272	0.0431	0.0987		0.8543
% error	36.000	13.800	1.300	17.033	
Est-A ($\widetilde{\tan \delta}$) AWGN 20dB SNR	0.0305	0.0456	0.0943		0.8041
% error	52.500	8.800	5.700	22.333	
Est-A ($\widetilde{\tan \delta}$) AWGN 15dB SNR	0.0383	0.0525	0.0844		0.7261
% error	91.500	5.000	15.600	37.367	
Est-A ($\widetilde{\tan \delta}$) AWGN 10dB SNR	0.0418	0.0526	0.0814		0.6425
% error	109.000	5.200	18.600	44.267	
Actual-B ($\tan \delta$)	0.05	0.03	0.08		
Est-B ($\widetilde{\tan \delta}$) AWGN 30dB SNR	0.0472	0.0312	0.0828		0.8977
% error	5.600	4.000	3.500	4.367	
Est-B ($\widetilde{\tan \delta}$) AWGN 25dB SNR	0.0381	0.0389	0.0855		0.8563
% error	23.800	29.667	6.875	20.114	
Est-B ($\widetilde{\tan \delta}$) AWGN 20dB SNR	0.0368	0.0454	0.0823		0.8031
% error	26.400	51.333	2.875	26.869	
Est-B ($\widetilde{\tan \delta}$) AWGN 15dB SNR	0.0425	0.056	0.0679		0.7243
% error	15.000	86.667	15.125	38.931	
Est-B ($\widetilde{\tan \delta}$) AWGN 10dB SNR	0.0337	0.0524	0.0795		0.6428
% error	32.600	74.667	0.625	35.964	
Actual-C ($\tan \delta$)	0.09	0.08	0.03		
Est-C ($\widetilde{\tan \delta}$) AWGN 30dB SNR	0.0904	0.0876	0.0283		0.8965
% error	0.444	9.500	5.667	5.204	
Est-C ($\widetilde{\tan \delta}$) AWGN 25dB SNR	0.0916	0.072	0.0351		0.8568
% error	1.778	10.000	17.000	9.593	
Est-C ($\widetilde{\tan \delta}$) AWGN 20dB SNR	0.0859	0.0704	0.0405		0.8036
% error	4.556	12.000	35.000	17.185	
Est-C ($\widetilde{\tan \delta}$) AWGN 15dB SNR	0.0717	0.0705	0.0524		0.7241
% error	20.333	11.875	74.667	35.625	
Est-C ($\widetilde{\tan \delta}$) AWGN 10dB SNR	0.0788	0.064	0.0617		0.6422
% error	12.444	20.000	105.667	46.037	

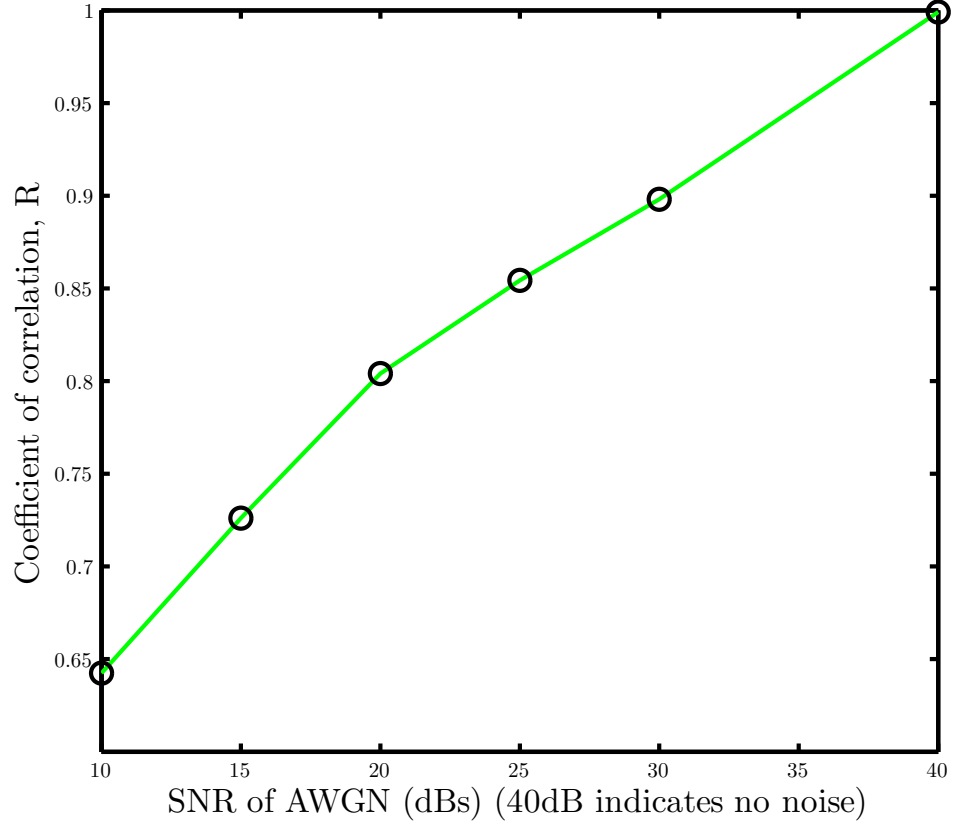


Figure 72: Coefficient of correlation, R , computed for different values of SNR in white Gaussian noise for a neural network with 20 neurons in the hidden layer.

The results for estimating $\tan \delta$ for the set of three, three sectioned electro-material lines, employing 25 neurons in the hidden layer with the LM backpropagation algorithm are shown in Table 20.

Using 25 neurons in the hidden layer, the % error in estimated values is less than 3%. The behavior of this network was also tested in presence of white Gaussian noise with 10, 15, 20, 25 and 30 dB SNR, and the results are tabulated in Table 21.

In the presence of noise, the % error in the $\tan \delta$ estimate reduces as the SNR improves. In this case also, a higher % error can be observed for smaller values of $\tan \delta$.

The results for $\tan \delta$ values of three lossy electro-material lines, using neural networks with 30, 35 and 40 neurons in the hidden layer, are tabulated in Tables 22, 23,

Table 20: Results for estimating $\tan \delta_{1,2,3}$ using neural networks with 25 neurons in hidden layer for a lossy electro-material line with $3.5 \leq \epsilon'_{r1} \leq 4.0$, $2.5 \leq \epsilon'_{r2} \leq 3.0$, and $4.5 \leq \epsilon'_{r3} \leq 5.0$, for the frequency range of 4.0 - 5.5 GHz with $\Delta f = 75 MHz$.

	ϵ'_{r1}	ϵ'_{r2}	ϵ'_{r3}		
	$\tan \delta_1$	$\tan \delta_2$	$\tan \delta_3$	Avg % error	R
Actual-A ($\tan \delta$)	0.02	0.05	0.1		
Estimate-A ($\tan \delta$)	0.0205	0.0502	0.1007	% 1.200	0.9997
% error	% 2.500	% 0.400	% 0.700		
Actual-B ($\tan \delta$)	0.05	0.03	0.08		
Estimate-B ($\tan \delta$)	0.0498	0.0306	0.0803	% 0.925	0.9966
% error	% 0.400	% 2.000	% 0.375		
Actual-C ($\tan \delta$)	0.09	0.08	0.03		
Estimate- C ($\tan \delta$)	0.0896	0.0814	0.0302	% 0.954	0.9997
% error	% 0.444	% 1.750	% 0.667		

and 24, respectively.

It can be observed that there is higher % error for smaller values of $\tan \delta$ as compared to the larger values, and one possible reason is the small target value of $\tan \delta$ itself. The networks with 30 and 35 neurons give the best results for added white Gaussian noise with 20, 25 and 30 dB SNR. Using an ANN with 30 neurons in the hidden layer, $\tan \delta$ can be reconstructed with an average % error less than 20% for added noise having SNR greater than 25dB.

7.4.2 Reconstructing ϵ'_r

The proposed method for reconstructing ϵ'_r of a dissipative electro-material line is quite similar to the approach presented in Chapter IV. The main difference is that in the results presented here, the neural network is trained for lossy electro-material line, while in the previous work, we used the lossless electro-material line to generate the training data. To reconstruct spatially distributed ϵ'_r of an electro-material line with multiple segments, the information is embedded in both the phase and magnitude of Γ_{in} [50]. The training data set for ϵ'_r has $|\Gamma|$ and $\angle \Gamma$ (phase) cascaded together in the shape of a matrix given by Eq.101, where N is the linear scaling factor. The neural network architecture is shown in Fig. 70. The training data for the network

Table 21: Results for estimating $\tan \delta_{1,2,3}$ using neural networks with 25 neurons in hidden layer for three different lossy electro-material lines with $3.5 \leq \epsilon'_{r1} \leq 4.0$, $2.5 \leq \epsilon'_{r2} \leq 3.0$, and $4.5 \leq \epsilon'_{r3} \leq 5.0$. The results are presented for the frequency range of 4.0 - 5.5 GHz with $\Delta f = 75 MHz$, in presence of white Gaussian noise with 10dB, 15dB, 20dB, 25dB and 30dB SNR. (Est. denotes estimated)

	ϵ'_{r1}	ϵ'_{r2}	ϵ'_{r3}		
	$\tan \delta_1$	$\tan \delta_2$	$\tan \delta_3$	Avg % error	R
Actual-A ($\tan \delta$)	0.02	0.05	0.1		
Est-A ($\widetilde{\tan \delta}$) AWGN 30dB SNR	0.032	0.0563	0.0858		0.9002
% error	60.000	12.600	14.200	28.933	
Est-A ($\widetilde{\tan \delta}$) AWGN 25dB SNR	0.0392	0.0431	0.0899		0.8584
% error	96.000	13.800	10.100	39.967	
Est-A ($\widetilde{\tan \delta}$) AWGN 20dB SNR	0.0282	0.047	0.0993		0.8015
% error	41.000	6.000	0.700	15.900	
Est-A ($\widetilde{\tan \delta}$) AWGN 15dB SNR	0.0347	0.0524	0.0925		0.7291
% error	73.500	4.800	7.500	28.600	
Est-A ($\widetilde{\tan \delta}$) AWGN 10dB SNR	0.0383	0.0449	0.0695		0.6447
% error	91.500	10.200	30.500	44.067	
Actual-B ($\tan \delta$)	0.05	0.03	0.08		
Est-B ($\widetilde{\tan \delta}$) AWGN 30dB SNR	0.0362	0.0368	0.0858		0.8988
% error	27.600	22.667	7.250	19.172	
Est-B ($\widetilde{\tan \delta}$) AWGN 25dB SNR	0.054	0.0295	0.078		0.8584
% error	8.000	1.667	2.500	4.056	
Est-B ($\widetilde{\tan \delta}$) AWGN 20dB SNR	0.0261	0.0422	0.0893		0.8017
% error	47.800	40.667	11.625	33.364	
Est-B ($\widetilde{\tan \delta}$) AWGN 15dB SNR	0.0243	0.0564	0.0859		0.7279
% error	51.400	88.000	7.375	48.925	
Est-B ($\widetilde{\tan \delta}$) AWGN 10dB SNR	0.046	0.0484	0.0508		0.6423
% error	8.000	61.333	36.500	35.278	
Actual-C ($\tan \delta$)	0.09	0.08	0.03		
Est-C ($\widetilde{\tan \delta}$) AWGN 30dB SNR	0.0821	0.0831	0.0334		0.9003
% error	8.778	3.875	11.333	7.995	
Est-C ($\widetilde{\tan \delta}$) AWGN 25dB SNR	0.0929	0.0697	0.0379		0.8587
% error	3.222	12.875	26.333	14.144	
Est-C ($\widetilde{\tan \delta}$) AWGN 20dB SNR	0.0959	0.0753	0.0295		0.8027
% error	6.556	5.875	1.667	4.699	
Est-C ($\widetilde{\tan \delta}$) AWGN 15dB SNR	0.0786	0.0617	0.0538		0.7283
% error	12.667	22.875	79.333	38.292	
Est-C ($\widetilde{\tan \delta}$) AWGN 10dB SNR	0.0793	0.0722	0.0433		0.6426
% error	11.889	9.750	44.333	21.991	

Table 22: Results for estimating $\tan \delta_{1,2,3}$ using neural networks with 30 neurons in hidden layer for three different lossy electro-material lines with $3.5 \leq \epsilon'_{r1} \leq 4.0$, $2.5 \leq \epsilon'_{r2} \leq 3.0$, and $4.5 \leq \epsilon'_{r3} \leq 5.0$. The results are presented for the frequency range of 4.0 - 5.5 GHz with $\Delta f = 75 MHz$, in presence of white Gaussian noise with 10dB, 15dB, 20dB, 25dB and 30dB SNR. (Est. denotes estimated)

	ϵ'_{r1}	ϵ'_{r2}	ϵ'_{r3}		
	$\tan \delta_1$	$\tan \delta_2$	$\tan \delta_3$	Avg % error	R
Actual-A ($\tan \delta$)	0.02	0.05	0.1		
Est-A ($\tan \delta$) (No Noise)	0.0213	0.0505	0.1006		0.9997
% error	6.500	1.000	0.600	2.700	
Est-A ($\tan \delta$) AWGN 30dB SNR	0.0285	0.0513	0.0936		0.9007
% error	42.500	2.600	6.400	17.167	
Est-A ($\tan \delta$) AWGN 25dB SNR	0.023	0.0507	0.0958		0.8569
% error	15.000	1.400	4.200	6.867	
Est-A ($\tan \delta$) AWGN 20dB SNR	0.0336	0.0499	0.0962		0.8035
% error	68.000	0.200	3.800	24.000	
Est-A ($\tan \delta$) AWGN 15dB SNR	0.0551	0.0552	0.0679		0.7305
% error	175.500	10.400	32.100	72.667	
Actual-B ($\tan \delta$)	0.05	0.03	0.08		
Est-B ($\tan \delta$) (No Noise)	0.0499	0.0307	0.0808		0.9997
% error	0.200	2.333	1.000	1.178	
Est-B ($\tan \delta$) AWGN 30dB SNR	0.0479	0.0304	0.0839		0.9006
% error	4.200	1.333	4.875	3.469	
Est-B ($\tan \delta$) AWGN 25dB SNR	0.0475	0.0294	0.0864		0.8591
% error	5.000	2.000	8.000	5.000	
Est-B ($\tan \delta$) AWGN 20dB SNR	0.0348	0.0452	0.0829		0.8045
% error	30.400	50.667	3.625	28.231	
Est-B ($\tan \delta$) AWGN 15dB SNR	0.0609	0.0428	0.0634		0.7274
% error	21.800	42.667	20.750	28.406	
Actual-C ($\tan \delta$)	0.09	0.08	0.03		
Est- C ($\tan \delta$) (No Noise)	0.0879	0.0823	0.0306		0.9998
% error	2.333	2.875	2.000	2.403	
Est-C ($\tan \delta$) AWGN 30dB SNR	0.0799	0.0904	0.0307		0.9016
% error	11.222	13.000	2.333	8.852	
Est-C ($\tan \delta$) AWGN 25dB SNR	0.0911	0.0813	0.0299		0.859
% error	1.222	1.625	0.333	1.060	
Est-C ($\tan \delta$) AWGN 20dB SNR	0.083	0.0695	0.0436		0.8015
% error	7.778	13.125	45.333	22.079	
Est-C ($\tan \delta$) AWGN 15dB SNR	0.0694	0.0669	0.0586		0.7283
% error	22.889	16.375	95.333	44.866	

Table 23: Results for estimating $\tan \delta_{1,2,3}$ using neural networks with 35 neurons in hidden layer for three different lossy electro-material lines with $3.5 \leq \epsilon'_{r1} \leq 4.0$, $2.5 \leq \epsilon'_{r2} \leq 3.0$, and $4.5 \leq \epsilon'_{r3} \leq 5.0$. The results are presented for the frequency range of 4.0 - 5.5 GHz with $\Delta f = 75 MHz$, in presence of white Gaussian noise with 15dB, 20dB, 25dB and 30dB SNR. (Est. denotes estimated)

	ϵ'_{r1}	ϵ'_{r2}	ϵ'_{r3}		
	$\tan \delta_1$	$\tan \delta_2$	$\tan \delta_3$	Avg % error	R
Actual-A ($\tan \delta$)	0.02	0.05	0.1		
Est-A ($\widetilde{\tan \delta}$) AWGN 30dB SNR	0.03	0.0503	0.0938		0.9012
% error	50.000	0.600	6.200	18.933	
Est-A ($\widetilde{\tan \delta}$) AWGN 25dB SNR	0.0298	0.0505	0.0912		0.8587
% error	49.000	1.000	8.800	19.600	
Est-A ($\widetilde{\tan \delta}$) AWGN 20dB SNR	0.0389	0.0426	0.0925		0.8032
% error	94.500	14.800	7.500	38.933	
Est-A ($\widetilde{\tan \delta}$) AWGN 15dB SNR	0.0469	0.0482	0.08		0.7285
% error	134.500	3.600	20.000	52.700	
Actual-B ($\tan \delta$)	0.05	0.03	0.08		
Est-B ($\widetilde{\tan \delta}$) AWGN 30dB SNR	0.0578	0.0204	0.0825		0.9006
% error	15.600	32.000	3.125	16.908	
Est-B ($\widetilde{\tan \delta}$) AWGN 25dB SNR	0.0573	0.0292	0.0748		0.859
% error	14.600	2.667	6.500	7.922	
Est-B ($\widetilde{\tan \delta}$) AWGN 20dB SNR	0.0369	0.0502	0.078		0.8043
% error	26.200	67.333	2.500	32.011	
Est-B ($\widetilde{\tan \delta}$) AWGN 15dB SNR	0.0346	0.0461	0.0808		0.7278
% error	30.800	53.667	1.000	28.489	
Actual-C ($\tan \delta$)	0.09	0.08	0.03		
Est-C ($\widetilde{\tan \delta}$) AWGN 30dB SNR	0.0834	0.1008	0.0213		0.8991
% error	7.333	26.000	29.000	20.778	
Est-C ($\widetilde{\tan \delta}$) AWGN 25dB SNR	0.0829	0.0848	0.0365		0.8599
% error	7.889	6.000	21.667	11.852	
Est-C ($\widetilde{\tan \delta}$) AWGN 20dB SNR	0.0884	0.0852	0.0267		0.8005
% error	1.778	6.500	11.000	6.426	
Est-C ($\widetilde{\tan \delta}$) AWGN 15dB SNR	0.0843	0.0677	0.0428		0.7255
% error	6.333	15.375	42.667	21.458	

Table 24: Results for estimating $\tan \delta_{1,2,3}$ using neural networks with 40 neurons in hidden layer for three different lossy electro-material lines with $3.5 \leq \epsilon'_{r1} \leq 4.0$, $2.5 \leq \epsilon'_{r2} \leq 3.0$, and $4.5 \leq \epsilon'_{r3} \leq 5.0$. The results are presented for the frequency range of 4.0 - 5.5 GHz with $\Delta f = 75 MHz$, in presence of white Gaussian noise with 15dB, 20dB, 25dB and 30dB SNR. (Est. denotes estimated)

	ϵ'_{r1}	ϵ'_{r2}	ϵ'_{r3}		
	$\tan \delta_1$	$\tan \delta_2$	$\tan \delta_3$	Avg % error	R
Actual-A ($\tan \delta$)	0.02	0.05	0.1		
Est-A ($\tan \delta$) (No Noise)	0.0205	0.0497	0.1001		0.9998
% error	2.500	0.600	0.100	1.067	
Est-A ($\tan \delta$) AWGN 30dB SNR	0.0295	0.0484	0.0931		0.9013
% error	47.500	3.200	6.900	19.200	
Est-A ($\tan \delta$) AWGN 25dB SNR	0.0314	0.0398	0.1009		0.8591
% error	57.000	20.400	0.900	26.100	
Est-A ($\tan \delta$) AWGN 20dB SNR	0.0456	0.0493	0.0821		0
% error	128.000	1.400	17.900	49.100	
Est-A ($\tan \delta$) AWGN 15dB SNR	0.0405	0.0437	0.0872		0.7291
% error	102.500	12.600	12.800	42.633	
Actual-B ($\tan \delta$)	0.05	0.03	0.08		
Est-B ($\tan \delta$) (No Noise)	0.0502	0.0301	0.08		0
% error	0.400	0.333	0.000	0.244	
Est-B ($\tan \delta$) AWGN 30dB SNR	0.0558	0.025	0.0805		0.9022
% error	11.600	16.667	0.625	9.631	
Est-B ($\tan \delta$) AWGN 25dB SNR	0.0437	0.0388	0.0797		0.859
% error	12.600	29.333	0.375	14.103	
Est-B ($\tan \delta$) AWGN 20dB SNR	0.027	0.0558	0.072		0
% error	46.000	86.000	10.000	47.333	
Est-B ($\tan \delta$) AWGN 15dB SNR	0.0501	0.0474	0.0689		0.7281
% error	0.200	58.000	13.875	24.025	
Actual-C ($\tan \delta$)	0.09	0.08	0.03		
Est- C ($\tan \delta$) (No Noise)	0.0899	0.08	0.0302		0
% error	0.111	0.000	0.667	0.259	
Est-C ($\tan \delta$) AWGN 30dB SNR	0.0908	0.0791	0.0298		0.9012
% error	0.889	1.125	0.667	0.894	
Est-C ($\tan \delta$) AWGN 25dB SNR	0.0835	0.0896	0.0291		0.8587
% error	7.222	12.000	3.000	7.407	
Est-C ($\tan \delta$) AWGN 20dB SNR	0.1	0.072	0.0287		0
% error	11.111	10.000	4.333	8.481	
Est-C ($\tan \delta$) AWGN 15dB SNR	0.0728	0.0683	0.0537		0.7286
% error	19.111	14.625	79.000	37.579	

to backsolve ϵ'_r is generated for the lossy electro-material line with parameters given in Eq. 91 - Eq. 100. The size of data set D_{sc} for the given parameters is $42 \times 46,656$. The large data set is handled by dividing the Jacobian into 4 equal matrices, J_1 , J_2 , J_3 and J_4 , as given in Eq. 102.

A network architecture for the LM back propagation algorithm was determined through an iterative process. The results for reconstructing ϵ'_r using 20 neurons in the hidden layer for three different lossy electro-material lines, A , B and C , with three sections each, are shown in Table 25.

Table 25: Results for estimating $\epsilon'_{r1,2,3}$ using neural networks with 20 neurons in hidden layer for three different lossy electro-material lines with $0.01 \leq \tan \delta_{1,2,3} \leq 0.10$. The results are presented for the frequency range of 4.0 - 5.5 GHz with $\Delta f = 75MHz$. (Est. denotes estimated)

	$\tan \delta_1$	$\tan \delta_2$	$\tan \delta_3$		
	ϵ'_{r1}	ϵ'_{r2}	ϵ'_{r3}	Avg % error	R
Actual-A (ϵ'_r)	3.5	2.9	4.7		
Est-A (ϵ'_r)	3.49	2.89	4.7002	% 0.212	1
% error	% 0.286	% 0.345	% 0.004		
Actual-B (ϵ'_r)	3.7	2.6	4.96		
Est-B (ϵ'_r)	3.7	2.6	4.959	% 0.007	1
% error	% 0.000	% 0.000	% 0.020		
Actual-C (ϵ'_r)	3.9	2.75	4.53		
Est-C (ϵ'_r)	3.9004	2.7502	4.5298	% 0.007	1
% error	% 0.010	% 0.007	% 0.004		

Very accurate results with error less than 1% are achieved with 20 neurons in the hidden layer as shown in Table 25. The network is evaluated for robustness in the presence of measurement noise. The results in the presence of AWGN with 20, 15 and 10dB SNR are shown in Table 26.

The network achieves quite accurate results in the presence of measurement noise, with an error less than 4%. The method is tested for networks with hidden layers having 25 and 30 neurons and the results are tabulated in Table 27 and Table 28, respectively.

Table 26: Results for estimating $\epsilon'_{r1,2,3}$ using neural networks with 20 neurons in hidden layer for three different lossy electro-material lines with $0.01 \leq \tan \delta_{1,2,3} \leq 0.10$. The results are presented for the frequency range of 4.0 - 5.5 GHz with $\Delta f = 75 MHz$, in presence of white Gaussian noise with 10dB, 15dB, and 20dB SNR. (Est. denotes estimated)

	$\tan \delta_1$	$\tan \delta_2$	$\tan \delta_3$		
	ϵ_{r1}	ϵ_{r2}	ϵ_{r3}	Avg % error	R
Actual-A (ϵ'_r)	3.5	2.9	4.7		
Est-A ($\widetilde{\epsilon'_r}$) AWGN 20dB SNR	3.431	2.873	4.8124		0.9129
% error	% 1.971	% 0.931	% 2.391	% 1.765	
Est-A ($\widetilde{\epsilon'_r}$) AWGN 15dB SNR	3.478	2.8953	4.6952		0.8578
% error	% 0.629	% 0.162	% 0.102	% 0.298	
Est-A ($\widetilde{\epsilon'_r}$) AWGN 10dB SNR	3.4827	2.8832	4.7359		0.7956
% error	% 0.494	% 0.579	% 0.764	% 0.612	
Actual-B (ϵ'_r)	3.7	2.6	4.96		
Est-B ($\widetilde{\epsilon'_r}$) AWGN 20dB SNR	3.7528	2.6353	4.8177		0.9135
% error	% 1.427	% 1.358	% 2.869	% 1.885	
Est-B ($\widetilde{\epsilon'_r}$) AWGN 15dB SNR	3.8162	2.6198	4.8067		0.8615
% error	% 3.141	% 0.762	% 3.091	% 2.331	
Est-B ($\widetilde{\epsilon'_r}$) AWGN 10dB SNR	3.7201	2.6681	4.7705		0.7962
% error	% 0.543	% 2.619	% 3.821	% 2.328	
Actual-C (ϵ'_r)	3.9	2.75	4.53		
Est-C ($\widetilde{\epsilon'_r}$) AWGN 20dB SNR	3.8468	2.7297	4.6376		0.9093
% error	% 1.364	% 0.738	% 2.375	% 1.493	
Est-C ($\widetilde{\epsilon'_r}$) AWGN 15dB SNR	3.819	2.7345	4.6467		0.8629
% error	% 2.077	% 0.564	% 2.576	% 1.739	
Est-C ($\widetilde{\epsilon'_r}$) AWGN 10dB SNR	3.8353	2.7374	4.6811		0.795
% error	% 1.659	% 0.458	% 3.336	% 1.818	

Table 27: Results for estimating $\epsilon'_{r1,2,3}$ using neural networks with 25 neurons in hidden layer for three different lossy electro-material lines with $0.01 \leq \tan \delta_{1,2,3} \leq 0.10$. The results are presented for the frequency range of 4.0 - 5.5 GHz with $\Delta f = 75MHz$, in presence of white Gaussian noise with 10dB, 15dB, and 20dB SNR. (Est. denotes estimated)

	$\tan \delta_1$	$\tan \delta_2$	$\tan \delta_3$		
	ϵ'_{r1}	ϵ'_{r2}	ϵ'_{r3}	Avg % error	R
Actual-A (ϵ'_r)	3.5	2.9	4.7		
Est-A (ϵ'_r) (No Noise)	3.5	2.9	4.7		0
% error	% 0	% 0	% 0	% 0	
Est-A (ϵ'_r) AWGN 20dB SNR	3.5	2.909	4.653		0.9164
% error	% 0.000	% 0.310	% 1.000	% 0.437	
Est-A (ϵ'_r) AWGN 15dB SNR	3.5307	2.8748	4.7154		0.8652
% error	% 0.877	% 0.869	% 0.328	% 0.691	
Est-A (ϵ'_r) AWGN 10dB SNR	3.5087	2.8505	4.7558		0.7991
% error	% 0.249	% 1.707	% 1.187	% 1.048	
Actual-B (ϵ'_r)	3.7	2.6	4.96		
Est-B (ϵ'_r) (No Noise)	3.7	2.6	4.96		0
% error	% 0	% 0	% 0	% 0	
Est-B (ϵ'_r) AWGN 20dB SNR	3.77	2.617	4.839		0.9164
% error	% 1.892	% 0.654	% 2.440	% 1.662	
Est-B (ϵ'_r) AWGN 15dB SNR	3.857	2.6564	4.6716		0.8667
% error	% 4.243	% 2.169	% 5.815	% 4.076	
Est-B (ϵ'_r) AWGN 10dB SNR	3.7261	2.6558	4.8011		0.7968
% error	% 0.705	% 2.146	% 3.204	% 2.018	
Actual-C (ϵ'_r)	3.9	2.75	4.53		
Est- C (ϵ'_r) (No Noise)	3.9	2.75	4.53		0
% error	% 0	% 0	% 0	% 0	
Est-C (ϵ'_r) AWGN 20dB SNR	3.88	2.7219	4.632		0.9164
% error	% 0.513	% 1.022	% 2.252	% 1.262	
Est-C (ϵ'_r) AWGN 15dB SNR	3.8696	2.7386	4.6218		0.8644
% error	% 0.779	% 0.415	% 2.026	% 1.074	
Est-C (ϵ'_r) AWGN 10dB SNR	3.8824	2.7369	4.6124		0.793
% error	% 0.451	% 0.476	% 1.819	% 0.916	

Table 28: Results for estimating $\epsilon'_{r1,2,3}$ using neural networks with 30 neurons in hidden layer for three different lossy electro-material lines with $0.01 \leq \tan \delta_{1,2,3} \leq 0.10$. The results are presented for the frequency range of 4.0 - 5.5 GHz with $\Delta f = 75 MHz$, in presence of white Gaussian noise with 10 dB, 15 dB, and 20 dB SNR. (Est. denotes estimated)

	$\tan \delta_1$ ϵ'_{r1} 3.5	$\tan \delta_2$ ϵ'_{r2} 2.9	$\tan \delta_3$ ϵ'_{r3} 4.7	Avg % error	R
Actual-A (ϵ'_r)					
Est-A (ϵ'_r) (No Noise)	3.5	2.9	4.699		1
% error	% 0.000	% 0.000	% 0.021	% 0.007	
Est-A (ϵ'_r) AWGN 20dB SNR	3.4988	2.8792	4.7253		0.9308
% error	% 0.034	% 0.717	% 0.538	% 0.430	
Est-A (ϵ'_r) AWGN 15dB SNR	3.5446	2.8838	4.6527		0.8617
% error	% 1.274	% 0.559	% 1.006	% 0.946	
Est-A (ϵ'_r) AWGN 10dB SNR	3.514	2.875	4.694		0.7978
% error	% 0.400	% 0.862	% 0.128	% 0.463	
Actual-B (ϵ'_r)	3.7	2.6	4.96		
Est-B (ϵ'_r) (No Noise)	3.7	2.6	4.9596		1
% error	% 0.000	% 0.000	% 0.008	% 0.003	
Est-B (ϵ'_r) AWGN 20dB SNR	3.7908	2.6436	4.7872		0.9192
% error	% 2.454	% 1.677	% 3.484	% 2.538	
Est-B (ϵ'_r) AWGN 15dB SNR	3.826	2.6572	4.6905		0.868
% error	% 3.405	% 2.200	% 5.433	% 3.680	
Est-B (ϵ'_r) AWGN 10dB SNR	3.721	2.66	4.775		0.7974
% error	% 0.568	% 2.308	% 3.730	% 2.202	
Actual-C (ϵ'_r)	3.9	2.75	4.53		
Est- C (ϵ'_r) (No Noise)	3.9	2.75	4.5291		1
% error	% 0.000	% 0.000	% 0.020	% 0.007	
Est-C (ϵ'_r) AWGN 20dB SNR	3.8616	2.7308	4.6132		0.9178
% error	% 0.985	% 0.698	% 1.837	% 1.173	
Est-C ($\tan \delta$) AWGN 15dB SNR	3.889	2.7272	4.6156		0.8632
% error	% 0.282	% 0.829	% 1.890	% 1.000	
Est-C (ϵ'_r) AWGN 10dB SNR	3.793	2.7364	4.6899		0.7958
% error	% 2.744	% 0.495	% 3.530	% 2.256	

7.4.3 Reconstructing complex $\epsilon_r = \epsilon'_r(1 - j \tan \delta)$

The last step is quite straightforward in which we use the results of the networks back-solving for $\tan \delta$ and ϵ'_r and integrate them together as shown in Fig. 71. From the results presented in Sections 7.4.1 and 7.4.2, the integrated network to back-solve ϵ_r will need 20 and 30 neurons, to reconstruct ϵ'_r and $\tan \delta$, respectively. The algorithm is more robust against measurement noise when reconstructing ϵ'_r as compare to when back-solving $\tan \delta$. The limit is set by the ability to reconstruct $\tan \delta$, since the integrated system can reconstruct ϵ_r with an error less than 4% for ϵ'_r , and an error less than 20% for $\tan \delta$, in presence of measurement noise with 25 dB SNR.

7.5 Discussion

For a three section lossy electro-material line in a REMS sensor, the variations in $|\Gamma_{in}|$ are much more pronounced than the variations in $\angle \Gamma_{in}$ over the frequency range from 3 to 5 GHz. For the systematic processing of training vectors, $\angle \Gamma_{in}$ is scaled using a linear scaling factor. For back-solving the complex permittivity, ϵ_r is split into ϵ'_r and $\tan \delta$, and both variables are tracked using two separate ANNs. The output of the two ANNs is then integrated together to reconstruct the complex ϵ_r . Any variations in ϵ'_r cause a shift in the resonant frequency of the electro-material line and therefore to reconstruct ϵ'_r , information is embedded in both the $|\Gamma_{in}|$ and $\angle \Gamma_{in}$. However, the variations in $\tan \delta$ can be tracked only in the $|\Gamma_{in}|$ with negligible changes in $\angle \Gamma_{in}$. As a result the training data for back-solving $\tan \delta$ consists of $|\Gamma_{in}|$ only.

In case of an electro-material line with $\epsilon'_{r1} = \epsilon'_{r2} = \epsilon'_{r3}$, it is not possible to accurately solve for $\tan \delta_1$, $\tan \delta_2$ or $\tan \delta_3$. However, the overall $\tan \delta$, which is equal to $\tan \delta_1 + \tan \delta_2 + \tan \delta_3$, can be predicted quite accurately.

The training data size for a dissipative electro-material line is manifold larger than the one for lossless line. To handle this large data set the Jacobian is divided into four equal submatrices. ϵ'_r and $\tan \delta$ are back-solved using two separate ANNs, which

are then integrated together to reconstruct complex ϵ_r . The results are more accurate for larger values of $\tan \delta$ as compared to smaller values. Moreover it is also observed that the setup is more robust against noise while solving for ϵ'_r as compared to $\tan \delta$. For ϵ'_r , the results are accurate with an error of less than 4% in presence of white Gaussian noise with 10dB SNR. The $\tan \delta$ results, which set the limit in this case, are accurate within a tolerance of 20% in presence of white Gaussian noise with 25dB SNR.

With these results, an ANN based methodology to reconstruct the spatially distribute permittivity profile of a dissipative electro-material for a REMS sensor is finalized.

CHAPTER VIII

CONCLUSION AND FUTURE WORK

This thesis presents the concept of a passive RFID sensor, using reflected electro-material signatures (REMS). The REMS sensor consists of an antenna attached to a microstrip transmission line, which in turn is routed over one or more sections of variable permittivity electro-material line before being terminated in a load. The material properties of the transmission line will change in response to the change in the environmental conditions, and would be sensed from an electromagnetic wave reflected by the sensor. Any material that has environmental sensitivity to permeability, permittivity, or conductivity may be a candidate for the electro-material line, e.g thermotropic liquid crystal trapped in polymer substrate. All the information about the variable being sensed is embedded in the spatially distributed permittivity profile of the electro-material line.

With the recent advances in material sciences, there is an increased interest in developing passive sensors with capabilities much more than merely sensing a parameter. Examples include structural health monitoring sensors using smart materials, Carbon Fiber Glass Fiber Reinforced Plastic (CFGFRP) for strain sensing, Transformation Induced Plasticity (TRIP) steel for memorizing the peak strain, etc. The REMS sensor concept may also allow for materials that time-record environmental attributes, thus providing a form of chemical memory rather than electrical memory that would achieve a completely passive sensor. The central idea of this research is to reconstruct the spatially distributed permittivity profile of the electro-material line from the reflection coefficient collected over a range of frequencies. The problem of identifying medium properties from waves reflected from a device of this type is a form

of the classical one dimensional inverse scattering problem. For profile inversion in a lossy inhomogeneous media, analytical techniques are difficult to implement in most practical situations. Artificial neural networks (ANN) have been employed across a wide field of applications, and provide an effective and efficient solution to this type of non-linear inverse problem.

There are three main components of an ANN: the training data, training algorithm and the architecture. The electro-material line is emulated by a three section microstrip line formed by cascading three microstrip lines with exactly same physical dimensions but different permittivity profiles. The ANN was trained using the complex reflection coefficient, Γ_{in} , generated for different values of ϵ_{rn} , where n denotes the bin number of the electro-material line. The variations in ϵ_r causes fluctuations in the resonant frequency, and the magnitude and phase of Γ_{in} . The magnitude and phase of complex reflection coefficient are cascaded together in the training data. The LM backpropagation algorithm is best suited to this problem and exhibits superior performance in terms of average error and computation time in comparison to other algorithms. For the lossless sensors, a single neural network was demonstrated to successfully determine the spatially distributed permittivity profile from the Γ_{in} of the electro-material line with 20 neurons in the hidden layer. The model was tested for its robustness in the presence of measurement noise. The spatially distributed ϵ'_r was reconstructed with an average error less than ± 0.5 in the presence of white Gaussian noise with 10 dB SNR. The frequency resolution is an important parameter for the accuracy of results and computational efficiency. It was observed that a frequency step size smaller than 100 MHz does not improve the accuracy of results. Furthermore, for a wide range of frequencies from 1-5 GHz, a frequency resolution of 300MHz is sufficiently dense to keep the results accurate.

The liquid crystal and isopropyl alcohol exhibit a thermo-responsive nature at microwave frequencies and the experimental observations suggest that a temperature

change as small as $2^{\circ}C$ can be detected. The variations in $\tan \delta$ with temperature fluctuations warrant the need of reconstructing complex permittivity to achieve a fully functional REMS sensor. To backsolve complex permittivity using a real valued ANN, two independent networks were integrated together, one solving for ϵ'_r and the other solving for $\tan \delta$. The complex permittivity is reconstructed from the outputs of the two networks. For the initial verification of this method, a model of a monopole probe immersed in the medium under test was used. The magnitude and phase of the complex Γ_{in} of the monopole probe provide the complete information to train the ANN to reconstruct the complex ϵ_r . Scaling $|\Gamma_{in}|$ linearly, facilitated systematic processing of the training data and improved the robustness of the model in the presence of measurement noise. Splitting the complex permittivity into ϵ'_r and $\tan \delta$ provides an effective way of reconstructing a complex valued target using two real valued ANNs integrated together. It is possible to reconstruct complex permittivity in a similar way using only one ANN, however, it results in poor accuracy and increased average error. The obvious reason for this decline in performance is that when one ANN is used to reconstruct complex permittivity, two non-linear inverse problems, which may have some correlation, are being solved by one network. The accuracy of the proposed method improves for larger values of $\tan \delta$.

Another approach to backsolve a complex valued quantity using two real-valued networks is by separating the complex number into real and imaginary parts and then using two separate networks, one dealing with the real part and the other dealing with the imaginary part. However, this approach has limitations such as the loss of correlation between the real and imaginary parts of the complex input data. In fact, there is usually considerable correlation between the real and imaginary parts of the complex data, which cannot be effectively utilized if real and imaginary values of data are manipulated independently.

Finally, a neural network based methodology is presented to reconstruct the spatially distributed permittivity profile of a dissipative electro-material line. To reconstruct complex permittivity, the training data size is much larger than that for the lossless electro-material line. This large data set can be handled by dividing the Jacobian into four or eight equal submatrices. Variations in ϵ'_r cause a shift in the resonant frequency and therefore, like the lossless electro-material line, both the magnitude and the phase of the complex reflection coefficient are required to reconstruct the spatially distributed ϵ'_r . For recreating $\tan \delta$, $|\Gamma_{in}|$ contains sufficient information. For a lossy electro-material line with homogeneous ϵ'_r across the complete length, it is not possible to backsolve distinct $\tan \delta$ values accurately for different bins of the line using an ANN.

Two independent ANNs are integrated to reconstruct the complex permittivity for varying values of ϵ'_r and $\tan \delta$ in each section of an electro-material line. The phase of Γ_{in} is linearly scaled to achieve an even distribution of information in the training data for the ANN solving for ϵ'_r . The robustness of the integrated ANN is tested against measurement noise and the accuracy of results is not compromised in the presence of white Gaussian noise with 25 dB SNR.

This method to reconstruct a spatially distributed permittivity profile can potentially be implemented in any REMS type passive sensor. In the proposed approach, the electro-material line is discretized into a finite number of segments. The complexity of the problem in terms of data handling increases with an increase in the number of bins of the electro-material line. This one dimensional inverse scattering problem would be more challenging to investigate with non deterministic boundaries and for material properties that vary across a greater range.

The proposed implementation currently requires a minimum bandwidth of about 1-2 GHz to accurately estimate the permittivity profile, which eliminates the possibility of using the ISM band at 5.8 GHz. However, passive ultrawide bandwidth (UWB)

RFID systems are under consideration for the next generation RFID [63], and the present research may be practical for such a system.

Proceeding further, an electro-material line may be developed in collaboration with the specialists of material sciences, which will take the proposed research toward the development of a prototype. One of the advantages of an ANN is that all the training is done beforehand and once the system is trained, the real time processing has negligible computational time delay.

APPENDIX A

A COMPARISON BETWEEN NEURAL NETWORKS & MULTIPLE LINEAR REGRESSION ALGORITHMS FOR REMS

ANN and regression analysis can be considered as two widely used estimating / metamodeling techniques. Both of these schemes have their own pros and cons with respect to data generation, training and then estimation. Neither of the methods can be considered as absolutely superior to the other. Which method performs better will depend upon the type of problem, the dataset, problem complexity, computation complexity and the desired accuracy. An ANN is considered more suited to non-linear problems. Many researchers have compared different schemes for the specific problem they were trying to solve. A detailed comparison of an ANN with response surface methods (RSM) can be found in [64].

In this appendix, an ANN using backpropagation algorithm is compared to a multiple linear regression model for application in a REMS sensor. Few researchers have carried out this comparison for different prediction and estimation problems. Arulsudar et.al. in their study on the optimization of formulation parameters of leuprolide acetate loaded liposomes, concluded that the ANN model provides more accurate prediction in the optimization of pharmaceutical formulations when compared to multiple regression analysis method [65]. In another study on optimizing formulation parameters of cytarabine liposomes, Subramanian et. al. demonstrated that an ANN is more accurate than the multiple regression analysis for optimizing formulation parameters of cytarabine liposomes [66]. For predicting the somatic production/biomass ratio of animal populations from the empirical data of population parameters, the ANN

displayed about 6% better performance than multiple regression [67]. In another research project, the ANN showed a greater capacity of prediction than multiple linear regression in developing the objective functions of the orthopaedic screws [68].

In multilinear regression, the dependent data y_i depends upon several independent variables, x_1, x_2, \dots, x_k . For example, if the given data depends only on three independent variables, the data points will be $(x_{1i}, x_{2i}, x_{3i}, y_i)$. The objective is to minimize the sum:

$$R^2 = \sum_{i=1}^N (a_1 x_{1i} + a_2 x_{2i} + a_3 x_{3i} + b - y_i)^2 \quad (103)$$

The system of n equations can be written as

$$A\mathbf{W} = \mathbf{Y} \quad (104)$$

where

$$A = \begin{pmatrix} x_{11} & x_{21} & x_{31} & 1 \\ x_{12} & x_{22} & x_{32} & 1 \\ x_{13} & x_{23} & x_{33} & 1 \\ \vdots & \vdots & \vdots & \vdots \\ x_{1N} & x_{2N} & x_{3N} & 1 \end{pmatrix}, \quad \mathbf{W} = \begin{pmatrix} a_1 \\ a_2 \\ a_3 \\ b \end{pmatrix}, \quad \mathbf{Y} = \begin{pmatrix} y_1 \\ y_2 \\ y_3 \\ \vdots \\ y_N \end{pmatrix}.$$

To solve for the coefficients, \mathbf{W} , the matrix A is to be inverted. To avoid the difficulties associated with inverting a non square matrix, Eq. 104 is rewritten as

$$A^t A \mathbf{W} = A^t \mathbf{Y}, \quad (105)$$

and then the solution of multilinear regression is given by

$$\mathbf{W} = (A^t A)^{-1} A^t \mathbf{Y}. \quad (106)$$

To compare linear regression and neural network for use with a REMS sensor, a multiple linear regression model was used for reconstructing the spatially distributed complex permittivity profile of the same set of three, three section, lossy electro-material lines as described in Chapter VII (Eq. 91 - Eq. 100). The results for estimating $\tan \delta$ using regression are tabulated in Table 29. For the purpose of comparison, exactly the same data set was used for multilinear regression as was used for the ANN. Which means that 46,656 variables were used in multilinear regression. One major difference for using multi linear regression was that ϵ'_r or $\tan \delta$ could not be reconstructed for all the three sections of the electro-material line simultaneously. Therefore, using the same data set, multilinear regression was used to backsolve ϵ'_r or $\tan \delta$ for each section individually. For a n section electro-material line, one ANN can be used to reconstruct spatially distributed ϵ'_r or $\tan \delta$, however for multilinear regression it will require n independent systems of equations.

These results can be compared with the ANN results listed in Table 24. It can be observed that the results are more accurate when using an ANN as compared to a regression model. For the low noise data, the accuracy of multilinear regression is much worse than ANN. As the data gets more noisy, i.e AWGN with 10 or 15dB SNR, there is no consistency in the results of regression model and it becomes very sensitive to the added noise. If the algorithm is run multiple times, the results do not show any consistency or repeatability. However, for the same level of measurement noise, the results of ANN are consistent and repeatable.

The estimates for reconstructing spatially distributed ϵ'_r using regression are tabulated in Table 30.

The ϵ'_r values reconstructed using regression model can be compared with the ANN results reported in Table 27. It can be observed that although the difference in accuracy is not as wide as in the case of $\tan \delta$, the neural network results are still more accurate than the multilinear regression estimates.

Table 29: Results for estimating $\tan \delta_{1,2,3}$ using multiple linear regression for three different lossy electro-material lines with $3.5 \leq \epsilon'_{r1} \leq 4.0$, $2.5 \leq \epsilon'_{r2} \leq 3.0$, and $4.5 \leq \epsilon'_{r3} \leq 5.0$. The results are presented for the frequency range of 4.0 - 5.5 GHz with $\Delta f = 75 MHz$, in presence of white Guassian noise with 15dB, 20dB, 25dB and 30dB SNR. (Est. denotes estimated)

	ϵ'_{r1}	ϵ'_{r2}	ϵ'_{r3}	
	$\tan \delta_1$	$\tan \delta_2$	$\tan \delta_3$	Avg % error
Actual-A ($\tan \delta$)	0.02	0.05	0.1	
Est-A ($\widetilde{\tan \delta}$) (No Noise)	0.0339	0.046	0.0922	
% error	69.5	8.0	7.8	28.433
Est-A ($\widetilde{\tan \delta}$) AWGN 30dB SNR	0.0497	0.0606	0.0767	
% error	148.5	21.2	23.3	64.33
Est-A ($\widetilde{\tan \delta}$) AWGN 25dB SNR	0.0639	0.0604	0.0648	
% error	219.5	20.8	35.2	91.833
Est-A ($\widetilde{\tan \delta}$) AWGN 20dB SNR	0.067	0.0668	0.0531	
% error	235.0	33.60	46.90	105.167
Est-A ($\widetilde{\tan \delta}$) AWGN 15dB SNR	0.0572	0.0572	0.0689	
% error	186.0	14.40	31.10	77.167
Actual-B ($\tan \delta$)	0.05	0.03	0.08	
Est-B ($\widetilde{\tan \delta}$) (No Noise)	0.0481	0.0328	0.0826	
% error	3.8	9.33	3.25	5.461
Est-B ($\widetilde{\tan \delta}$) AWGN 30dB SNR	0.0381	0.0455	0.0815	
% error	23.8	51.67	1.875	25.781
Est-B ($\widetilde{\tan \delta}$) AWGN 25dB SNR	0.0451	0.0465	0.0785	
% error	9.8	55.0	1.875	22.225
Est-B ($\widetilde{\tan \delta}$) AWGN 20dB SNR	0.0397	0.0517	0.0738	
% error	20.6	72.33	7.75	33.561
Est-B ($\widetilde{\tan \delta}$) AWGN 15dB SNR	0.0499	0.0532	0.0633	
% error	0.200	77.33	20.875	32.803
Actual-C ($\tan \delta$)	0.09	0.08	0.03	
Est- C ($\widetilde{\tan \delta}$) (No Noise)	0.0867	0.0763	0.03337	
% error	3.667	4.625	12.33	6.875
Est-C ($\widetilde{\tan \delta}$) AWGN 30dB SNR	0.0733	0.0735	0.0482	
% error	18.556	8.125	60.667	29.116
Est-C ($\widetilde{\tan \delta}$) AWGN 25dB SNR	0.0821	0.0737	0.0415	
% error	8.778	7.875	38.33	18.329
Est-C ($\widetilde{\tan \delta}$) AWGN 20dB SNR	0.0748	0.0658	0.0592	
% error	16.889	17.75	97.33	43.991
Est-C ($\widetilde{\tan \delta}$) AWGN 15dB SNR	0.0611	0.0669	0.0624	
% error	32.111	16.735	108.00	52.162

Table 30: Results for estimating $\epsilon'_{r1,2,3}$ using multiple linear regression for three different lossy electro-material lines with $0.01 \leq \tan \delta_{1,2,3} \leq 0.10$. The results are presented for the frequency range of 4.0 - 5.5 GHz with $\Delta f = 75MHz$, in presence of white Gaussian noise with 10dB, 15dB, and 20dB SNR. (Est. denotes estimated)

	$\tan \delta_1$	$\tan \delta_2$	$\tan \delta_3$	
	ϵ'_{r1}	ϵ'_{r2}	ϵ'_{r3}	Avg % error
Actual-A (ϵ'_r)	3.5	2.9	4.7	
Est-A ($\tilde{\epsilon}'_r$) (No Noise)	3.501	2.901	4.6	
% error	% 0.02	% 0.01	% 0.06	% 0.03
Est-A ($\tilde{\epsilon}'_r$) AWGN 20dB SNR	3.66	2.811	4.73	
% error	% 4.6	% 3.076	% 0.668	% 2.781
Est-A ($\tilde{\epsilon}'_r$) AWGN 15dB SNR	3.661	2.812	4.7	
% error	% 4.6	% 3.038	% 0.009	% 2.549
Est-A ($\tilde{\epsilon}'_r$) AWGN 10dB SNR	3.6479	2.8235	4.7	
% error	% 4.226	% 2.638	% 0.153	% 2.339
Actual-B (ϵ'_r)	3.7	2.6	4.96	
Est-B ($\tilde{\epsilon}'_r$) (No Noise)	3.701	2.59	4.97	
% error	% 0.068	% 0.054	% 0.032	% 0.05
Est-B ($\tilde{\epsilon}'_r$) AWGN 20dB SNR	3.72	2.64	4.75	
% error	% 0.484	% 1.746	% 4.165	% 2.132
Est-B ($\tilde{\epsilon}'_r$) AWGN 15dB SNR	3.77	2.66	4.75	
% error	% 1.88	% 2.33	% 4.05	% 2.752
Est-B ($\tilde{\epsilon}'_r$) AWGN 10dB SNR	3.72	2.71	4.71	
% error	% 0.630	% 4.104	% 4.909	% 3.214
Actual-C (ϵ'_r)	3.9	2.75	4.53	
Est- C ($\tilde{\epsilon}'_r$) (No Noise)	3.89	2.74	4.536	
% error	% 0.09	% 0.033	% 0.126	% 0.083
Est-C ($\tilde{\epsilon}'_r$) AWGN 20dB SNR	3.704	2.788	4.623	
% error	% 5.026	% 1.404	% 2.051	% 2.827
Est-C ($\tilde{\epsilon}'_r$) AWGN 15dB SNR	3.7069	2.7804	4.6975	
% error	% 4.951	% 1.105	% 3.698	% 3.251
Est-C ($\tilde{\epsilon}'_r$) AWGN 10dB SNR	3.73	2.7652	4.6856	
% error	% 4.385	% 0.549	% 3.435	% 2.790

On the basis of this brief analysis it can be concluded that multilinear regression can be used in a limited scope for REMS sensor application, however, the ANN appears to give more accurate results and is more robust against measurement noise. In practical scenarios where ferroelectric materials and materials like LC 5CB will be used in the electro-material line, the nonlinearity in the relationship between material properties and temperature will be much higher. In that case ANNs are expected to perform much better than the multiple regression models.

REFERENCES

- [1] G. Durgin, “Reflected Electro-Material Signature (REMS) Sensor,” Provisional Patent filed on June 2008.
- [2] N. Muto, H. Yanagida, T. Nakatsuji, M. Sugita, Y. Ohtsuka, and Y. Arai, “Design of intelligent materials with self-diagnosing function for preventing fatal fractures,” *Smart Materials and Structures*, vol. 1, pp. 324 – 329, Nov. 1992.
- [3] B. D. Westermo and L. Thompson, “Smart structural monitoring: A new technology,” *International Journal of Sensors*, pp. 15–18, Nov. 1994.
- [4] A. Mita and S. Takahira, “Damage index sensor for smart structures,” *Structural Engineering and Mechanics*, vol. 17, no. 3-4, pp. 231–346, 2004.
- [5] J. T. Simonen, M. M. Andringa, K. M. Grizzle, S. L. Wood, and D. P. Neikirk, “Wireless sensors for monitoring corrosion in reinforced concrete members,” *Proceeding of SPIE - Smart Structures and Materials*, vol. 5391, pp. 587–596, 2004.
- [6] K. J. Loh, J. P. Lynch, and N. A. Kotov, “Passive wireless sensing using swnt-based multifunctional thin film patches,” *International Journal of Applied Electromagnetics*, vol. 28, pp. 87–94, 2008.
- [7] G. Marrocco and D. Scarana, “Permittivity passive rfid sensor for non-cooperating objects,” in *The Second European Conference on Antennas and Propagation, EuCAP*, 2007, pp. 1 – 4.
- [8] G. Marrocco and F. Amato, “Self-sensing passive rfid: From theory to tag design and experimentation,” in *European Microwave Conference, EuMC*, Oct. 2009, pp. 1 – 4.
- [9] R. Bhattacharyya, C. Floerkemeier, and S. Sarma, “Low-cost, ubiquitous rfid-tag-antenna-based sensing,” *Proceedings of the IEEE*, vol. 98, no. 9, pp. 1593–1600, 2010.
- [10] S. Chandrasekhar, *Liquid Crystals, 2nd Ed.* Cambridge: Cambridge University Press, 1992.
- [11] P. Collings and M. Hird, *Introduction to Liquid Crystals.* Bristol, PA: Taylor & Francis, 1997.
- [12] R. O’Handley, *Magnetic Materials: Principles and Applications.* Wiley-Interscience, 1999.

- [13] J. Griffin and G. Durgin, "Complete link budgets for backscatter-radio and rfid systems," *Antennas and Propagation Magazine, IEEE*, vol. 51, no. 2, pp. 11–25, Apr. 2009.
- [14] H. Oraizi, "Design of impedance transformers by the method of least squares," *Microwave Theory and Techniques, IEEE Transactions on*, vol. 44, no. 3, pp. 389–399, mar 1996.
- [15] D. M. Pozar, *Microwave Engineering*, 3rd Ed, John Wiley and Sons- New York, 2005.
- [16] W. Sha and K. Edwards, "The use of artificial neural networks in materials science based research," *Materials and Design*, vol. 28, no. 6, pp. 1747–1752, 2007.
- [17] L. F. Chen, C. K. Ong, C. P. Neo, V. V. Varadan, and V. K. Varadan, *Microwave Electronics Measurements and Material Characterization*. West Sussex, England: John Wiley & Sons, 2004.
- [18] P. C. Fannin, T. Relihan, and S. W. Charles, "Investigation of ferromagnetic resonance in magnetic fluids by means of the short-circuited coaxial line technique," *Journal of Physics D: Applied Physics*, vol. 28, pp. 2002–2006, Feb. 1995.
- [19] J. C. Booth, D. H. Wu, and S. M. Anlage, "A broadband method for the measurement of the surface impedance of thin films at microwave frequencies," *Review of Scientific Instruments*, vol. 65, pp. 2082–2090, Jun. 1995.
- [20] J. Krupka, R. G. Geyer, M. Kuhn, and J. H. Hinken, "Dielectric properties of single crystals of Al_2O_3 , $LaAlO_3$, GaO_3 , $SrTiO_3$, and MgO at cryogenic temperatures," *Microwave Theory and Techniques, IEEE Transactions on*, vol. 42, no. 10, pp. 1886–1890, oct 1994.
- [21] R. G. Geyer and J. Krupka, "Microwave dielectric properties of anisotropic materials at cryogenic temperatures," *Instrumentation and Measurement, IEEE Transactions on*, vol. 44, no. 2, pp. 329–331, apr 1995.
- [22] C. Q. Lee, "Wave propagation and profile inversion in lossy inhomogeneous media," *Proceedings of the IEEE*, vol. 70, no. 3, pp. 219–228, Mar. 1983.
- [23] M. Nakhkash, Y. Huang, and M. T. C. Fang, "Application of the multi-level single-linkage method to one-dimensional electromagnetic inverse scattering problem," *IEEE Trans. on Antennas and Propagation*, vol. 47, no. 11, pp. 1658–1668, Nov. 1999.
- [24] H. W. Yang and R. S. Chen, "FDTD analysis on the effect of plasma parameters on the reflection coefficient of the electromagnetic wave," *Optical and Quantum Electronics*, vol. 39, no. 15, pp. 1245–1252, Dec. 2007.

- [25] E. Kemppinen, "Effective permittivity and attenuation coefficient of microstrip transmission line determined by 1-port and 2-port measuring methods," *Measurement Science and Technology*, vol. 11, pp. 38–44, 2000.
- [26] J. Bandler, M. Ismail, J. Rayas-Sanchez, and Q.-J. Zhang, "Neuromodeling of microwave circuits exploiting space-mapping technology," *Microwave Theory and Techniques, IEEE Transactions on*, vol. 47, no. 12, pp. 2417–2427, dec 1999.
- [27] Q. J. Zhang, K. C. Gupta, and V. K. Devabhaktuni, "Artificial neural networks for rf and microwave design - from theory to practice," *IEEE Transactions on Microwave Theory and Techniques*, vol. 51, no. 4, pp. 1339–1350, Apr. 2003.
- [28] H. Kabir, M. Yu, and Q. J. Zhang, "Recent advances of neural network-based em-cad," *International Journal of RF and Microwave CAE*, vol. 20, pp. 502–511, Jul. 2010.
- [29] S. R. H. Hoole, "Artificial neural networks in the solution of inverse electromagnetic field problems," *IEEE Trans. on Magnetism*, vol. 29, no. 2, pp. 1931–1934, Mar. 1993.
- [30] I. Elshafiey, L. Udpa, and S. S. Udpa, "Application of Neural Networks to Inverse Problems in Electromagnetics," *IEEE Trans. on Magnetism*, vol. 30, no. 5, pp. 3629–3632, Sep. 1994.
- [31] C. Christodoulou and M. Georgiopoulos, *Application of Neural Networks in Electromagnetics*. Boston, London: Artech House, 2001.
- [32] S. Caorsi and P. Gamba, "Electromagnetic detection of dielectric cylinders by a neuralnetwork approach," *IEEE Trans. on Geo Science and Remote Sensing*, vol. 37, no. 2, pp. 820–827, Mar. 1999.
- [33] E. Bermani, S. Caorsi, and M. Raffetto, "Microwave detection and dielectric characterization of cylindrical objects from amplitude-only data by means of neural networks," *IEEE Trans. on Antennas and Propagation*, vol. 50, no. 9, pp. 1309–1314, Sep. 2002.
- [34] F. Yaman and S. Simsek, "Neural network approach to determine nonsmooth one-dimensional profiles in inverse scattering theory ," *Microwave and Optical Technology Letters*, vol. 49, no. 12, pp. 3158–3162, Sep. 2007.
- [35] K. Mehrotra, S. Ranka, and C. K. Mohan, *Elements of Artificial Neural Networks*. MIT Press, 1996.
- [36] M. T. Hagan, H. B. Demuth, and M. Beale, *Neural Network Design*. Boston, MA: PWS Publishing Company, 1996.
- [37] R. M. and H. Braun, "A direct adaptive method for faster backpropagation learning: The RPROP algorithm," *IEEE International Conference on Neural Networks*, vol. 1, no. 1, pp. 586–591, 1993.

- [38] D. G. Luenberger, *Introduction to Linear and Non Linear Programming*. Addison Wesley Pub. Co., 1973.
- [39] F. R. and C. Reeves, "Function minimization by conjugate gradients," *Computer Journal*, vol. 7, pp. 149–154, 1964.
- [40] M. Powell, "Restart procedures for the conjugate gradient method," *Mathematical Programming*, vol. 12, pp. 241–254, 1977.
- [41] E. Beale, "A derivation of conjugate gradients" in *F.A.Lootsma, Ed., Numerical methods for nonlinear optimization*. London Academic Press, 1972.
- [42] M. Moller, "A scaled conjugate gradient algorithm for fast supervised learning," *Neural Networks*, vol. 6, pp. 525–533, 1993.
- [43] R. Battiti, "First- and Second-Order Methods for Learning: Between Steepest Descent and Newton's Method," *Neural computation*, vol. 4, no. 2, pp. 141–166, Jun. 1992.
- [44] D. W. Marquardt, "An Algorithm for Least-Squares Estimation of Nonlinear Parameters," *Journal of the Society for Industrial and Applied Mathematics*, vol. 11, no. 2, pp. 431–441, Jun. 1963.
- [45] M. Hagan and M. Menhaj, "Training feed-forward networks with the Marquardt algorithm," *IEEE Transactions on Neural Networks*, vol. 5, no. 61, pp. 989–993, Nov. 1994.
- [46] G. Czechowski, J. Jadzyn, J. Ziolo, S. Rzoska, and M. Paluch, "Linear and non-linear dielectric pretransitional behavior near the isotropic-nematic phase transition for 4-cyano-4-n-pentylbiphenyl (5CB)," *Journal of Physical Sciences*, vol. 57, no. 5, pp. 244–246, May 2002.
- [47] Agilent 85070D: Dielectric Probe Kit, Product Overview.
- [48] T. Meissner and F. Wentz, "The complex dielectric constant of pure and sea water from microwave satellite observations," *IEEE Transactions on Geoscience and Remote Sensing*, vol. 42, no. 9, pp. 1836 – 1849, sept. 2004.
- [49] D. Duong and P. Steffes, "The Complex Dielectric Properties of Aqueous Ammonia from 2 GHz - 8.5 GHz in Support of the NASA JUNO Mission," Master's thesis, The Georgia Institute of Technology, 2011.
- [50] A. Hasan, A. F. Peterson, and G. D. Durgin, "Feasibility of passive wireless sensors based on reflected electro-material signatures," *The Applied Computational Electromagnetic Society Journal*, vol. 25, no. 10, pp. 552–560, Jun. 2010.
- [51] G. S. Smith and J. D. Nordgard, "Measurement of the electrical constitutive parameters of materials using antennas," *IEEE Transactions on Antennas and Propagation*, vol. AP-33, no. 7, pp. 783–792, 1985.

- [52] D. W. Gooch, J. C. W. Harrison, R. W. P. King, and T. T. Wu, "Impedances of long antennas in air and in dissipative media," *Journal of Research at the National Bureau of Standards*, vol. 67D, no. 3, pp. 355–360, May 1963.
- [53] S. C. Olson and M. F. Iskander, "A new in-situ procedure for measuring the dielectric properties of low permittivity materials," *IEEE Transactions on Instrumentation and Measurement*, vol. IM-35, no. 1, pp. 2–6, Mar. 1986.
- [54] A. Denoth, "The monopole-antenna : A practical snow and soil wetness sensor," *IEEE Transactions on Geoscience and Remote Sensing*, vol. 35, no. 5, pp. 1371–1375, Sep. 1997.
- [55] F. M. Sagnard, V. Guilbert, and C. Fauchard, "In-situ characterization of soil moisture content using a monopole probe," *Journal of Applied Geophysics*, vol. 68, pp. 182–193, 2009.
- [56] A. Hirose, *Complex-Valued Neural Networks*. Berlin / Heidelberg: Springer, 2006.
- [57] H. Acikgoz, Y. L. Bihan, O. Meyer, and L. Pichon, "Neural networks for broad-band evaluation of complex permittivity using a coaxial discontinuity," *Eur. Phys. J. Appl. Phys.*, vol. 39, no. 2, pp. 197–201, 2007. [Online]. Available: <http://dx.doi.org/10.1051/epjap:2007073>
- [58] G. M. Georgiou and C. Koutsougeras, "Complex domain bakpropagatoin," *IEEE Transactions on Circuits and Systems - II: Analog and Diital Signal Processing*, vol. 39, no. 5, pp. 330–334, May 1992.
- [59] M. Smith and Y. Hui, "A data extrapolation algorithm using a complex domain neural network," *IEEE Transactions on Circuits and Systems - II: Analog and Diital Signal Processing*, vol. 44, no. 2, pp. 143 –147, Feb 1997.
- [60] A. Hasan and A. F. Peterson, "Measurement of complex permittivity using artificial neural networks," in *Proceedings of 32nd AMTA symposium, Atlanta*, Oct. 2010.
- [61] —, "Measurement of complex permittivity using artificial neural networks," *Antennas and Propagation Magazine, IEEE*, vol. 53, no. 1, pp. 200 –203, Feb. 2011.
- [62] A. Hasan, A. F. Peterson, and G. D. Durgin, "Reflected electro-material signatures for self-sensing passive rfid sensors," in *Proceedings of IEEE International Conference on RFID, Orlando*, Apr. 2011, pp. 62 –69.
- [63] D. Dardari and R. D'Errico, "Passive ultrawide bandwidth rfid," in *Global Telecommunications Conference, 2008. IEEE GLOBECOM 2008. IEEE*, 30 2008.

- [64] M. Abbas and G. Vachtsevanos, “System-level health assessment of complex engineered processes,” Ph.D. dissertation, The Georgia Institute of Technology, 2010.
- [65] N. Arulsudar1, N. Subramanian, and R. Murthy, “Comparison of artificial neural network and multiple linear regression in the optimization of formulation parameters of leuprolide acetate loaded liposomes,” *Journal of Pharmacy & Pharmaceutical Sciences*, vol. 8, no. 2, pp. 243–285, Aug. 2005.
- [66] N. Subramanian, A. Yajnik, and R. S. R. Murthy, “Artificial neural network as an alternative to multiple regression analysis in optimizing formulation parameters of cytarabine liposomes,” *Journal of Pharmacy & Pharmaceutical Sciences*, vol. 5, no. 1, pp. 1–9, 2004.
- [67] T. Brey, A. Jarre-Teichmann, and O. Borlich, “Artificial neural network versus multiple linear regression: predicting p/b ratios from empirical data,” *Marine Ecology Series*, vol. 140, pp. 251 – 256, Sep. 1996.
- [68] C.-C. Hsu, J. Lin, and C.-K. Chao, “Comparison of multiple linear regression and artificial neural network in developing the objective functions of the orthopaedic screws,” *Computer Methods and Programs in Biomedicine*, vol. 104, no. 3, pp. 341 – 348, 2011. [Online]. Available: <http://www.sciencedirect.com/science/article/pii/S0169260710002804>

VITA

Azhar Hasan received his early education from Islamabad College for Boys, Islamabad, Pakistan. Then he gained his BE and MS degrees in electrical engineering from National University of Sciences and Technology, Pakistan, in 1997 and 2007, respectively. He is currently a PhD candidate in electrical and computer engineering at Georgia Institute of Technology, Atlanta. His research involves material characterization and numerical techniques for passive RFID based sensing applications. He also holds interest in researching passive components for RF/microwave front end applications and transmit diversity schemes for Backscatter RFID systems.